博 士 学 位 論 文

Doctoral Dissertation

Formation and evolution of silicic magma plumbing system and fluid genesis in subduction zone of NE Japan - Kuril region

（東北日本ー千島地域の沈み込み帯における珪長質マグマ上昇の形成・発達過程と流体の発生に関する研究）

東北大学大学院環境科学研究科
Graduate School of Environmental Studies, Tohoku University

先進社会環境学専攻	専攻major／コースcourse

学籍番号
Student ID No.
C0GD1504

氏 名
Name
Kotov Alexey

<table>
<tr><td>指導教員
Supervisor at Tohoku Univ.</td><td colspan="2">教 授 土屋 範芳</td></tr>
<tr><td>研究指導教員
Research Advisor at Tohoku Univ.</td><td colspan="2"></td></tr>
<tr><td rowspan="4">審査委員
（○印は主査）
Dissertation Committee Members
Name marked with “○” is the Chief Examiner</td><td colspan="2">教授 土屋 範芳</td></tr>
<tr><td>1 教授 岡本 敦</td><td>2 教授 中村 美千彦
（理学研究科）</td></tr>
<tr><td>3 教授 伴 雅雄
（山形 大学）</td><td>4</td></tr>
<tr><td>5</td><td>6</td></tr>
</table>

Content

Chapter 1. Introduction

Geology of the NE Honshu – Southern Kuril Arc

The NE Honshu to southern Kuril region is a typical convergent margin, where is magmatism associated with a subduction. This is one of the well-described subduction zones which provides a useful information for understanding how subduction factory produce magma, from the most primitive basalts to the most evolved silicic magmas.

The NE Honshu – Southern Kuril arc is associated with westward subduction of the Pacific plate beneath the Eurasian plate at a rate of 7.7 to 8.2 cm/yr (Syracuse et al., 2010). The northeastern Honshu-Hokkaido-Southern Kuril subduction system is a unique example where there is a gradual transition from NE Honshu, with a crustal thickness of 35-40 km and a slab dip angle to about 30°, to the southern Kuril Islands, with a crustal thickness of 15-20 km and a slab dip angle to 46° (Syracuse at al., 2010). Such a transition, together with different thickness and composition of Island crust, explain the change in the composition of eruptive rocks. The collision of the Northeast Japan arc with the Kuril arc due to oblique subduction of the Pacific plate is evident at the transition boundary (Iwasaki et al., 2019). The types generated by volcanoes differ significantly in the studied zone, which is obviously a consequence of differences in crustal thickness, slab dip angle, and other subduction parameters (plate age, dip rate, thermal parameter, slab thickness). The modern volcanism of the frontal part of these arcs is characterized by a large number of large silicic eruptions, whereas the rear part of the arc is characterized by more primitive basaltic and andesite-basaltic volcanoes, and silicic volcanism is limited.

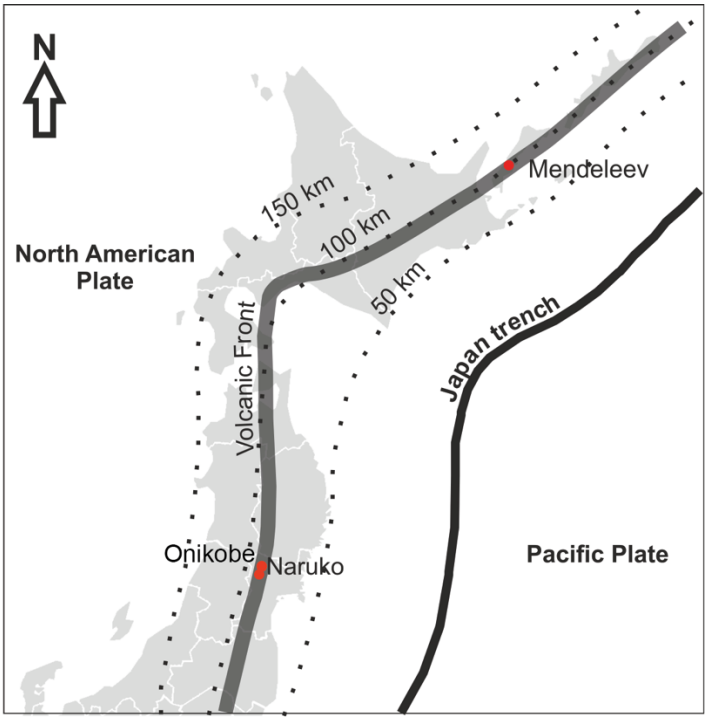

Figure 1.1. Map of the NE Honshu – Southern Kuril Arc subduction zone. The red dots represent the calderas involved in this study and discussed below. Dotted lines indicate slab depths (Zhao et al., 1997). Thick grey line indicates a volcanic front.

Genesis of voluminous silicious magmas in subduction zones. Its storage and magmatic processes timescales

In this study, voluminous silicic magma formation is key issue. To respond to these questions, I describe in detail the results of a study of four large caldera eruptions: the caldera eruption of Mendeleev volcano, two caldera eruptions of Onikobe caldera and one caldera eruption of Naruko caldera (NE Honshu). I have established P-T-*f*O parameters for the formation of these magmas, the content of volatiles in the parental melts, and proposed scenarios and mechanisms of formation for each certain case.

Caldera forming eruptions are of particular interest because of their high explosivity and large volumes of erupted material. Caldera-forming eruptions are characterized by volumes of ejected material ranging from the first km^3 to the first hundred km^3. At the same time, all caldera eruptions are examples of silicic volcanism. Large caldera eruptions mostly occurred in subduction settings and are associated with the development of shallow high-silica magmatic system, with a high concentration of volatile components.

The formation of such voluminous, fluid-rich magmatic systems is the cause of combination of magmatic processes occurring from the slab to the upper crust. Within the crust,

two main processes can lead to the formation of silicic magmas: differentiation of primary magmas (e.g., Gill, 1981; Grove et al., 2002; Annen et al., 2006; Nandedkar et al., 2014; Marxer et al, 2022; Miyagi et al., 2023) and/or partial melting of crustal rocks (e.g., Rapp et al., 1991; Beard & Lofgren, 1991; Atherton & Petford, 1993; Rapp & Watson, 1995; Petford & Atherton, 1996; Petford & Gallagher, 2001; Izbekov et al., 2004; Annen et al., 2006; Shukuno et al., 2006; Hammerli et al., 2018; Kotov et al., 2023). These processes are inextricably linked. For example, the intrusion of primitive rocks into the island crust leads to partial melting of these rocks, and the formation of most evolved ones, while crystallization of intruded magmas forms other residual silicic magmas and silica-depleted restite. The interaction of magmas with each other (mixing) or with crustal rocks (assimilation) leads to the formation of additional scenarios of magma formation. Eventually, shallow magma storage zones are formed, in which large amounts of felsic low-mobile magmas are stored.

It's known that crustal magma bodies contain large amount of volatile components in the form of dissolved compounds, structural units of minerals and fluid. Recent studies of volcanic emanations and inclusions of mineral-forming environments show that the most important volatile components of magmatic systems are H_2O and CO_2. Such volatiles as S, F, Cl, and others play a less prominent, but still important role in the evolution of caldera-forming eruptions, as well as in the formation of epithermal and porphyry deposits (Wallace, 2005; Oppenheimer et al., 2014).

For over a century, the melt-dominated magma chamber was a predominant concept describing arc crustal magmatic systems. However, in recent decades, much evidence has called into question this established paradigm. Simultaneously, physicochemical models exploring igneous processes have indicated the surprising difficulty in both the formation and maintenance of magma chambers. Consequently, there has been a growing emphasis on igneous processes that involve a magma chamber confined solely to the uppermost portion of a significantly larger magmatic system. This system extends throughout the crust, exhibits a predominantly crystalline structure, and encompasses a heterogeneous distribution of melt, crystals, and exsolved volatiles across space and time.

A recent model on the generation and accumulation of voluminous magma is the 'crystal mush model' (Hildreth, 2004; Bachmann & Bergantz 2004, 2008). Following that model, magmatic systems can exist in crustal conditions as bodies of crystal-rich (>45–60 % crystals) magma of broadly intermediate bulk composition and highly silicic interstitial melt. Such bodies may occasionally erupt (the 'monotonous intermediates' of Hildreth 1981; e.g.,

Bachmann et al. 2002), but most evolved crystal-poor rhyolites are inferred to have been extracted from the mush zone and accumulated at shallower levels prior to eruption (Allan et al., 2013) in the "melt-dominant" eruptible bodies. Thus, here we consider the formation mechanisms of bulk felsic magmas of two volcanoes in terms of petrology and mineralogy and volatile content.

It is known that the formation of such mushy bodies within the crust can take 10^5-10^6 years, while remobilization and migration of eruptible magmas can occur within years to thousand years (e.g., Cooper, 2019, and references therein). Thus, interpreting the time scales of these processes plays a key role in understanding geological processes.

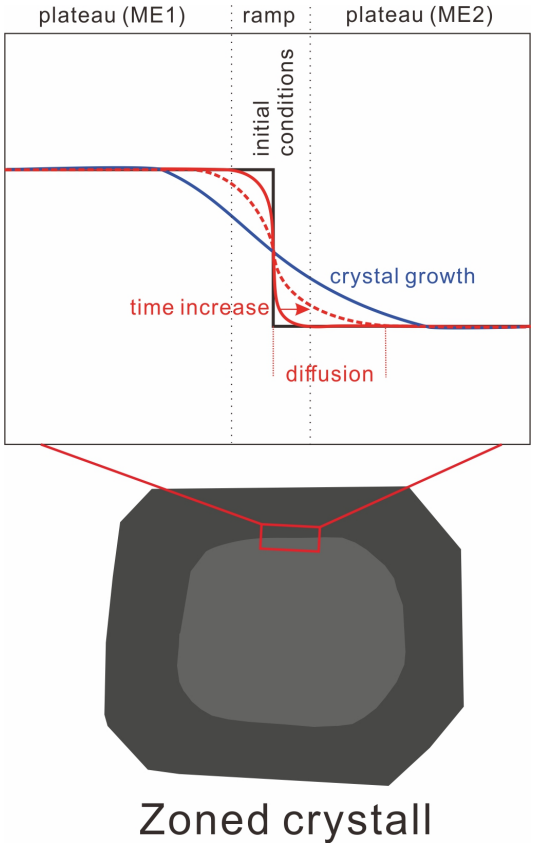

Figure 1.2. Schematic illustration of diffusion profile on the border between two zones in the mineral.

There are many ways to estimate the time scales of these processes. One of such ways is time scales based on diffusion profiles in a mineral. Diffusion zoning occurred at the crystal boundary when the surrounding parameters change. That border can be used to estimate the equilibration time of this crystal during the transition from one magmatic environment to another. Thus, it is possible to estimate the timing of such processes as the movement of magmas from depth to shallower parts, mixing of magmas, remobilization of mush, and initiation of eruptions through mafic recharge. Diffusion time modelling suggests that initially, when P-T conditions changed around the crystal, its composition changed abruptly, and step-

wise concentration gradients were formed. This gradient was changed over time by elements interdiffusion, resulting in sigmoidal concentration gradients (Fig. 1.2). The assumption that the sigmoidal gradient is a result of diffusion only yields the maximum timescale. Diffusion chronometry, which is applied to such compositionally zoned crystals, provides important insights into pre-eruptive magmatic timescales (Costa et al., 2008; Dohmen et al., 2017; Costa et al., 2020; Costa, 2021; Chakraborty & Dohmen, 2022; Sato et al., 2022; Elms et al., 2023). There can also be discrepancies in time scales estimated from different phases recording seemingly common processes (e.g., Chamberlain et al., 2014), so if zonality in crystals permits, it is important to consider time scales across multiple phases.

Water budget in crustal magmatic systems

Subduction zones are the largest Earth factory where is exchanging in volatiles (H_2O, CO_2, S, halogens) appear between the different Earth's reservoirs. Studying the process of magma formation and evolution of magmatic systems in subduction zones is a fundamental task of geology designed to answer questions about the mechanisms of formation of new continental crust, epithermal deposits, and the role of subduction in geochemical cycles of major volatiles (Jarrard, 2003; Wallace, 2005; Kimura & Yoshida, 2006; Grove et al., 2012; Parai & Mukhopadhyay, 2012; Zellmer et al., 2015). The process of magma formation and circulation of volatile components are inextricably linked and, therefore, it is impossible to consider the circulation of volatile elements in the subduction zone without considering the mechanisms of magma genesis. Thus, this study is designed to investigate the evolution of some Quaternary magmatic systems in the region and the volatile content of their magmas in order to complement the existing understanding of the global volatile circulation in the NE Honshu and Southern Kuril Islands region.

There are many different approaches to studying fluid flux in subduction zones. Geophysical studies have revealed the macroscopic distribution of fluid in the subduction zone and particularly in crust (e.g., Hasegawa et al., 2005; Hasegawa et al., 2009; Ogawa et al., 2014), geochemical studies have estimated long-term fluid flux from subducting plates (Iwamori, 1998; Hacker, 2008; Van Keken, 2011; Nakamura et al., 2019) and volcanoes, solidifying magmatic chambers and dikes (Kimura & Nakajima, 2014; Uno et al., 2017; Amanda et al., 2019). However, the absolute amounts and flow rates of the crustal fluids are highly uncertain, owing to the limited resolution of those approaches in the lower crust. Such deep crust fluids principally originate from the dehydration of the subducting slab. Hydrous magmas generated in the mantle wedge carry aqueous fluids that are released into the lower

and middle crust (Kimura and Nakajima et al., 2014). These fluids then migrate to the bottom of the upper crust and deep geothermal reservoirs (e.g., Nakajima et al., 2001; Tsuchiya et al., 2016).

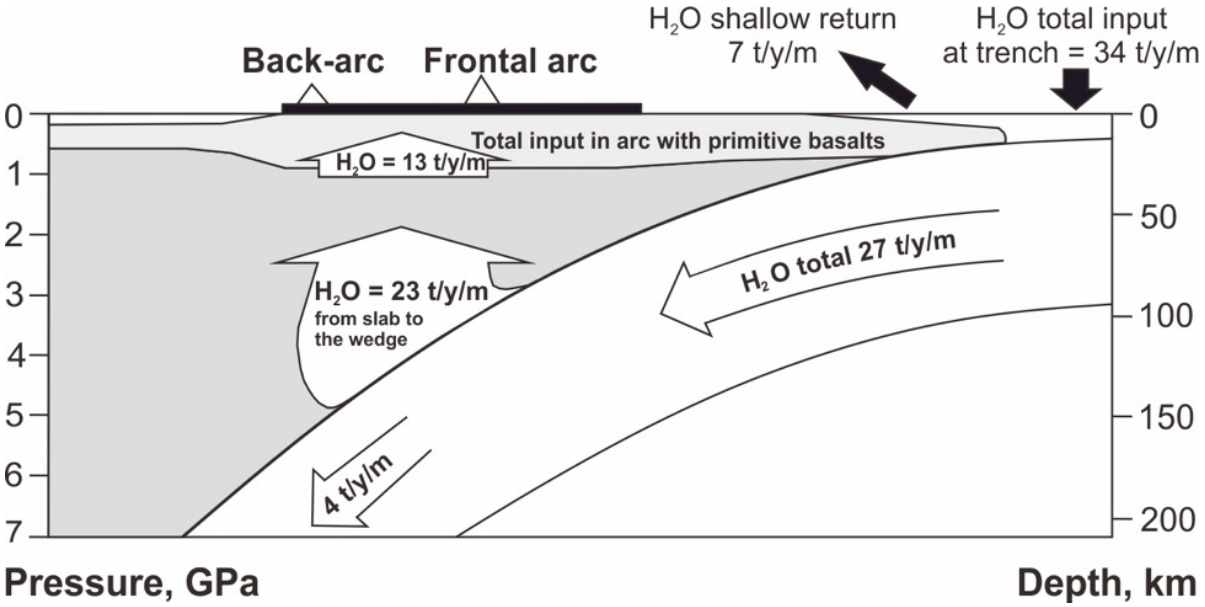

Figure1.3. Schematic cross section of NE Japan and estimated water flux from (Kimura and Nakajima, 2014)

In fact, shallow silicic magmatic systems are the final water reservoir in the entire global subduction cycle. Recently (Kimura and Nakajima, 2014; Kimura et al., 2017), estimated water flux into the crust of the Honshu Island arc from the subduction plate and water mass balance in this part of the subduction zone. Based on that investigation, total water input in subduction zone of NE Honshu is 34 tons/year/meter of subduction length, while total input into the crust of 13 tons/year/meter of subduction length. However, the mass balance of water flow directly within the crust remains unclear. Obviously, water reaching the crust involves in all magmatic processes and can be consumed in reaction with crustal rocks and remain as dissolved or structural water in intrusive bodies. Only some part of this water can reach the upper crustal reservoirs and be released into the atmosphere during eruptions. In order to find this out, it is necessary to understand the mechanism of magma formation and migration throughout the entire crustal thickness, from the more primitive basaltic magmas in the lower crust, to the most evolved silicic magmas in the upper crust. Therefore, I want to address this problem. Also, estimates of water content in the upper crustal reservoirs of felsic magma are important because 1) these reservoirs are potential sources of geothermal energy; 2) dissolved volatiles in the magma define the style and catastrophic potential of a future eruption; 3) they contribute to the formation of epithermal deposits due fluid separation and interaction with crustal rocks.

Objective and Thesis Structure

The purpose of this study is to investigate in detail the magma formation processes of three large Pleistocene calderas in NE Honshu (Naruko and Onikobe calderas) and Kunashir Island (Mendeleev caldera). Here we pay attention to a detailed study of the mineralogy of pyroclastic flows and mineral and melt inclusions from phenocrysts of eruptive rocks. Based on the data obtained, we reconstruct the history of magmatic chamber development that led to the final large caldera eruptions. In addition to basic petrological studies, we address two relevant petrological topics as applied to the objects under study: (1) time scales of magma formation and mobilization based on diffusion profiles in quartz and orthopyroxene and (2) calculation of the water excess that forms during the formation of these magmas under shallow crustal conditions.

The structure of this thesis consists of six chapters. The first chapter is introduction and back- ground study. The second chapter devoted to the detailed petrological investigation of Mendeleev caldera eruption occurred 40 thousand years ago in Kunashir Island. The results described in this chapter were also published in an article (Kotov et al., 2023; JPeT). The third chapter is detailed petrological description of Naruko caldera eruption and two Onikobe caldera eruptions. Described results prepared for publication in JVGR. Chapter 4 is devoted to a study of the timescales of formation and mobilization of magmas from both eruptions of the Naruko caldera. The fourth chapter is inspired by the chapter three as minerals of Naruko caldera deposits have abundant diffusion zoning which indicate different mixing and mobilization processes. Thus, based on diffusion profiles in orthopyroxene and quartz, we provide important information about geological processes and their duration before final catastrophic eruption. In the fifth chapter, we attempted to estimate the excess of water in the formation of felsic magmas through the crystallization of more primitive magmas and partial melting of amphibole-bearing crustal rocks. These scenarios are a theoretical estimate of the magmas of the Naruko and Mendeleev caldera eruptions considered in the example previously described in detail. Chapters 6 is conclusions summarizing the results of the entire dissertation.

List of figures

Lowenstern, 2002) and pressure estimation for amphibole relics using (Ridolfi, 2021). Depth calculated using crustal density of Kunashir Island of 2600 kg/m^3 (Nakanishi et al., 2009)

Figure 2.11. Variations in major-element contents of Mendeleev MIs coexisting with amphibole relics (filled symbols) and amphibole equilibrium melt (AEM; open symbols). AEM was calculated following the model of (Zhang et al., 2017) and updated by (Humphreys et al., 2019).

Figure 2.12. Results of amphibole thermobarometry using the method of (Ridolfi, 2021).

Figure 2.13. Major-element contents from partial melting experiments (filled gray circles) and crystallization experiments (open black circles) compare to Mendeleev melts (open red circles)

Figure 2.14. Comparison of crustal structure of a selection of island arc based on geophysical observations (updated and modified from Melekhova et al., 2019). The range in Vp (km/s) within individual crustal layers is shown by the double-ended arrows. Seismic discontinuities are shown by solid horizontal lines. A question (?) indicates a poorly resolved Moho. References for the arcs are provided by Boynton et al., 1979; Zlobin et al., 1997; Iwasaki et al., 2001; Iwasaki et al., 2004; Christeson et al., 2008; Kopp et al., 2011; Shillington et al., 2004; Kodaira et al., 2007; Takahashi et al., 2007.

Figure 3.1. Schematic map and stratigraphy column of the Naruko and Onikobe caldera deposits based on (Tsuchiya et al., 1997; Sakaguchi and Yamada, 1988). Digital elevation model created with GeoMapApp (Ryan et al. 2009).

Figure 3.2. Whole-rock compositions of Naruko volcanic products. Compositions of modern lavas and mafic inclusions from (Ban et al., 2005). Classification diagrams of (a) $Na_2O + K_2O$ versus SiO_2 (Bas et al., 1986), (b) K_2O versus SiO_2 (Rickwood, 1989), (c) FeO/(FeO + MgO) versus SiO_2 (Frost et al., 2001) and (d) A/NK versus A/CNK (Shand, 1943). All data are volatile-free and normalized to 100 wt.%. All Fe is FeO. A/CNK = $(Al_2O_3/101.96)/(CaO/56.08 + Na_2O/61.98 + K_2O/94.2)$; A/NK = $(Al_2O_3/101.96)/(Na_2O/61.98 + K_2O/94.2)$; MALI = $Na_2O + K_2O - CaO$.

Figure 3.3. BSE images of the plagioclase phenocrysts from Yanagisawa pumice with reverse zoning and evidence of resorption on the border between Low-Ca and High-Ca zones. Numbers are shown An mol% based on EPMA analysis in black spots. An mol% = [XCa/(XCa + XNa+XK) × 100].

Figure 3.4. Statistical distribution of orthopyroxenes in the pumice of the Yanagisawa (a) deposits, respectively. The predominant types for each eruption are shown in bold.

Figure 3.5. BSE images of the amphibole Yanagisawa Tuffs (d-f). Numbers showing Mg-number based on EPMA analysis in black spots Mg-number = $[X_{Mg}/(X_{Mg} + X_{Fe}) \times 100]$. Mgt- Magnetite, Amph-amphibole.

Figure 3.6. Amphibole composition diagram by (Hawthorne et al., 2012); Calculated using a spreadsheet, formula units were calculated based on 22 oxygens (Locock, 2014). Ed - edenite; Prg - pargasite; Sdg - sdanagaite; Tr - tremolite; Mg-Hbl - magnesio-hornblende; Ts – tschermakite. Grey field correspond to the amphibole composition from Onikobe pyroclastic discussed below.

Figure 3.7. Histograms of core and rim composition of zoned crystals of plagioclase (a) and orthopyroxene (b) in Yanagisawa tuffs. An mol% = Ca*100/(Ca+Na+K); Mg#=Mg*100/(Fe+Mg).

Figure. 3.8. Whole-rock compositions of Onikobe caldera eruptions. Classification diagrams of (a) $Na_2O + K_2O$ versus SiO_2 (Bas et al., 1986), (b) K_2O versus SiO_2 (Rickwood, 1989), (c) FeO/(FeO + MgO) versus SiO_2 (Frost et al., 2001) and (d) A/NK versus A/CNK (Shand, 1943). All data are volatile-free and normalized to 100 wt.%. All Fe is FeO. A/CNK = $(Al_2O_3/101.96)/(CaO/56.08 + Na_2O/61.98 + K_2O/94.2)$; A/NK = $(Al_2O_3/101.96)/(Na_2O/61.98 + K_2O/94.2)$; MALI = $Na_2O + K_2O - CaO$.

Figure 3.9. BSE images of the plagioclase phenocrysts from Ikezuki tuffs (a-c) and Shimoyamazato tuffs (d-f). (a) Ikezuki plagioclase with complex zoning (patchy core + concentric outer part and (b) zoomed patchy core of the same crystal with abundant inclusions of clino- and orthopyroxenes and Fe—Ti oxides; (c) Intergrowth of two Ikezuki plagioclase crystals with complex texture; (d-f) Shimoyamazato plagioclase with complex zoning (d), concentric zoning (e), and evidence of resorption on the border between Low-Ca and High-Ca zones (f). Numbers are shown An mol% based on EPMA analysis in black spots. An mol% = [XCa/(XCa + XNa+XK) × 100].

Figure 3.10. BSE images of the pyroxenes from Ikezuki tuffs (a-c) and Shimoyamazato Tuffs (d-f). (a) "Mafic" clot of clino- and orthopyroxene crystals in Ikezuki tuffs with abundant amphibole inclusion; (b and c) Ikezuki clinopyroxene crystal oriented lamellae of orthopyroxene and amphibole; (d) Shimoyamazato orthopyroxene crystal cut along the C axis with amphibole inclusions located in the Mg-rich core; (e and f) Shimoyamazato orthopyroxene

crystal cut across the C axis with amphibole inclusions located in the Mg-rich core; Note the mantle High-Mg zone between core and rime in the crystals cut across C-axis. Numbers showing Mg-number based on EPMA analysis in black spots Mg-number = $[X_{Mg}/(X_{Mg} + X_{Fe})\times 100]$. Mgt- Magnetite, Amph-amphibole.

Figure 3.11. Compositions of mafic minerals in the Ikezuki tuffs and Shimoyamazato tuffs: (a) Classification of pyroxenes according to (Morimoto, 1988); (b) classification of amphiboles following (Hawthorne et al., 2012). Calculated using a spreadsheet, formula units were calculated based on 22 oxygens (Locock, 2014). Ed, edenite; Prg, pargasite; Sdg, sadanagaite; Tr, tremolite; Mg-Hbl, magnesio-hornblende; Ts, tschermakite.

Figure 3.12. Statistical distribution of orthopyroxenes in the pumice of the Shimoyamazato deposits. The predominant types for each eruption are shown in bold.

Figure 3.13. Variations of the major elements in MIs from orthopyroxene and quartz and groundmass glasses from Ikezuki tuffs, Shimoyamazato pumice and Yanagisawa pumice. All data are plotted volatile-free, normalized to 100%. Al Fe as FeO.

Figure 3.14. Volatile elements variations MIs from orthopyroxene, quartz, and groundmass glasses from Ikezuki, Shimoyamazato, and Yanagisawa tuffs. SiO_2 and K_2O content are plotted volatile-free, normalized to 100%. Isobars plotted based on VolatileCalc calculation under 850°C (Newman & Lowenstern, 2002).

Figure 3.15. Result of thermometry and barometry application for the Ikezuki tuffs (upper row) and Shimoyamazato tuffs (bottom row), respectively. Amph - amphibole, Opx – orthopyroxene, Plag – plagioclase.

Figure 3.16. Result of thermometry and barometry application for the Yanagisawa tuffs. Amph - amphibole, Opx – orthopyroxene, Plag – plagioclase.

Figure 3.17. Schematical ME's connection pathways for Ikezuki and Shimoyamazato magma. Each arrow corresponds to the number of EPMA travers from core to rim, indicated observed zoning patterns.

Figure 3.18. Schematical ME's connection pathways for Yanagisawa magma. Each arrow corresponds to the number of EPMA travers from core to rim, indicated observed zoning patterns.

Figure 3.19. Cartoon cross-section of the Yanagisawa magma system. The magmatic processes inferred from crystal textures and chemistry (discussed in the text).

List of tables

Chapter 2. Mendeleev volcano. Formation of voluminous dacite through partial melting under shallow-crustal conditions in Kunashir Island (Southern Kuril arc)

2.1. Introduction

Caldera eruptions, occurring within subduction zones, are rare events but can have catastrophic consequences. When a magmatic system progresses towards a violent caldera-forming eruption, a significant amount of mobile magma accumulates at shallow depths in the arc crust, capable of being rapidly erupted. The precise mechanisms behind the formation and accumulation of such large volumes of felsic magma remain uncertain, hindering our ability to understand the conditions that give rise to massive calderas. The generation of dacitic or rhyolitic arc magmas is commonly attributed to two primary processes: the differentiation of primary mafic or andesitic magmas (e.g., Gill, 1981; Grove et al., 2002; Annen et al., 2006; Nandedkar et al., 2014; Marxer et al., 2022; Miyagi et al., 2023) and/or partial melting of crustal rocks (e.g., Rapp et al., 1991; Beard & Lofgren, 1991; Atherton & Petford, 1993; Rapp & Watson, 1995; Petford & Atherton, 1996; Petford & Gallagher, 2001; Izbekov et al., 2004; Annen et al., 2006; Shukuno et al., 2006; Hammerli et al., 2018). These processes can occur concurrently, with heat and fluids released during the fractional crystallization of basalts playing a significant role in crustal melting.

Caldera-forming eruptions are typically associated with active continental margins characterized by a thick, mature continental crust, such as southwestern North America and the Central Andean Volcanic Zone (e.g., Stern, 2004; Watts et al., 2016; Grocke et al., 2017). Such eruptions are also prevalent in certain arcs with continental-type crust, such as Sumatra Island (Indonesia) (e.g., Chesner, 1998) and Honshu Island (Japan) (Yoshida et al., 2014). In contrast, island arcs formed on oceanic crust generally do not exhibit evidence of large-scale caldera eruptions. However, explosions accompanied by the formation of calderas measuring up to 10 km in diameter and erupting volumes reaching hundreds of cubic kilometers are common occurrences in these eruptions, capable of impacting the global climate and environment in certain cases (e.g., Oppenheimer, 2003). Therefore, it is crucial to understand the causes and conditions that lead to powerful eruptions in young volcanic arcs. However, the origins of such eruptions remain poorly constrained and requires further research.

The southern Great Kuril Island Chain (Chishima Islands), serves as an excellent example of an island arc developed on a crust characterized by an immature felsic portion.

Within the southern Kuril Island Arc, multiple caldera eruptions have occurred during the Pleistocene and Early Holocene periods (Bazanova et al., 2016). Kunashir Island, situated in the southern Kurils, is home to two calderas. However, previous petrological studies on Kunashir Island have primarily focused on its early tectonic history, Miocene-Pleistocene basaltic volcanism, and fumarolic activity. Among the studied volcanoes, Tyatya stands out due to its recent eruption in 1973 (e.g., Martynov et al., 2005, 2010a,b; De Grave et al., 2016; Kalacheva et al., 2017a,b; Martynov & Martynov, 2017; Taran et al., 2018; Zharkov, 2020). Despite covering a significant portion of the island, caldera eruptions involving siliceous magma with andesitic and dacitic compositions have received limited research attention.

Conducting investigations on these eruptions is crucial as they can provide valuable insights into the nature of large-scale explosions within volcanic arcs that possess immature or absent felsic crusts, such as certain regions of the Kuril and Aleutian arcs. Results described here represents the first petrological investigation specifically focusing on the origin and evolution of dacitic magma responsible for one of the most significant explosions in the Kuril Islands during the Late Pleistocene.

2.2. Geological settings

Kunashir is the southwestern most and one of the largest (123 km long and 1490 km²) islands of the Kuril Island Arc. The island is located on the convergent boundary of the Pacific and Okhotsk lithospheric plates. The subduction in the southern part of the arc is oblique (WNW direction), with a rate of plate convergence perpendicular to the dip of the slab of 7.7 cm/yr (Syracuse et al., 2010). Lavas and pyroclastic rocks formed by submarine eruptions during the middle Miocene are the oldest volcanic rocks of the island. Detailed descriptions of aspects of the geological history of the island have been given by (Gorshkov, 1967; Piskunov, 1987; Laverov et al., 2005; De Grave et al., 2016; Martynov et al., 2017; Kotov et al., 2023).

The volcanic activity of Kunashir Island during the Pleistocene–Holocene has occurred in four large volcanic centers: Tyatya (1819 m), Rurui (1485 m), Mendeleev (886 m), and Golovnin (541 m) volcanoes (Fig. 2.1). The neighboring Tyatya and Rurui volcanoes form the northern part of the island. Volcanic activity in the northern part has been almost continuous since the Pleistocene. The geochemical compositions of the eruptive rocks vary from basaltic to andesitic.

The Golovnin caldera and its pyroclastic flow deposits constitute the southern part of the island. Pyroclastic flow deposits of this caldera eruption contain non-welded tuffs and

pumice of dacitic and andesitic compositions. The caldera reaches 7 km in diameter, and precaldera rocks are andesites and basalts. The ^{14}C age of the caldera eruption is 41 ka, and the erupted volume has been estimated at 15 km^3 DRE (Bazanova et al., 2016). Postcaldera andesitic lava domes have been extruded in the central part of the caldera. At present, the volcano exhibits active fumarolic activity (Zharkov, 2020).

The primary focus of this study revolves around Mendeleev volcano, situated near the center of Kunashir Island (see Fig. 2.1). The eruption under investigation, which occurred approximately 39-41 thousand years ago (referred to as "40 ka" hereafter), represents a relatively young caldera eruption. The estimated volume of erupted material amounts to 60 cubic kilometers of dense rock equivalent (DRE) (Braitseva et al., 1995; Bazanova et al., 2016). Such a substantial volume of erupted material positions this eruption as one of the largest in the Kuril Islands throughout the Pleistocene and Holocene periods. The caldera deposits consist of non-welded tuffs and pumice characterized by dacitic and rhyolitic compositions. These pyroclastic deposits extensively cover the central part of the island, with outcrops of caldera eruption pyroclastic flows reaching heights of up to 15 meters. Precaldera formations consist of andesitic and basaltic andesite lavas. In addition to the caldera-forming eruption, several extrusive domes (approximately 20) have formed due to syn- and postcaldera volcanism, both within the 40 ka caldera and its periphery. Among these domes, Mechnikov volcano, located on the caldera's edge, consists of basaltic andesite and basalt, while Mendeleev volcano represents a recent dome situated within the caldera.

Geophysical investigations conducted by (Zlobin et al., 1997) have provided insights into the crustal structure beneath Mendeleev volcano. The Moho discontinuity is identified at depths of approximately 22-27 kilometers. Within the crust, several domains exhibiting either complete or partial absence of S-waves, indicative of potential magmatic reservoirs, have been identified at various levels. One of these inferred partially molten domains lies directly beneath the modern Mendeleev volcano at depths ranging from 3 to 10 kilometers. Additionally, smaller domains have been detected in the lower crust and below the Moho discontinuity. These observations suggest the presence of a vertical series of domains with restricted wave propagation beneath Mendeleev volcano, interpreted as interconnected crustal magma reservoirs constituting part of the volcano's plumbing system.

2.3. Sample selection and preparation

For the present study, pyroclastic deposits of the 40 ka caldera eruption were sampled on the southern and western shores of Lagunnoe (Lagoon) Lake (Fig. 2.1b, red square), where

they have the largest outcrop thickness. The studied outcrops represent thick (5–12 m) sequences composed of pumice flow and pyroclastic density current deposits (Fig. 2.1c). Up to three pumice layers divided by finer tephra (from coarse ash to lapilli) deposits were documented. Pyroclastic material dominates over lithic material in the layers. Only fresh pumices from pumice flow deposits were collected for this study. The contact between the syncaldera extrusive dome and pyroclastic deposits was observed on the western shore of Lagunnoe Lake. A wide vitreous contact zone divides the pyroclastic deposits and the extrusive body, indicating that the latter was extruded after the emplacement of pyroclastic layers and, therefore, belongs to a syn- or postcaldera events.

Mendeleev caldera pyroclastic deposits do not form thick exposed outcrops anywhere. This is attributed to the fact that most of the pyroclastic flow has gone into the sea. Kunashir Island in the Pleistocene was presented by several independent small volcanic islands. Subsequent voluminous felsic volcanism filled the straits between these islands, leading to the consolidation of the island.

Samples of proximal pumice and tuffs were collected directly from caldera deposit outcrops located on the southwestern shore of Lagunnoe Lake (Okhotsk Sea side, 8 km north of the modern Mendeleev volcano). Samples of syncaldera extrusions that intruded caldera deposits were taken from two extrusion domes on the western shore of Lake Lagunnoe on the coast of Pervukhina Bay (Fig. 2.1d). Each pumice chunk was studied as a separate sample to minimize the possible influence of co-eruptive magma mixing, assuming that single clasts should be least affected by eruptive mixing (Schuraytz et al., 1989). Thin sections were made for petrographic analysis to study phenocryst assemblages and abundances. We collected several BSE photos of each sample and stitched them together to create photomicrograph mosaics with composite fields of view approaching 20 mm. ImageJ software (https://imagej.nih.gov/ij/) has been used to process the images and determine the modal abundances of minerals, pores, and groundmass glass.

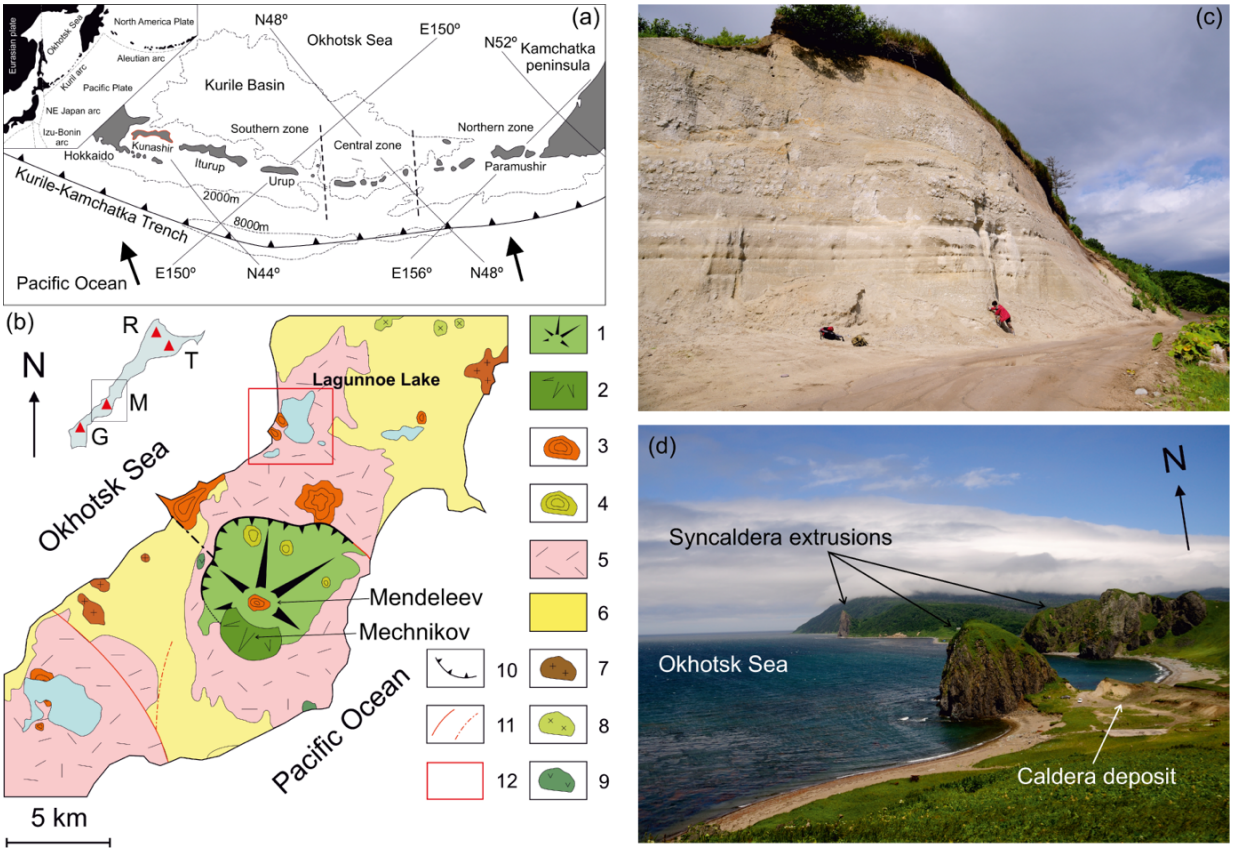

Fig. 2.1. (a) Map of the Kuril–Kamchatka arc system (modified after Martynov & Martynov, 2017). Thick black arrows indicate direction of the Pacific plate movement. (b) Geological map (modified after Rotman, 2000). 1, Pleistocene basalts and andesites of the Mendeleev modern cone; 2, Pleistocene basalts of the Mechnikov dome; 3, Pleistocene and Holocene extrusions of rhyolite, rhyodacite, and dacite; 4, Pleistocene extrusion of andesite; 5, Pleistocene dacitic caldera deposit; 6, Pliocene–Pleistocene volcanic sedimentary rocks; 7, Pliocene–Miocene and Miocene extrusions of rhyodacite and dacite; 8, Pliocene–Miocene and Miocene extrusions of andesitic composition; 9, Miocene and Miocene–Pleistocene extrusions of basalt; 10, Caldera rim (40 ka); 11, faults; 12, Sample collection area. R, Rurui volcano; T, Tyatya volcano; M, Mendeleev volcano; G, Golovnin volcano. (c) Photo shows an outcrop of caldera-forming pyroclastic f low deposits on the southern shore of Lagunnoe. A human for scale. (d) Photo shows several extrusive domes breaking through caldera deposits on the isthmus between Lagunnoe Lake and the Okhotsk Sea.

2.4. Whole-rock compositions

Compositions of pumice and extrusive rocks collected from the shore of Lagunnoe Lake are shown in (Fig. 2.2 a–c) and compared with other Kunashir volcanic rocks and similar pumice deposits from the neighboring islands of Iturup and Hokkaido. Pumices of the 40 ka Mendeleev caldera eruption are classified as low-K (K_2O < 1.0 wt.%) dacites (SiO_2 = 65–66 wt.%) according to their major-element compositions, whereas syncaldera extrusive dome rocks classified as low-K rhyolites (K_2O = 1.1 wt.% and SiO_2 = 71–73 wt.%) (Supplementary Table 2.1). Both caldera pumices and syncaldera extrusions contain 13.0–14.6 wt.% of Al_2O_3 and plot on or near the boundary between metaluminous and peraluminous compositions (Fig.

2.2b). An important feature of the pumice and syncaldera extrusion rock compositions is the high CaO contents (4.1–4.2 wt.% for pumice, 3.0 wt.% for dome rocks), which are almost equal to the total major-alkalis ($Na_2O + K_2O$ = 4.4–5.2 wt.%), classifying these rocks as calcic felsic rocks (Fig. 2.2e). The compositions of pumices and the dome rocks exhibit similar trends, indicating that both may have originated from the same magmatic source (Fig. 2.2a, c-e). In terms of silica content, the pumices are similar to those that erupted during the Late Pleistocene Vetrovoy Isthmus and Lvinaya Past' Bay events on the neighboring Iturup Island. However, the pumices have lower total alkali and K contents and higher aluminosity, as measured by the A/NK [molal $Al_2O_3/(Na_2O + K_2O)$] index (Fig. 2.2b). Compared with pumices from the Kutcharo caldera complex on Hokkaido Island, Japan, pumices from the Mendeleev caldera have similar SiO_2 contents but substantially lower total alkali and K contents and A/NK aluminosity.

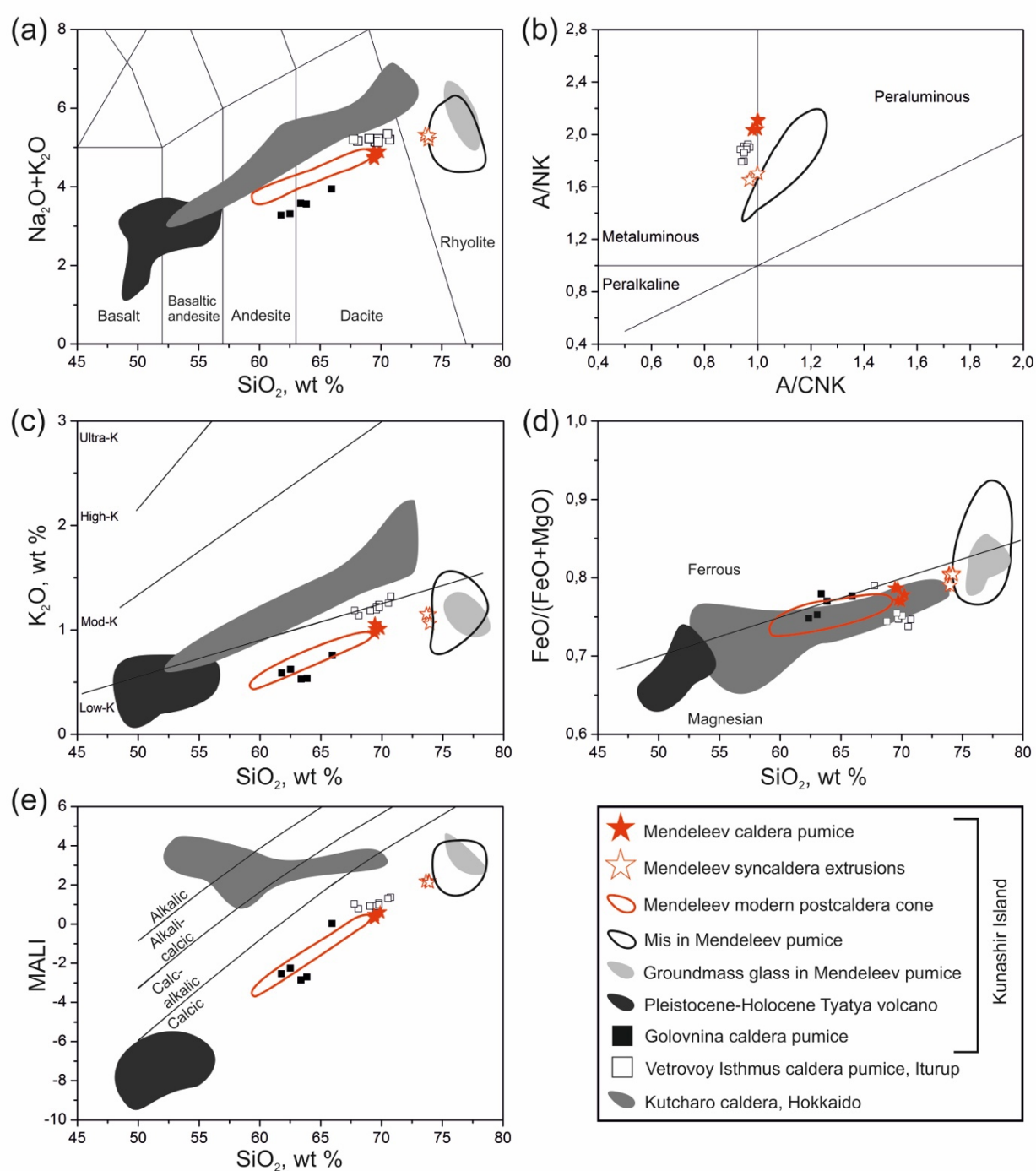

Fig. 2.2. Whole-rock compositions of the modern pyroclastic deposits from Kunashir Island pyroclastic deposits on the Kunashir, Iturup, and Hokkaido Islands. Classification diagrams of (a) $Na_2O + K_2O$ versus SiO_2 (Bas et al., 1986), (b) A/NK versus A/CNK (Shand, 1943), (c) K_2O versus SiO_2 (Rickwood, 1989), and (d and e) $FeO/(FeO + MgO)$ versus SiO_2 and MALI versus SiO_2 (Frost et al., 2001). Compositions of Vetrovoy Isthmus caldera deposits (Iturup Island) are from (Smirnov et al., 2019), those for Tyatya Volcano (Kunashir Island) are from (Martynov & Martynov, 2017), those for the Kutcharo caldera deposits (Hokkaido Island) are from (Hoang et al., 2011), and the Golovnin caldera deposit compositions (Kunashir Island) are unpublished data. All data are volatile free and normalized to 100 wt%. A/CNK = $(Al_2O_3/101.96)/(CaO/56.08 + Na_2O/61.98 + K_2O/94.2)$; A/NK = $(Al_2O_3/101.96)/(Na_2O/61.98 + K_2O/94.2)$; MALI = $Na_2O + K_2O - CaO$.

2.5. Mineralogy and petrography of caldera pumice and syncaldera extrusions

Pumices from the pyroclastic deposits of the 40 ka Mendeleev caldera eruption are fresh gray porous rocks ranging from lapilli size up to 30–40 cm across. Pumices contain abundant phenocrysts and glomerophyric clots, which are set into a glassy vesicular matrix (GM) that contains almost no microlites. Glassy GM varies from 71 to 77 vol.% (excluding voids). Phenocrysts and glomerophyric assemblages constitute 23–29 vol.% of the pumices (total crystallinity, excluding voids) and are composed mainly of plagioclase (59–71 vol.%), orthopyroxene (8-14 vol.%), and clinopyroxene (10–16 vol.%), with subordinate Fe–Ti oxides (Ti-magnetite and ilmenite; 5–8 vol.%) and rare quartz (1–3 vol.%) (Supplementary table S2)

Syncaldera extrusions are composed of vitreous, massive rocks that have a fluidal texture. The mineral assemblage of the syncaldera domes is completely derived from that of pumice, but the former contain more quartz. Total crystallinity for the syncaldera extrusions range between 31-34 vol.%. Modal abundance of plagioclase varies within 60-62 vol.% of the total crystallinity, orthopyroxene make up 4-7 vol.%, clinopyroxene 4-6 vol.%, Fe–Ti oxides 2-3 vol.%, while quartz 25-27 vol.%, respectively. Differences in the modal abundances of extrusive domes and pumice indicate that modes of quartz increased in extrusions, whereas of plagioclase slightly decreased, pyroxenes and oxides decreased significantly. This indicates that only plagioclase and quartz crystallized at the stage of formation of syncaldera extrusions, which is discussed in more detail in the chapter 2.8.2. "Crystallization and magma degassing".

2.5.1. Plagioclase compositions and textures

Plagioclase occurs as individual phenocrysts, aggregates of phenocrysts, and inclusions in pyroxenes and magnetite. The most common size of plagioclase crystals is ~0.5–2 mm. Phenocrysts larger than 2 mm are rare.

Phenocrysts are usually euhedral and display complex zoning that is typically concentric and patchy. The combination of these patterns defines three types of plagioclase crystal: (I) patchy crystals, (II) concentric/oscillatory-zoned crystals, and (III) complex crystals with patchy core and concentric outer parts.

The patchy pattern of type I crystals is shown in SEM BSE images (Fig. 2.3b–e) and comprises irregularly distributed roughly rectangular patches. These patches are both dark and light in SEM BSE images. Dark patches have andesine composition with An mol% = 50–58, whereas light patches vary from bytownite to anorthite (An mol% = 84–94). Plagioclase phenocrysts with oscillatory concentric growth patterns (type II crystals) dominate the mineral

assemblage (Fig. 2.3a). Different zones of such crystals vary irregularly within An mol% = 41–60. Very rarely we have observed non-patchy normally zoned crystals with cores of An mol% 80-83 and rims of An mol% 48–58. Phenocrysts with complex zoning (type III crystals) have a patchy core similar to type I crystals and oscillatory outer rims similar to type II crystals. In some cases, the cores of phenocrysts with complex zoning preserve crystallographic outlines. The composition of plagioclase at the boundary between the outer and inner parts of crystals changes abruptly from An mol% = 84–81 to An mol% = 65–52 (Fig. 2.3b–d). The outermost concentric zones of the plagioclase phenocrysts always have An mol% = 48–58.

Patchy (type I) plagioclases tend to host considerably more inclusions compared with the other two types. Inclusions of clinopyroxene, Ti-magnetite, and rare orthopyroxene are found in the low-Ca (dark) domains (Fig. 2.3d–e) of patchy crystals. Inclusions of very rare clinopyroxene, rare magnetite crystals, and extremely rare amphiboles (<2–3 μm) are found in the high-Ca domains. As a rule, oscillatory-zoned plagioclases contain fewer inclusions than patchy plagioclases, even where both are observed in the same type III crystals. Oscillatory-zoned plagioclase hosts rare inclusions of apatite, ortho- and clinopyroxene, magnetite, and ilmenite. The number of inclusions decreases outward with decreasing content of Ca in the host plagioclase.

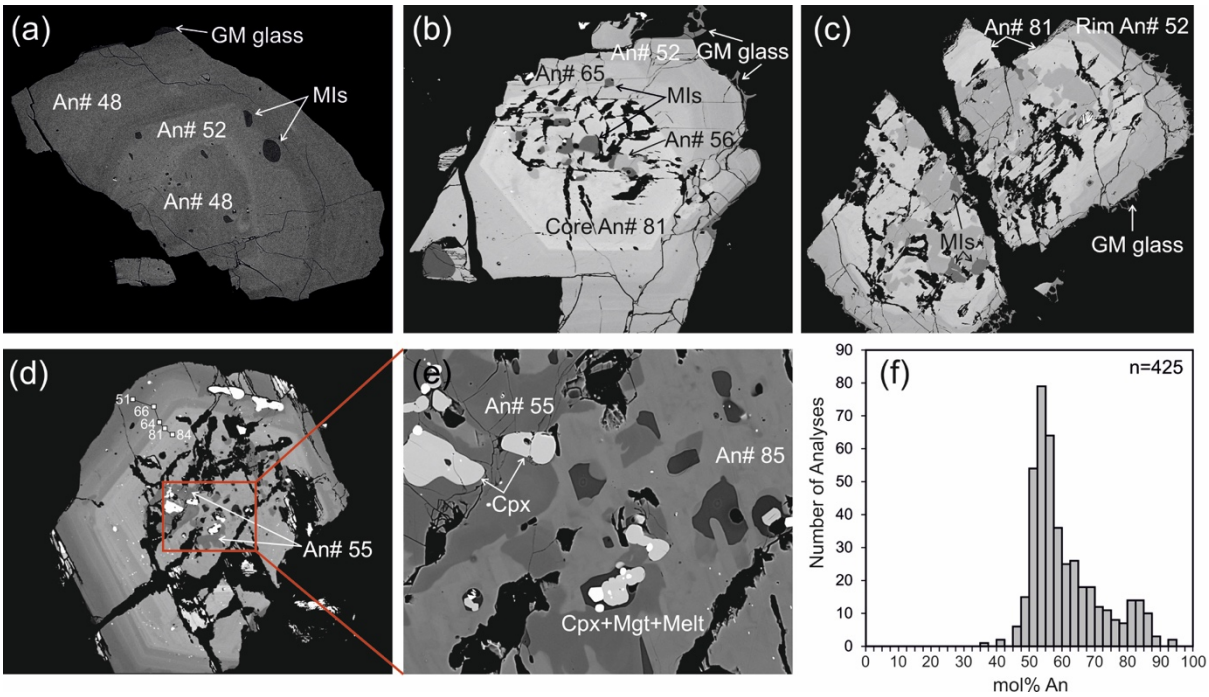

Fig. 2.3. BSE images of plagioclase phenocrysts: (a) Plagioclase with low-contrast zoning (Type I); (b–d) combination of patchy and concentric growth zonation in plagioclase (Type III); (e) zoomed image of the central part of the plagioclase phenocryst from image (d), showing the confinement of inclusions to andesine patches; (f) histogram of plagioclase compositions. An mol% = [XCa /(XCa + XNa + XK)×100]. Cpx, clinopyroxene; Mgt, Magnetite; MIs, melt inclusions; GM glass, groundmass glass.

Plagioclase phenocrysts contain ubiquitous inclusions of parental melts both in cores and outer rims. Many phenocrysts host primary fluid inclusions, most of which are confined to patchy cores. Qualitative study by Raman spectroscopy revealed that these inclusions at room temperature consist of aqueous liquid and rarely low-density CO_2 vapor (< 0.015 g/cm^3), determined based on the splitting of the Fermi diad (Mironov et al., 2020).

2.5.2. Clinopyroxene

Clinopyroxene forms individual euhedral and subhedral crystals (Fig. 2.4a) and clusters with Fe–Ti oxides, plagioclase, and orthopyroxene. The clinopyroxene is classified as augite, with Mg# = 71–78 (Fig. 2.5a) (Morimoto, 1988). The composition of clinopyroxene varies in a narrow range ($Wo_{42–45}En_{39–44}Fs_{12–16}$). Clinopyroxene phenocrysts do not show significant compositional variations. Mg# values typically vary by only 1-3 units in an individual crystal. Mg# is positively correlated with SiO_2 content (51.0–53.7 wt.%) and inversely with Al_2O_3 (0.9–2.6 wt.%) and TiO_2 (0.1–0.6 wt.%).

Augite inclusions are abundant in the patchy plagioclase, but rare in other minerals. All clinopyroxene inclusions exhibit a composition similar to that of the phenocrysts. The prevalent mineral inclusions within augite are plagioclase, magnetite, ilmenite, orthopyroxene, amphibole, and apatite. Augite, plagioclase (An mol% = 45-86), and magnetite often form glomerophyric clots, which are widely distributed. Clinopyroxene within these clots typically contain numerous inclusions of amphibole, orthopyroxene, and rhyolitic glass. It is worth noting that augite originating from clots contains a higher abundance of amphibole inclusions in comparison to augite phenocrysts. The compositions of orthopyroxene inclusions within augite are same to those observed in orthopyroxene phenocrysts.

The most common mineral inclusions in augite are plagioclase, magnetite, ilmenite, orthopyroxene, amphibole, and apatite. Glomerophyric clots of augite, plagioclase (An mol% = 45–86), and magnetite are ubiquitous. Clinopyroxene in such clots typically contains abundant inclusions of amphibole and orthopyroxene together with rhyolitic glass. It is observed that augite from clots contains more amphibole inclusions compared with augite phenocrysts. The compositions of orthopyroxene inclusions in augite are similar to those of orthopyroxene phenocrysts.

2.5.3. Orthopyroxene

Orthopyroxene forms euhedral crystals measuring up to 2 mm in size (Fig. 2.4b). According to the IMA classification, the orthopyroxene compositions fall into the enstatite field ($Wo_{2–4}En_{63–69}Fs_{29–34}$; Fig. 2.5a; Morimoto, 1988), with Mg# 65–74. The majority of orthopyroxene phenocrysts have homogeneous Mg-hypersthene compositions without zoning pattern, and only few crystals have weak normal zoning with a difference between core and rim no more than 5 Mg# units. Mg# values are positively correlated with SiO_2 (51.7–54.5 wt.%) and inversely with MnO (0.6–1.5 wt.%). The Al_2O_3 (0.5–1.7 wt.%) and TiO_2 (0.1–0.3 wt.%) contents of the enstatite are poorly correlated with Mg#.

The prevalent mineral inclusions within hypersthene consist mainly of apatite, plagioclase (with An mol% ranging from 56 to 81), magnetite, and ilmenite. Inclusions of clinopyroxene within orthopyroxene are infrequent and demonstrate a composition similar to that of augite phenocrysts (characterized by Mg# values of 73-75) as well as inclusions present in plagioclase. Notably, orthopyroxene often forms clots with plagioclase and augite. While irregular amphibole inclusions are found in the orthopyroxene, their prevalence is notably lower compared to their occurrence in clinopyroxene. Similarly to plagioclase pyroxene phenocrysts host abundant inclusions of parental rhyolitic melts and primary fluid inclusions.

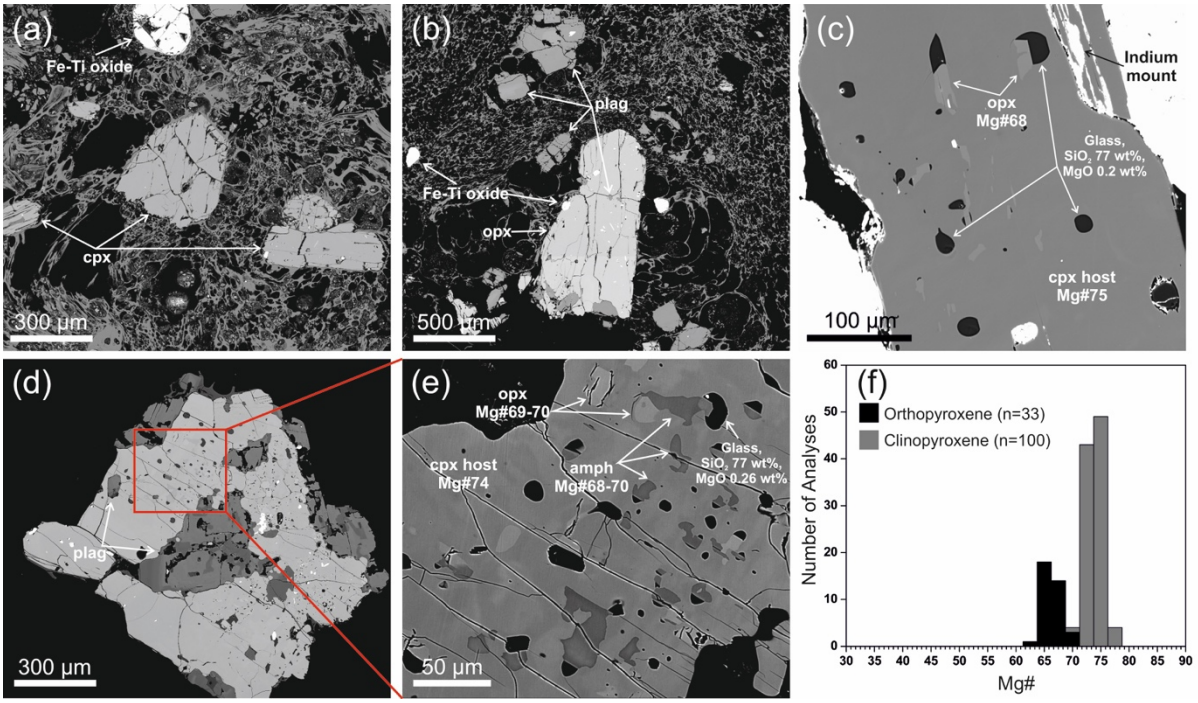

Fig. 2.4. BSE images of the pyroxene phenocrysts: (a and b) Euhedral crystals of augite and enstatite set in groundmass glass; (c) augite phenocryst with enstatite and melt inclusions; (d) plagioclase–enstatite–augite clot; (e) zoomed image of augite phenocryst from panel (d) showing inclusions of Mg-hornblende amphibole together with rhyolitic melt and enstatite; (f) Histograms of pyroxene composition. Mg#=[XMg/(XMg+XFe)×100]. Cpx, clinopyroxene; Opx, orthopyroxene; Plag, plagioclase; Mgt, magnetite; Amph, amphibole.

2.5.4. Amphibole relics

No instances of amphibole phenocrysts were identified within the examined pumice and extrusive dome rocks from the syncaldera. Instead, amphibole is exclusively found as inclusions within the minerals from clots, and most abundant in augite (Mg# of 72-77 and Al_2O_3 content ranging from 1.1% to 2.9%). These amphibole inclusions exhibit melted, anhedral shapes and are commonly found alongside glass inclusions (with SiO_2 content ranging from 74% to 76%) and hypersthene inclusions (with Mg# ranging from 67 to 71). The morphology of these amphibole inclusions, combined with their occurrence within a clinopyroxene, orthopyroxene, plagioclase cores, and Fe-Ti oxide, strongly suggests that these inclusions are vestiges of previously stable amphibole. In less frequent cases, amphibole is encased within orthopyroxene (with Mg# of 68-74) and within high-calcium zones of plagiolcase (An mol% ranging from 82 to 89). These inclusions also often coexist with glass inclusions and can vary from anhedral to more well-defined shapes. The majority of amphibole compositions align with magnesio-ferri-hornblende compositions (as illustrated in Figure 2.5b), exhibiting Mg# values between 63 and 74, Al_2O_3 content ranging from 6.52% to 11.52%, and Na_2O content ranging from 1.27% to 2.19%.

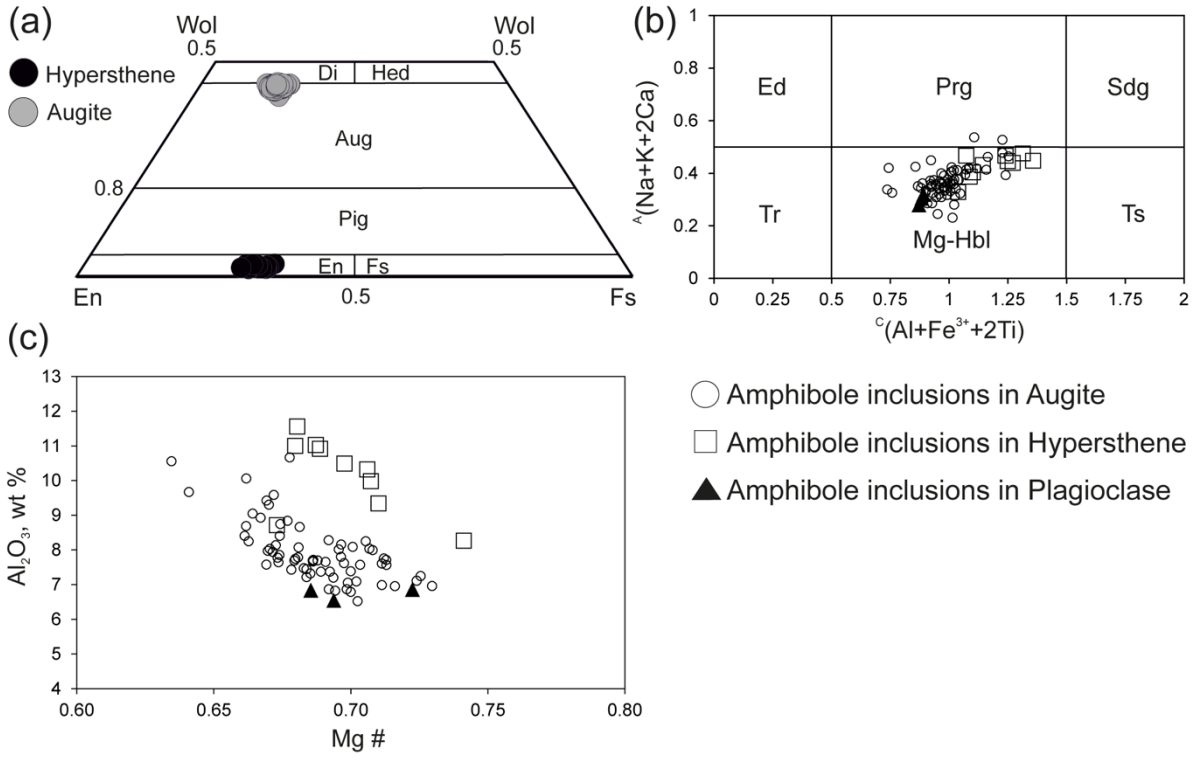

Fig. 2.5. Compositions of mafic minerals in the Mendeleev pumice: (a) Classification of pyroxenes according to (Morimoto, 1988); (b) classification of amphiboles following (Hawthorne et al., 2012); (c)

compositions of amphibole inclusions from pyroxenes. Ed, edenite; Prg, pargasite; Sdg, sadanagaite; Tr, tremolite; Mg-Hbl, magnesio-hornblende; Ts, tschermakite.

2.5.5. Quartz

Quartz typically forms small (<200 μm), rounded phenocrysts set in GM glass. The quartz is usually free of mineral inclusions and rarely contains apatite needles. Quartz does not cluster with other phenocrysts. It contains abundant inclusions of parental melts. Fluid inclusions have never been found even at most thorough microscopic examination.

2.5.6. Fe–Ti oxides

Titanomagnetite and ilmenite crystals are euhedral and have sizes of up to 500 μm. Ilmenite is much rarer than magnetite. Fe–Ti oxides occur as phenocrysts and as inclusions in other minerals. Titanomagnetite and ilmenite are commonly included within the same growth zones in pyroxenes and less commonly in plagioclase. In some cases, titanomagnetite and ilmenite form clusters with pyroxenes. Pairs of intergrowing titanomagnetite and ilmenite crystals are rare. Titanomagnetite contains abundant inclusions of apatite, plagioclase, and rare Fe-sulfides.

The mutual inclusion of Fe-Ti oxides and the ubiquitous intergrowths of ilmenite and titanomagnetite indicate that their crystallization was simultaneous. All of the studied magnetite and ilmenite grains are chemically homogeneous. The compositions of the studied Fe–Ti oxides are typical of arc dacites. Titanomagnetite contains 7.5–8.4 wt.% TiO_2. The main impurities in titanomagnetite include Al_2O_3, V_2O_3, MnO, MgO, Cr_2O_3, and NiO, the contents of which do not exceed the limit of detection in some cases. The main impurities in ilmenite include MgO, MnO, Al_2O_3, and V_2O_3.

2.6. Melt inclusions and groundmass glass

All of the studied minerals contain inclusions of glass. Some of them are sealed microportions of the parental melts, trapped by minerals during their growth, and they are termed “melt inclusions” (MIs). Others form embayed protrusions of the GM glass into magmatic crystals.

In phenocrysts, MIs are distributed either along polygonal growth zones or as compact groups of irregularly scattered inclusions. At room temperature, most MIs consist of transparent colorless or brownish glass only. Less commonly, they contain single or multiple shrinkage bubbles. Only bubble- and crystal free MIs were selected for compositional analyses.

Harker diagrams (Fig. 2.6a–d) can be used to constrain the extent of post-entrapment host-mineral crystallization (PEC) on inclusion walls. The selected elements have variable compatibility with host pyroxenes and plagioclase. When a material that is similar to a particular host mineral is deposited on inclusion walls, the composition of the trapped melt changes in a way, which is specific for this mineral only. Thus, inclusions in different minerals subjected to significant PEC should form different compositional trends intersecting at the composition of the trapped melt (Roedder, 1984). For example, PEC in pyroxene-hosted MIs would result in a shift to very low MgO contents with little change in Al_2O_3, whereas PEC in plagioclase-hosted MIs would lead to a decrease in Al_2O_3 and a slight increase in MgO, producing different trends. (Fig. 2.6a–d) reveals that the compositions of the inclusions form similar trends where contents vary within narrow ranges. Thus, PEC should be considered negligible, meaning that the observed compositional variations MIs can be explained by common regularities of magma crystallization in the reservoir rather than PEC processes. Thus, none of the studied MIs display any evidence of PEC on inclusion walls.

In some cases, MIs in pyroxene, plagioclase, or Fe–Ti oxide minerals contain crystals of other minerals (apatite, clinopyroxene, orthopyroxene, plagioclase, and magnetite). All of these minerals occur as individual inclusions in the host mineral, and their compositions are similar to those of the phenocrystal and glomerophyric mineral assemblages. The similarity of minerals in MIs and host mineral indicates that all of the reported mineral phases are foreign and were trapped simultaneously with the melt. The insignificant PEC allows the composition of the glass of the naturally quenched vitreous MIs to be regarded as an adequate proxy for the composition of the parental melt of the phenocryst minerals.

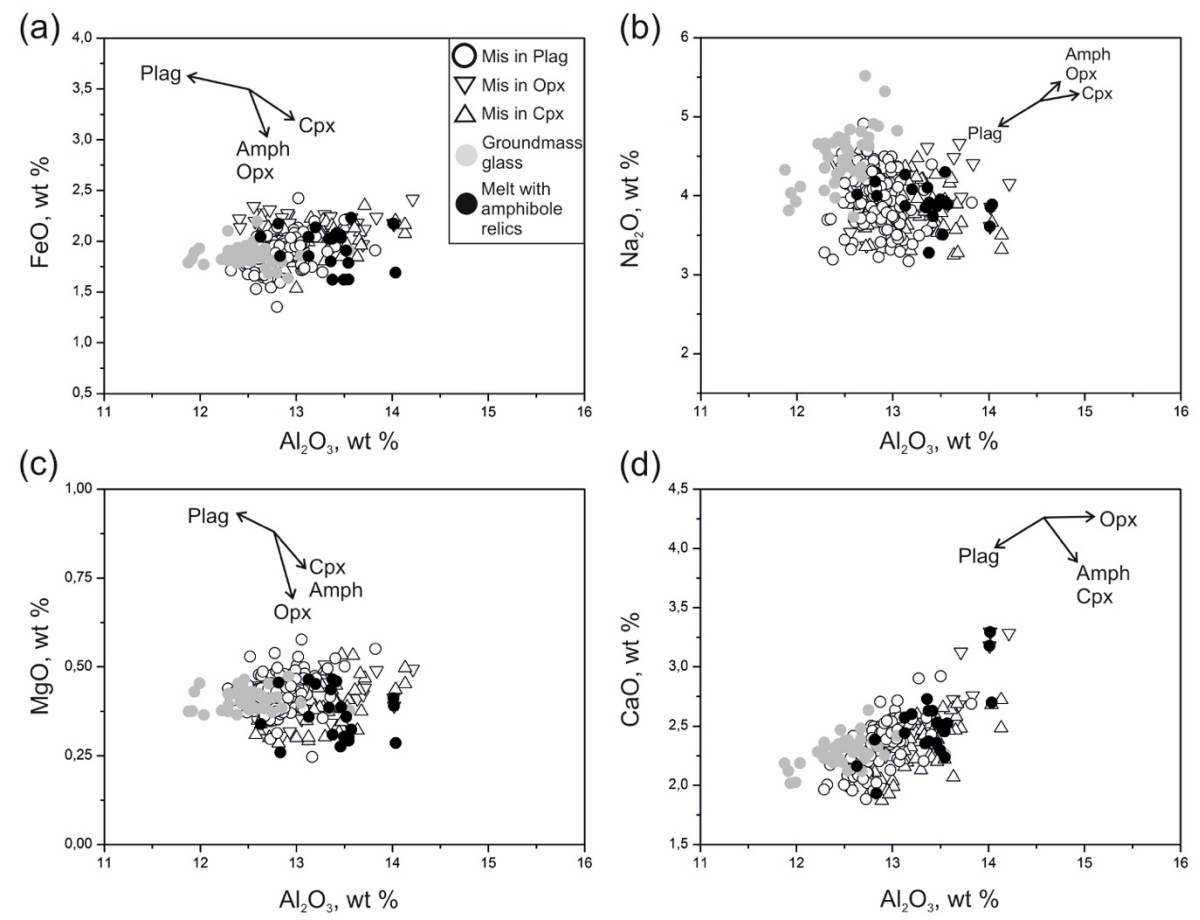

Fig. 2.6. Harker diagrams for the 40 ka Mendeleev pumice MIs. The diagrams show that the chemistry of MIs is independent of the host mineral. Black arrows show the directions of trapped melt evolution owing to PEC in the plagioclase- and pyroxene-hosted melt inclusions. All contents are recalculated on a volatile-free basis and normalized to 100 wt%.

Major-element compositions for MIs are displayed in Figure 2.7 and reported in (Kotov et al., 2023). The compositions of MIs differ from those of the bulk rock for all major elements. The MIs correspond to low-K rhyolite, with $Na_2O + K_2O$ of 4.2–6.2 wt.%, Al_2O_3 of 12.2–14.5 wt.%, and SiO_2 of 74.0–78.4 wt.% (anhydrous). The MIs from different pumice minerals are compositionally similar, which is consistent with a lack of PEC influence on glass compositions. The MI compositions from different pumice samples are also similar, indicating chemical homogeneity of the magma throughout the sampled sequence. It should also be noted that the compositions of MIs trapped together with amphibole relics do not differ from those of other MIs.

GM glass is classified as low-K rhyolite, similar to the glass of MIs. $Na_2O + K_2O$ varies from 4.8 to 6.6 wt.% and SiO_2 from 74.7 to 78.2 wt.% (anhydrous; Fig. 2.7b). The compositions of GM glass overlap the less aluminous range of MI glass, and some of them have even lower aluminosity than MIs (Fig. 2.7a). The major-alkali contents of the GM glass are comparable to

those of bulk rocks. The Na_2O contents of the GM glass are close to the highest measured in MIs, whereas K_2O corresponds to intermediate contents in the MIs (Fig. 2.7g and h). Contents of femic components in GM glass correspond to lower to intermediate concentrations measured in MI glass (Fig. 2.7c–f).

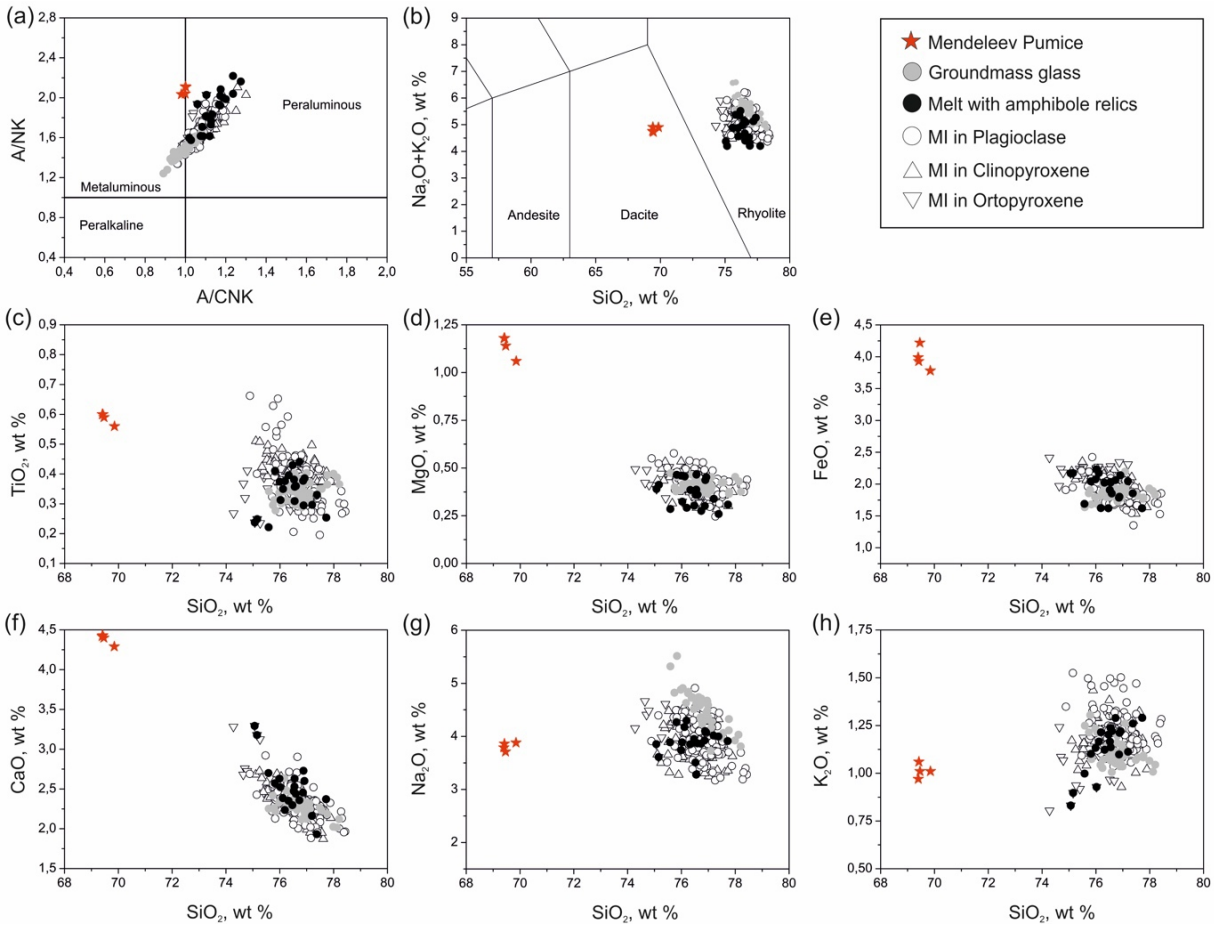

Fig. 2. 7. Variations in major-element contents of MIs. All data are plotted volatile free, summed to 100 wt%.

2.7. Volatile contents of melt inclusions

Contents of volatile elements (H_2O, CO_2, P_2O_5, S, F, and Cl) in the MI glass from pumices were measured using SIMS. Analytical procedure, standard analysis and errors provided in supplementary materials. For comparison, we provide several analyses of GM glass from syncaldera extrusions (Fig. 2.8a–d). H_2O dominates among volatile species in MIs in plagioclases and pyroxenes and varies from 4.2 to 5.8 wt.%. Chlorine contents vary within 0.15–0.25 wt.% and are positively correlated with F contents, which range from 383 to 483 ppm. Variations in H_2O, Cl, and F are generally greater in MIs hosted in plagioclase relative to those hosted in other minerals.

Contents of other magmatic volatiles are substantially lower than those reported above for H_2O, Cl, and F. Contents of phosphorus and sulfur are similar (109–279 and 69–179 ppm, respectively), and CO_2 contents are negligible (<14 ppm).

Volatile contents of the quartz-hosted MIs and GM glass of the syncaldera extrusions differ from those of MIs in plagioclase and pyroxene phenocrysts. The H_2O contents in quartz-hosted MIs are lower than those in plagioclase- and pyroxene-hosted MIs and vary from 3.28 to 4.14 wt.%. H_2O contents in the GM glass are even lower at 0.57 wt.%. Chlorine contents in quartz-hosted MIs (0.22–0.24 wt.%) are similar to those in plagioclase- and pyroxene-hosted MIs, whereas the syncaldera extruions GM glass is slightly depleted in Cl (0.15–0.16 wt.%) compared with all MIs. Contents of H_2O and chlorine are positively correlated for all of the studied glasses. Fluorine contents in the quartz-hosted MIs and syncaldera extrusions GM glass are similar at 449–502 and 472–497 ppm, respectively.

Similar to plagioclase- and pyroxene-hosted MIs, the contents of other volatiles in quartz-hosted MIs and syncaldera GM are lower than those of H_2O, Cl, and F. However, the quartz-hosted MIs and GM glass are enriched in phosphorus, with contents of P varying from 165 to 168 ppm in quartz-hosted MIs and from 183 to 188 ppm in syncaldera dome rock GM.

The quartz-hosted MIs contain 11–17 ppm CO_2 and 45–52 ppm S. In the dome rock glass, these volatiles fall close to or below the detection limits of SIMS. Phosphorus contents are positively correlated with both Cl and F contents. In general, the volatile contents of Mendeleev MIs are similar to those of high-Si MIs from the SW Hokkaido–SE Kuril felsic volcanoes. On average, rhyolitic MIs in dacites of this region have 3–7 wt.% H_2O (mean 4.5–5 wt.%), very low CO_2 and S contents (<50 and <250 ppm, respectively), 0.1–0.4 wt.% Cl, and up to 0.18 wt.% F (Miyagi et al., 2012; Smirnov et al., 2019; Kotov et al., 2021). Data from (Miyagi et al., 2012) data suggest that rhyolite MIs from Kutcharo–Mashu caldera complex (Hokkaido Island) have a somewhat wider range of halogens relative to the rhyolites of the southern Kurils.

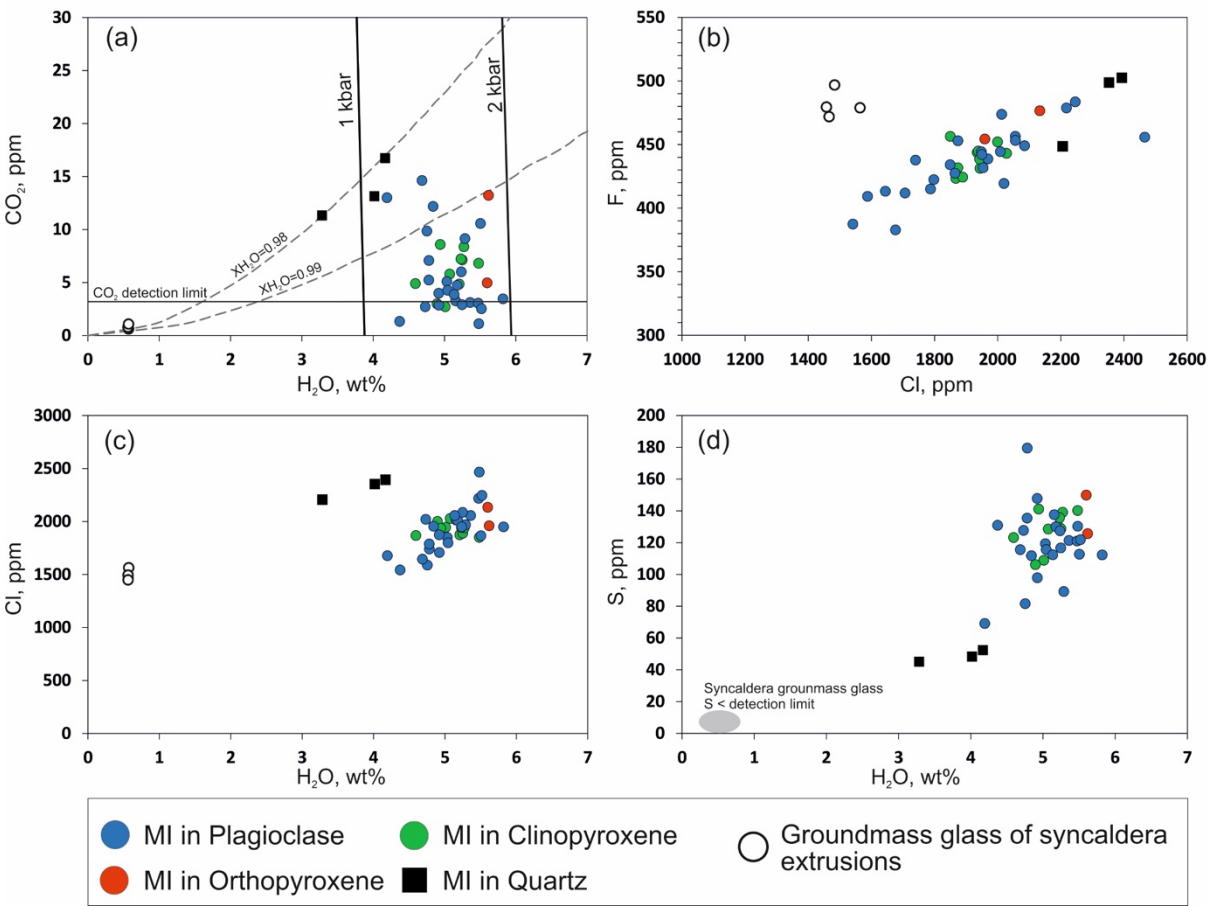

Fig. 2.8. (a–d) Diagrams of volatile compositions of MIs in pumice minerals and GM glass of syncaldera extrusive domes. Isobars and isopleths for CO_2 versus H_2O were plotted using VolatileCalc 2.0 (Newman & Lowenstern, 2002) for 850◦C (average temperature for MI formation based on mineral-liquid thermometry, see paragraph 'Pressure, temperature, and redox properties of the pre-eruptive magma').

2.8. Discussion

2.8.1. Mineral assemblages and pre-eruptive melt compositions

To describe a sequence of crystallization of the mineral assemblage we will use a two-stage model based on the observation of mineral zoning and mutual occurrence of minerals in each other in the form of mineral inclusions: 1) an "early" assemblage includes patchy plagioclase, clino- and orthopyroxene, Fe-Ti oxides and relics of amphibole in pyroxenes and plagioclase cores; 2) a "late" assemblage includes quartz and plagioclase with An mol% 50-60 (Kotov et al., 2023)

Crystallization of plagioclase starts from An mol% = ~55 and is subsequently replaced by plagioclase with An mol% of up to 80–94. This replacement leads to the formation of plagioclase crystals with patchy texture. The composition of plagioclase at the boundary between the outer part and such patchy cores changes abruptly from An mol% = 84–81 to 65–52 (Fig. 2.3b–d). In later growth zones anorthite content decreases gradually outward to 60–50

An mol% and normal oscillatory zoning forms. The An mol% of the latest-formed plagioclase varies from 50 to 60.

The mineral zoning observed in plagioclase offers valuable insights into the sequence of events leading up to the eruption of the Mendeleev caldera 40 thousand years ago. The initial formation of andesine (An mol% 50-58) occurred concurrently with augite, hypersthene, and Fe-Ti oxides. However, the exact nature and origin of this mineral assemblage remain uncertain. While these minerals are typically interpreted as the earliest products of magma solidification, the possibility of an external source cannot be ruled out. The early plagioclase assemblage underwent destabilization and was subsequently replaced by more calcic plagioclase, as previously described. During this stage, plagioclase was found in association with augite, enstatite, and remnants of Mg-hornblende. These remnants were also observed within high-Ca plagioclase growth zones. This association can be explained by the dehydration reaction of amphibole and subsequent breakdown, resulting in the formation of a mineral assemblage consisting of plagioclase, clinopyroxene, and orthopyroxene. Such an assemblage is commonly observed during partial melting of amphibole-bearing substrates (Blatter et al., 2017; Smirnov et al., 2019; Kotov et al., 2023).

In this context, two pyroxenes and plagioclase can be considered as residual phases resulting from the reaction, as they did not directly crystallize from the melt. The uniform compositions of the pyroxene crystals and the high-silica rhyolitic composition of the MI glass support this interpretation. The significance of amphibole in the formation of the 40 ka Mendeleev magma is discussed in more detail in the following section titled "Amphibole relics as evidence of magma genesis" (section 2.8.4).

The mineral compositions observed in the pumices of the 40 ka Mendeleev caldera eruption exhibit similarities to those described for the 20 ka dacitic pumices found on Iturup Island's Vetrovoy Isthmus. In a publication of (Smirnov et al., 2019), an initial assemblage consisting of two pyroxenes and early-stage plagioclase, followed by a subsequent assemblage of late-stage plagioclase and quartz, was identified. The phenocryst mineral assemblage in the 40 ka Mendeleev dacitic pumices closely corresponds to the early-stage assemblage found in the Vetrovoy Isthmus pumices. However, the occurrence of the later quartz-plagioclase assemblage in the 40 ka Mendeleev pumices is relatively rare compared to the 20 ka Vetrovoy Isthmus pumices. This observation suggests that a two-step sequence of phenocryst crystallization may be a common feature in magma reservoirs associated with caldera-forming eruptions in the southern Kuril Island Arc.

Our data indicates that the pre-eruptive magma of the 40 ka Mendeleev caldera eruption consisted of a mixture of residual minerals, minerals formed from the melt, and low-K peraluminous to metaluminous calc-alkaline rhyolitic melts. The Harker diagrams in Figure 6 exhibit a significant positive correlation between CaO and Al_2O_3, while a weaker negative correlation is observed between Na_2O and Al_2O_3. On the other hand, the variations in MgO and FeO relative to Al_2O_3 do not show distinct patterns. Among these elements, Al_2O_3 demonstrates the most significant variation in content and can be used as an indicator of the progression of crystallization. Figure 2.6 illustrates that Al_2O_3 content decreases as crystallization advances towards a GM (glass-matrix) composition. The correlations between Al_2O_3 with CaO and Na_2O, and the lack of correlations with FeO and MgO, suggest that the melt composition was primarily influenced by plagioclase crystallization and minimally affected by pyroxene crystallization. This interpretation aligns with the identification of a later assemblage of phenocrysts (late plagioclase and quartz) that formed directly from the melt without undergoing any reactive processes.Narrow ranges of compositional variations indicate that most of the studied minerals formed as a result of amphibole breakdown or direct crystallization from the melt, which was cogenetic with the rhyolitic melt represented by Mis. The compositional homogeneity of femic minerals and the uniform rhyolitic compositions of Mis in both the early (reactional) and late minerals show that fractional crystallization and derivation of felsic melts from mafic magmas were unimportant in the formation of magma involved in the 40 ka Mendeleev caldera eruption. Possible alternative scenarios of magma generation are discussed below.

2.8.2. Crystallization and magma degassing

The correlations between H_2O and major elements provide insights into the relationship between degassing and magma crystallization during different stages of magmatic evolution. In cases where extensive degassing is driven by decompression during crystallization, H_2O contents should exhibit a positive correlation with compatible elements but a negative correlation with incompatible elements (e.g., Wallace & Anderson, 1998; Lloyd et al., 2012; Barth et al., 2019; Barth & Plank, 2021). Figure 2.9 illustrates the covariations of major elements with H_2O for scenarios involving isobaric crystallization of water-saturated melts, isobaric crystallization of water-undersaturated melts, and rapid syneruptive degassing, following the work of (Blundy & Cashman, 2005).

Figure 2.9 reveals that the crystallization of plagioclase and pyroxenes was accompanied by slight decompression and degassing, consistent with our interpretation that the magmatic

system involved in the generation of the 40 ka Mendeleev caldera dacitic magma was extending to depth. The decrease in H_2O content alongside decreasing CaO and MgO contents aligns with the simultaneous crystallization of plagioclase and pyroxene. The weak positive correlation between H_2O and P_2O_5 can be attributed to extensive crystallization of apatite. However, this correlation might be apparent due to the wide range of H_2O contents and low phosphorus contents present in the initial melts.

Generally, a negative correlation between H_2O and K_2O is expected in degassing magma, as K is typically incompatible in arc-front magmas. However, this anticipated correlation is not evident in the presented data (Fig. 2.9e). Upon examining Figure 2.7h, it becomes apparent that the K_2O contents of MIs and GM glass do not show significant differences. The lack of an H_2O-K_2O correlation can be attributed to the distinct compatibility of K with respect to the major pumice minerals, namely pyroxene and plagioclase. While potassium tends to be incompatible with pyroxene and high-Ca plagioclase, its compatibility increases as the Ca content of plagioclase decreases during the late stages of pre-eruptive magma crystallization. This trend likely masks the initially expected negative correlation between H_2O and K_2O. Consequently, absolute variations in K_2O in a melt in this case should be relatively small, as any increase in K_2O due to pyroxene crystallization will be offset, or even exceeded, by its incorporation within plagioclase as the Ca content decreases.

The presence of primary fluid inclusions in the pumice plagioclase and clinopyroxene suggests that the 40 ka Mendeleev caldera magma was already saturated with H_2O during pre-eruptive crystallization. Moreover, the slight decrease in H_2O contents indicates that the magma experienced a gradual degassing due to slight decompression during the late stage of crystallization.

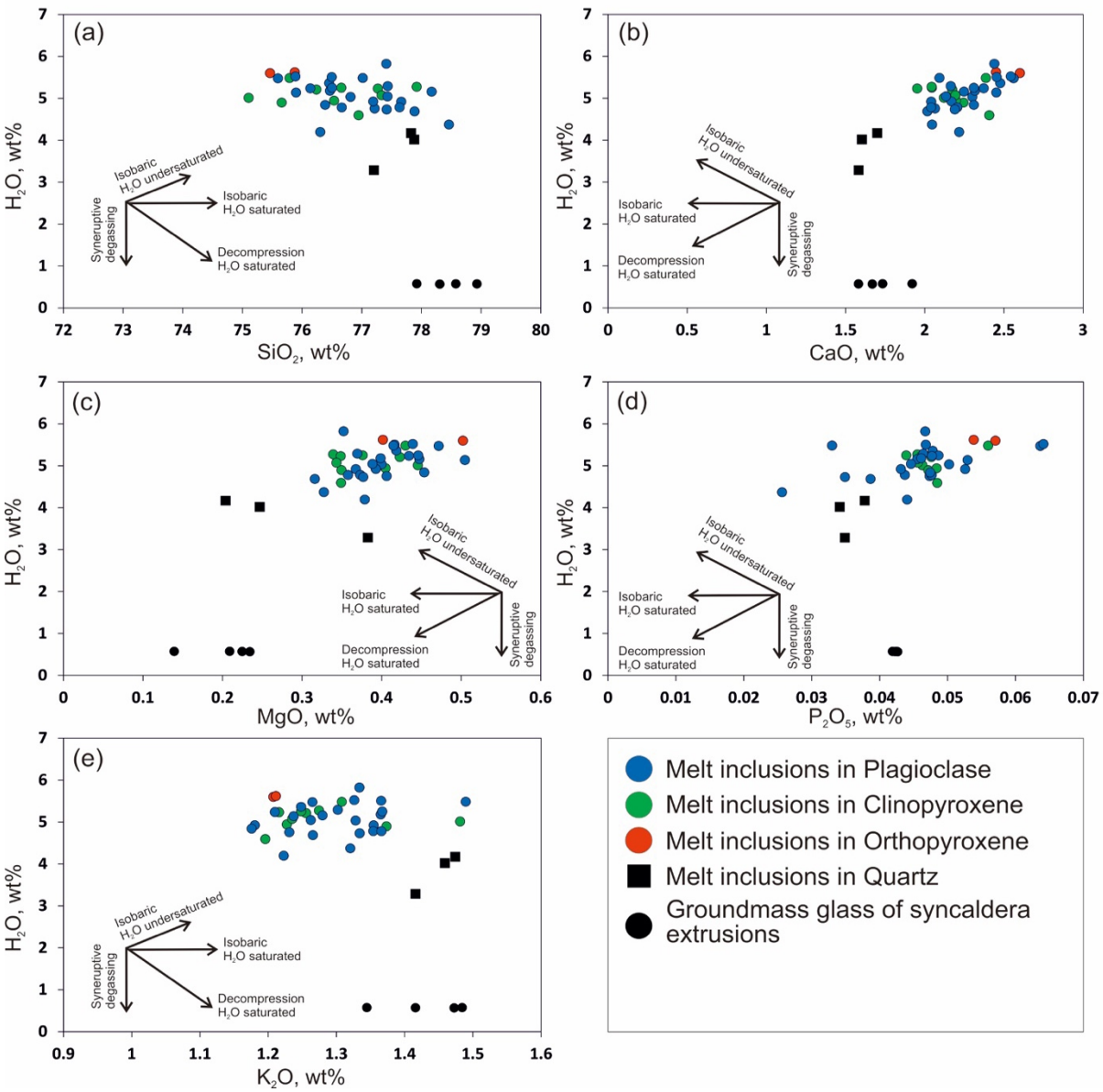

Fig. 2.9. Variation in dissolved H_2O versus (a) SiO_2, (b) CaO, (c) MgO, (d) P_2O_5, and K_2O contents for the MIs and syncaldera extrusion dome rock groundmass glass. Arrows show the main trends expected from different crystallization mechanisms (Blundy & Cashman, 2005).

The H_2O contents of quartz-hosted MIs and GM glass in syncaldera dome rocks exhibit lower values compared to those found in MIs from plagioclase and pyroxenes. This observation is consistent with the knowledge that quartz typically crystallizes during the later stages of pre-eruptive magma evolution, and it tends to be more abundant in syneruptive lava domes while being less prevalent in the pumices. As a result, the compositions of quartz-hosted MIs can serve as a representation of the latest stage of pre-eruptive melts, whereas the GM glass in dome rocks can be indicative of syneruptive melts. Figure 2.9 demonstrates that the quartz-hosted MIs generally align with the low-H_2O end of the compositional trend observed in MIs across

all minerals. This evidence of late-stage degassing may also provide an explanation for the transition from an explosive to an effusive style of eruption (Popa et al., 2021).

Contents of H_2O in the GM glass of the syncaldera extrusive domes are markedly lower than those in quartz-hosted MIs. These lower H_2O at similar SiO_2 contents suggest syneruptive degassing that was not accompanied by substantial crystallization. In this case, the MIs in quartz record the increase in the decompression rate that precedes the syneruptive degassing indicated by the depletion of H_2O in the GM glass of syncaldera extrusions.

2.8.3. Pressure, temperature, and redox properties of the pre-eruptive magma

The observed mineral assemblages, formed either due to amphibole breakdown or direct crystallization from melts, provide valuable insights into estimating the parameters (pressure, temperature, and oxygen fugacity) of the stored magma before the 40 ka Mendeleev caldera eruption.

To determine the temperature and oxygen fugacity, we used thermo-oxybarometers proposed by (Ghiorso & Evans, 2008) and (Andersen & Lindsley, 1985) for Fe–Ti oxide pairs. We also employed clinopyroxene–orthopyroxene and plagioclase–melt pairs to estimate temperature (Putirka, 2008). Mineral–liquid thermometry utilized only MIs with known H_2O contents, assessed using SIMS, and a pressure of 1 kilobar was assumed for temperature calculations.

Fe–Ti oxide equilibrium tests confirmed that the applied thermo-oxybarometers produced comparable results for both contacting or intergrowing pairs of Ti-magnetite and ilmenite, as well as inclusions of these minerals closely spaced within the same growth zone of pyroxene and plagioclase. The temperatures calculated using the models of (Ghiorso & Evans, 2008) and (Andersen & Lindsley, 1985) indicated equilibrium at 850–885 °C and an fO_2 of 0.85–1.05 log units above the nickel–nickel oxide (NNO) buffer, and at 860–873 °C and an fO_2 of 1.05–1.23 log units above the NNO buffer, respectively.

The two-pyroxene thermometer of (Putirka, 2008) was applied to contacting pairs of pyroxene crystals. Calculations yielded a temperature range of 830–890 °C (equation 36 of Putirka, 2008, with ±45 °C uncertainty). *Kd* (Fe–Mg) varies within 0.61–0.75, which falls within the confidence interval for subsolidus systems (Putirka, 2008).

Plagioclase–liquid mineral thermometry (Putirka, 2008) was based on the MI compositions and corresponding host plagioclase compositions and yielded equilibrium temperatures ranging from 835 to 879 °C (equation 24a of (Putirka, 2008), with ±36 °C

uncertainty). Despite wide variations in plagioclase compositions, we did not observe obvious dependence between temperature and the location of MIs in the specific growth zone of the host plagioclase.

The equilibrium temperatures calculated using the different approaches show that the formation of reaction-derived minerals and crystallization in the magma reservoir occurred within a temperature range of 830–890 °C.

Despite the presence of MIs in ortho- and clinopyroxenes, we did not apply pyroxene-liquid thermometers in this paper. Unlike the other thermometers, clinopyroxene-liquid and orthopyroxene-liquid ones do not pass the test of equilibrium between pyroxene and liquid (Rhodes et al., 1979). This might be additional evidence for the reactional nature of pyroxenes which is discussed above.

The pressue in the magma reservoir can be determined using solubility models for volatile species. The coupled solubility of H_2O and CO_2, which are two major volatile components, is typically used to estimate saturation pressure. In this study, we used the VolatileCalc 2.0 model (Newman & Lowenstern, 2002) of H_2O-CO_2 coupled solubility in rhyolitic melts. All pressures were calculated at a nominal temperature of 850 °C as a realistic average temperature estimated as described above. Saturation pressure was estimated at 116–195 MPa for the MIs in plagioclase and pyroxenes, 77–116 MPa for the MIs in quartz, and 2.9 MPa for the H_2O-poor GM glass of syncaldera extrusive domes. Pressure estimations for the MIs should be considered as a minimum possible pressure for the 40 ka Mendeleev stored magma because of the presence of other volatiles (CO_2, S, F, and Cl) and possible fluid saturation. Fluid saturation in the magmatic reservoir is confirmed by H_2O-rich fluid inclusions found in plagioclase cores and clinopyroxene. Such fluid inclusions were trapped simultaneously with MIs and serve as an argument for fluid saturation and magma degassing.

The identified mutuality between H_2O and major elements (see the section above 2.8.2 entitled “Crystallization and magma degassing”) is in good agreement with estimations of pressure in the 40 ka Mendeleev caldera magma reservoir. Pressure variations coincide with a gradual decrease in H_2O contents, confirming slight decompression and degassing. Here, we estimate the depth of the magmatic chamber based on the average crustal density of Kunashir Island of 2600 kg/m^3 (Nakanishi et al., 2009). Pressure estimations for the MIs in quartz (77–116 MPa) correspond to a depth range of 3.0–4.5 km, whereas those for plagioclase- and pyroxene-hosted MIs suggest depths at level 4.5–7.6 km. As we show below in the section 2.8.4

entitled “Amphibole relics as evidence of magma genesis”, amphibole breakdown probably occurred at depths of up to 12.3 km. All of these depth estimations and variations in volatile and major-element contents in MIs can be explained either by the ascent of partial melts from their source to the reservoir at a depth of 4.5–7.6 km and simultaneous segregation of eruptible magma at a depth of 3–4.5 km, or by partial rupture of the magma chamber without a major eruption. Such a model suggests that the caldera eruption was related to a magmatic plumbing system that extended to the entire thickness of the upper crust. Moreover, assuming that quartz phenocrysts crystallized from the melts in the main magma reservoir immediately before the caldera-forming eruption and thus recorded more extensive decompression, we interpret that the difference between pressure estimations for MIs in quartz and the GM glass of syncaldera extrusion dome rocks can be regarded as overpressurization specific to water-saturated magma in the sealed magma reservoir (Kotov et al., 2023).

Therefore, the depth of the stored eruptible magma for the 40 ka Mendeleev caldera-forming event can be roughly estimated as 3.0–4.5 km below surface level. The power of this eruption event was probably controlled by the inferred overpressurization. The marked reduction in water content of the magma before syncaldera dome extrusion implies more extensive decompression of the stored magma, which could have been caused by massive destruction of the reservoir roof, leading to a major eruption event.

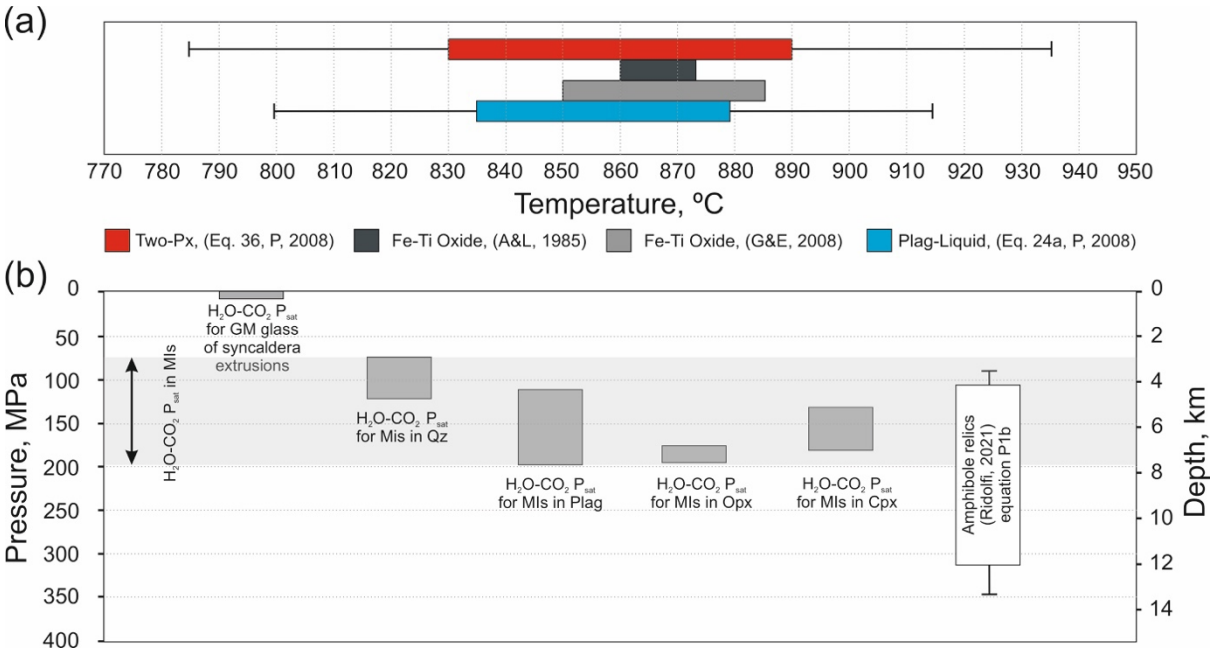

Fig. 2.10. (a) Ranges of temperatures estimated using the two-pyroxene thermometer of (Putirka, 2008), Fe–Ti oxides using the models of (Ghiorso & Evans, 2008) and (Andersen & Lindsley, 1985), and the plagioclase–liquid thermometer of (Putirka, 2008). (b) Ranges of H_2O-CO_2 saturation pressure for melts, calculated by VolatileCalc 2.0 (Newman & Lowenstern, 2002) and pressure estimation for

amphibole relics using (Ridolfi, 2021). Depth calculated using crustal density of Kunashir Island of 2600 kg/m^3 (Nakanishi et al., 2009)

Estimated H_2O contents and P–T–fO_2 ranges for the 40 ka Mendeleev caldera stored magma prior to eruption are comparable to those determined for the 20 ka Vetrovoy Isthmus eruption (Smirnov et al., 2019), and both pressure estimates are close to the preferred pressure for eruptible stored magma of 200 ± 50 MPa derived from thermomechanical modeling of stored magma dynamics by (Huber et al., 2019). Those estimations of pre-eruption H_2O contents in the 40 ka Mendeleev caldera magma are comparable to the estimations of (Popa et al., 2021) of H_2O contents promoting explosive eruptions corresponding to the crystallinity of Mendeleev pumice. The similarity of the Mendeleev and Vetrovoy Isthmus calderas suggests that the P–T conditions of stored magma for massive dacitic magma eruptions in the southern Kuril Island Arc may be regionally consistent, indicating a common regional process resulting in series of powerful explosions associated with the formation of large calderas and thick pyroclastic flow deposits.

2.8.4. Amphibole relics as evidence of magma genesis

Interpretations of the origin of island-arc dacitic magmas usually balance between two contrasting scenarios: fractional crystallization of primitive or contaminated deep mafic magma, or partial melting of arc crust. Fractional crystallization of primitive mantle magmas should produce andesitic melts with a high silica content (e.g., Gill, 1981; Grove et al., 2003). The appearance of more felsic magmas requires particular conditions, i.e., high crystallinity and low H_2O contents of the initial magma charge (Whitaker et al., 2008; Erdmann & Koepke, 2016). Primitive magmas are usually H_2O rich, whereas the high degree of their crystallinity (>90%) should hinder separation of viscous felsic liquids from the fractionating magma batch (Vigneresse et al., 1996). The assimilation of aluminosilicate sedimentary or metamorphic rocks or mixing of primitive mantle magma with silica-rich crustal melts may lead to an increase in the initial SiO_2 content of the contaminated magma charge and cause higher SiO_2 contents at lower degrees of crystallinity. Nevertheless, the felsic compositions of the earliest MIs in pyroxenes can be considered as sufficient evidence against crystallization from primitive or contaminated mafic or andesitic melts.

Although pyroxenes are abundant among the Mendeleev pumice phenocrysts, the observed compositional variations of the melt are controlled mostly by the crystallization of plagioclase, as demonstrated above. Augite and enstatite are most likely the products of

amphibole breakdown, which is common in anatectic melt generation within a pressure range of 0.1–1.0 GPa (Beard & Lofgren, 1991; Rapp & Watson, 1995; Vielzeuf & Schmidt, 2001).

Amphibole can be an indicator of magmatic crystallization conditions, as its occurrence in the mineral assemblage is strictly controlled by T–P–XH_2O. The mineral assemblages of the 40 ka Mendeleev pumice contain amphibole only as relics in pyroxene and plagioclase, in some cases together with trapped rhyolitic melt. The composition of this melt (Figs 2.7 and 2.11) is similar to the composition of the ordinary MIs in all other minerals and the GM glass. The corroded and intricate morphologies of amphibole relics in augite and plagioclase (Fig. 4e) clearly indicate that the amphibole was either partially melted prior to entrapment or replaced by the host mineral. Contacts between amphibole relics and attached glass are sharp and lack reaction rims, as have also been shown, for example, in the case of Mount St. Helens (Rutherford & Hill, 1993), where amphibole has reaction rims only at the contact with melt. Amphibole relics evidencing its disequilibrium during pre-eruptive magma storage have been commonly observed in dacitic pumices formed by large explosive events in the NE Japan–SW Kuril region (e.g., Miyagi et al., 2012; Smirnov et al., 2019).

To evaluate the disequilibrium between coexisting rhyolitic melt and amphibole, we performed estimations of the major-element melt chemistry that should be in equilibrium with the amphibole relics, referred to as amphibole equilibrium melt (AEM). This was accomplished using the model proposed by (Zhang et al., 2017) and utilizing the spreadsheet provided by (Humphreys et al., 2019) (Fig. 2.11a–d). Subsequently, we compared the calculated compositions of AEM with the compositions of melt inclusions (MIs) attached to amphibole relics (Fig. 4e).

The results revealed that the predicted AEM compositions varied over a wider range compared to those of MIs attached to amphibole relics. The discrepancy between the predicted AEM and the attached MI compositions was more pronounced for orthopyroxene- and certain clinopyroxene-hosted amphibole relics but smaller for plagioclase- and most clinopyroxene-hosted relics. The contents of MgO and Al_2O_3 displayed the smallest deviations for AEM of plagioclase- and most clinopyroxene-hosted amphibole relics. The deviation in TiO_2 content was smaller for the AEM of plagioclase-hosted relics. Notably, the predicted AEMs were found to be depleted in FeO and significantly enriched in K_2O relative to MIs (Kotov et al., 2023)

The observed differences between the predicted AEMs and the actual melt compositions provide clear evidence that amphibole was not in equilibrium with the rhyolitic melts of the 40

ka Mendeleev caldera's pre-eruptive magma. This finding highlights the presence of disequilibrium conditions between the coexisting rhyolitic melt and amphibole relics during the magma's evolution.

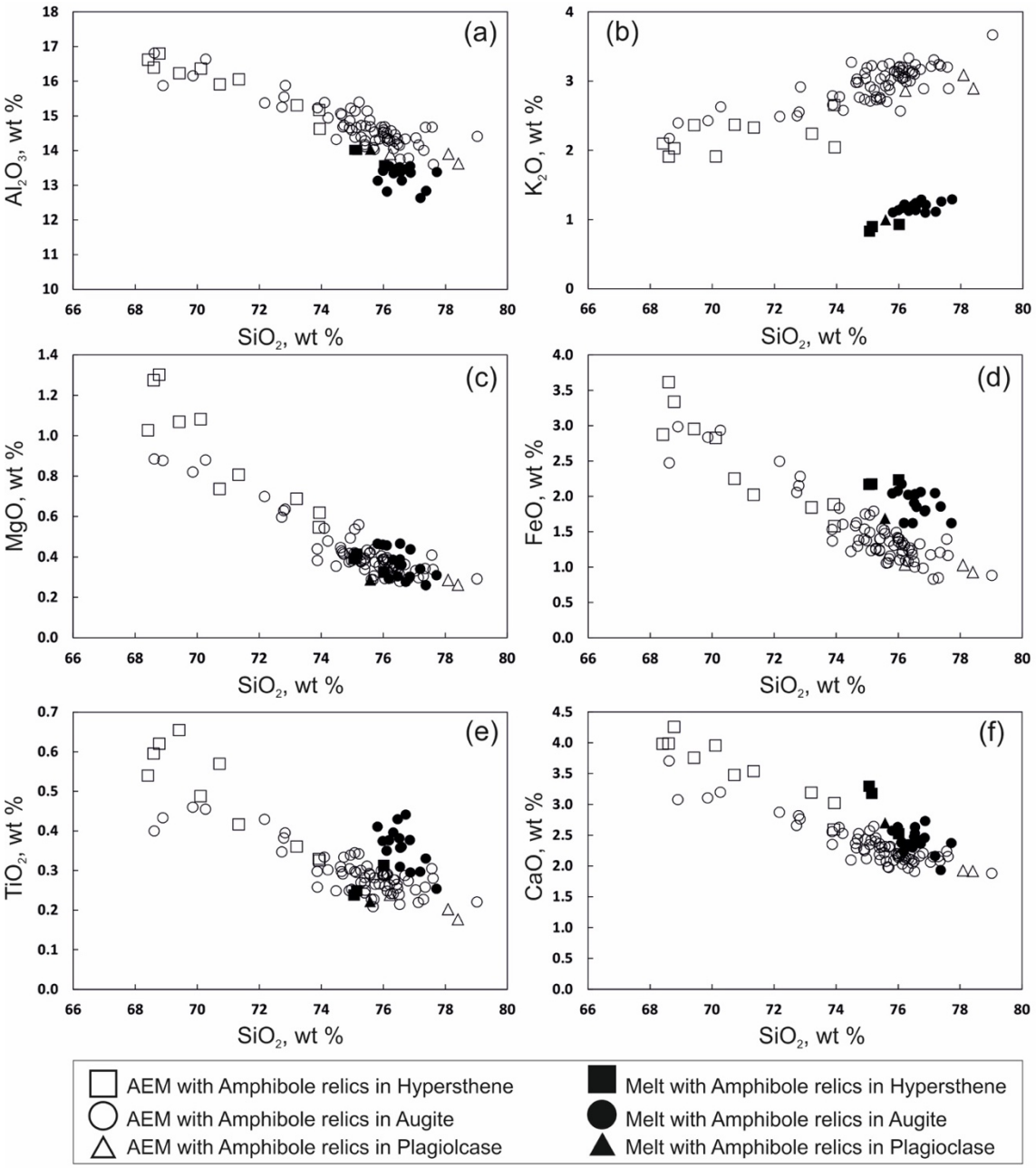

Fig. 2.11. Variations in major-element contents of Mendeleev MIs coexisting with amphibole relics (filled symbols) and amphibole equilibrium melt (AEM; open symbols). AEM was calculated following the model of (Zhang et al., 2017) and updated by (Humphreys et al., 2019). The following equilibria were used: [1] for SiO2, [5] for TiO2, [7] for FeO, [8] for MgO, [9] for CaO, [10] for K2O, and [11] for Al2O3.

The presence of amphibole only as an inclusion, as well as its location only in the plagioclase cores indicates that it was the earliest-formed mineral in the 40 ka Mendeleev pumice mineral assemblage. But we suggest that amphibole should not be interpreted as having

formed by crystallization of the parental magma (Kotov et al., 2023). This mineral was probably derived from pre-existing rock subjected to partial melting during the generation of dacitic magma. In that case, it records the parameters of its last equilibration, which was likely related to a magma-generation event.

It is important to note that thermometers and barometers based on amphibole–other mineral equilibria (e.g., Holland & Blundy, 1994; Molina et al., 2015) or on the amphibole–melt equilibrium (Putirka, 2016) are not applicable here, as the studied amphibole relics might not be in equilibrium with other minerals in the assemblage. Therefore, only the amphibole thermobarometry proposed by (Ridolfi & Renzulli, 2012) and revised by (Ridolfi, 2021) was used in this study for estimating the P–T conditions of the last amphibole equilibrium. Calculations suggest that this equilibrium occurred under 107–314 ± 38 Mpa (Eq. P1b, Ridolfi, 2021) and 807–932 ± 22 °C. (Fig. 2.12).

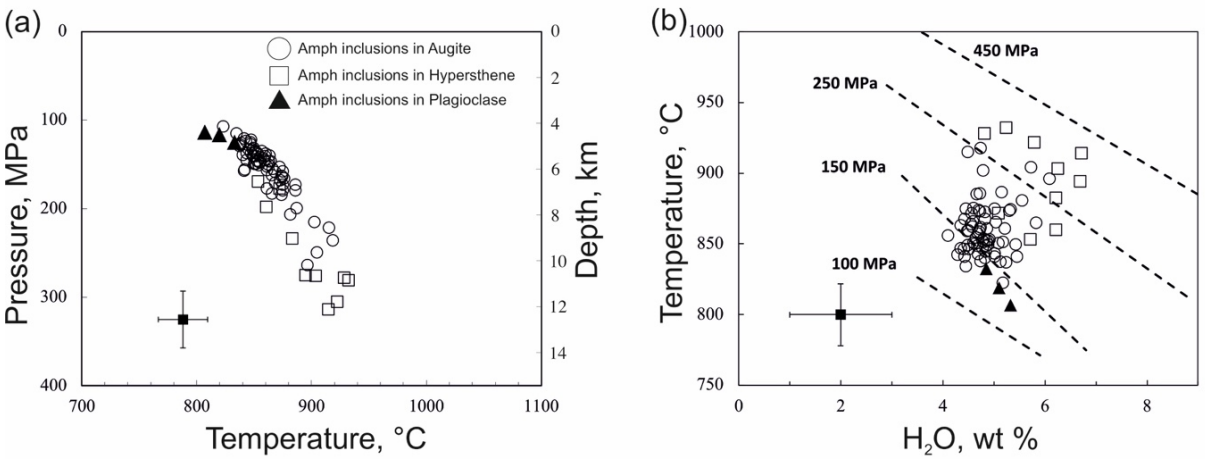

Fig. 2.12. Results of amphibole thermobarometry using the method of (Ridolfi, 2021). Cross-bars present the maximum error (from Ridolfi, 2021). Depth calculated using crustal density of Kunashir Island of 2600 kg/m3 (Nakanishi et al., 2009). The dashed lines in (b) show isobars from (Ridolfi, 2021). The legend is the same as for Fig. 5.

The estimates of temperature, pressure, and H_2O content of the amphiboles presented above cannot be directly used to determine the generation conditions of Mendeleev caldera magmas due to their melted and anhedral nature. However, these estimations are likely close to the conditions for dacite generation. If we consider the P–T–XH_2O parameters from (Ridolfi, 2021) corresponding to the formation of amphibole, changing one of these parameters may lead to the removal of amphibole from its stability field, as demonstrated for Mount St. Helens by (Riker et al., 2015). The conditions of the last amphibole equilibrium, as determined above, are reasonably comparable to the estimated P–T–XH_2O parameters for the 40 ka Mendeleev

caldera's stored pre-eruptive magma. The orthopyroxene-hosted well-shaped amphiboles provide systematically higher temperatures and pressures, while the plagioclase-hosted amphibole relics yield the lowest estimations (Fig. 2.12a). These observations suggest that the melting that formed the magma likely occurred somewhat deeper than the magma storage depth, at temperatures slightly above those recorded by phenocrystic minerals (see section 2.8.3 entitled "Pressure, temperature, and redox properties of the pre-eruptive magma" and Fig. 2.10b). This, in turn, implies short paths of ascent and good preservation of residual minerals in the ascending magma. The most probable scenario for amphibole instability is an increase in temperature, leading to the melting of amphibole-bearing rocks due to intense heating by deep-fluxed magmas. This observation is consistent with the fact that the high-Al amphiboles from the Mendeleev pumice are better preserved and more abundant compared to the scarce, small, anhedral low-Al amphiboles. Therefore, amphibole barometry supports the conclusions that amphibole-bearing rocks served as a melting protolith, and the melting occurred in the upper part of the crust of Kunashir Island, not far from the location of the main magma reservoir.

Similar scenarios to the one presented above were suggested by (Smirnov et al., 2017; 2019) for the pre-eruptive magmatic history of the 20 ka Vetrovoy Isthmus eruption on neighboring Iturup Island. The model proposed by these authors suggests that the early mineral assemblage ("gabbro-noritic") of plagioclase + augite + hypersthene + Fe–Ti oxides + sulfides + apatite originated during the partial melting of metamorphic amphibole-bearing rocks. This process involved a peritectic amphibole breakdown reaction accompanied by the generation of rhyolitic melt. The later mineral assemblage of plagioclase + quartz crystallized directly from this partial melt.

Experimental evidence has shown that amphibole breakdown during partial melting in the Earth's crust plays a vital role in the generation of siliceous magma (Beard & Lofgren, 1991; Rapp & Watson, 1995; Kawamoto, 1996). The partial melting of crustal rocks has been demonstrated to produce dacitic magmas in the Izu–Bonin arc (Tamura & Tatsumi, 2002; Shukuno et al., 2006), the southern Kuril Islands (Smirnov et al., 2019), and South Sister volcano (Cascade Range, Oregon, U.S.; Waters et al., 2021). Additionally, dehydration of amphibole is an efficient mechanism for producing substantial amounts of aqueous fluid, which is crucial for the genesis of arc silicic magma.

To confirm that the Mendeleev dacitic pumices are not a product of fractionation, we compared the melt compositions and estimated magmatic temperatures with major-element contents estimated from studies of experimental glasses and experimental temperatures of

partial melting (Holloway & Burnham, 1972; Beard & Lofgren, 1991; Kawamoto, 1996; Shukuno et al., 2006) and crystallization experiments (Sisson & Grove, 1993; Grove et al., 2003; Nandedkar et al., 2014; Ulmer et al., 2018; Marxer et al., 2022) (Fig. 2.13a–h). We use melt compositions instead of pumice whole-rock compositions because if some minerals have a reactional nature, then the whole-rock composition may not correspond to that of the original melt.

Compositions comparable to the studied MIs and GM glass were generally obtained from partial melting experiments. For example, melts obtained by Beard & Lofgren (1991) from dehydration melting of hornblende hornfels (Sample 466, low-K amphibolite) at 100 and 300 MPa and 900–1000 °C are most consistent with the observed Mis attached to the amphibole relics and GM glass (Fig. 2.13a–h). Compositions of partial melts similar to the observed MIs were obtained by Kawamoto (1996) in melting experiments at 500 MPa, 875 °C, and 1 wt.% H_2O. However, under this pressure, amphibole should be stable in the residual assemblage, which is not consistent with the mineralogy of Mendeleev pumice.

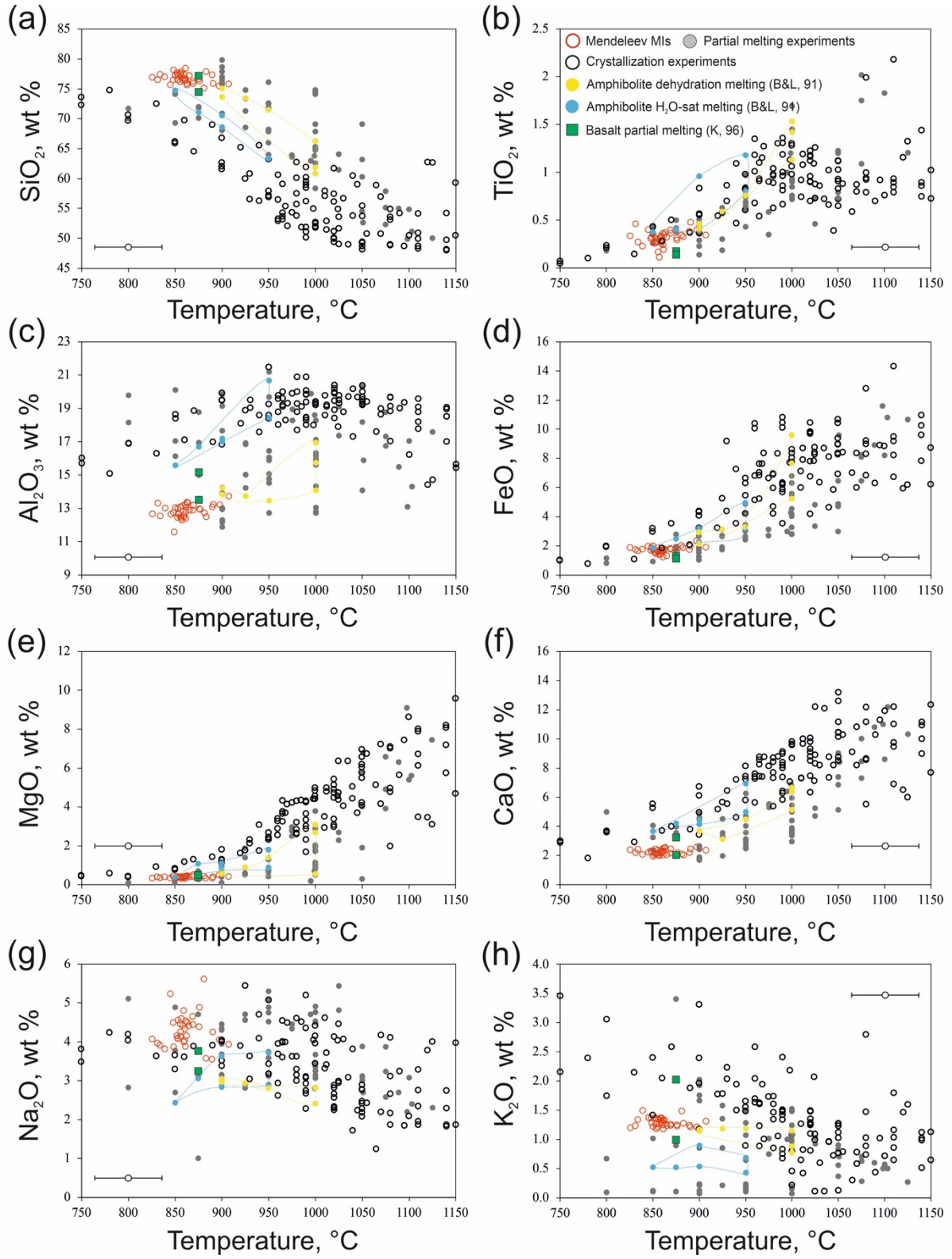

Fig. 2.13. Major-element contents from partial melting experiments (filled gray circles) conducted over a range of pressures (100–900 MPa) and H2O contents (0–5 wt%) using mafic protoliths (Holloway & Burnham, 1972; Beard & Lofgren, 1991; Kawamoto, 1996; Shukuno et al., 2006) and crystallization experiments (open black circles) conducted at variable pressures (200–1000 MPa), H_2O contents (anhydrous to 12 wt% H20), and oxygen fugacity (NNO−2 to NNO+3) (Sisson & Grove, 1993; Grove et al., 2003; Nandedkar et al., 2014; Ulmer et al., 2018; Marxer et al., 2022) using basalts. Mendeleev melts (open red circles) are shown as a function of their temperatures estimated from mineral–liquid thermometry. Error bars indicate uncertainty (±36◦C) for plagioclase-liquid thermometry of (Putirka,

2008, equation 24a). Yellow and blue circles are highlighted results of dehydration melting and water-saturated melting experiments on low-K amphibolite (sample 466) under 1 and 3 kbar from (Beard & Lofgren, 1991). Green squares are results of two partial melting experiments on high-Al basalt under 5 kbar, 1–2 wt% H_2O and 875◦C from (Kawamoto, 1996) (see text for details).

In summary, the compositions of MIs and GM glass in rocks produced by the 40 ka Mendeleev caldera eruption confirm that they were generated during the course of partial melting of amphibole-bearing pre-existing rocks. Given their high viscosity, these melts were unable to separate from the residual minerals that formed during amphibole breakdown. Residual minerals [plagioclase (probably lower than An mol% = 82) + augite (Mg# = 72–77) + enstatite (Mg# = 68–74)] and silica-rich partial melts [(74–77 wt.% SiO_2(anh) and 4–6 wt.% H_2O] constituted the primary magma, which had dacitic bulk composition.

2.8.5. Remarks on magma origin and storage conditions for the 40 ka Mendeleev caldera eruption

The pressures estimated for the last amphibole equilibrium suggest that the amphibole breakdown reaction likely occurred in the upper crust of Kunashir Island, at depths ranging from 4.2 to 12.3 km, assuming an average crustal density of 2600 kg/m^3 (Nakanishi et al., 2009). These data align with geophysical estimates indicating an upper-crustal thickness of up to 10 km under Mendeleev volcano (Zlobin et al., 1997).

It is widely accepted that partial melting occurs within deep-crustal hot zones (DCHZs) due to the thermal influence of mantle-derived magmas stalling at lower-crustal depths (Annen et al., 2006). Magmas accumulating in the upper crust are considered ascending derivatives of DCHZ magmas, exemplified by the dacites of South Sister volcano (Blatter et al., 2017; Waters et al., 2021). These dacitic melts from South Sister were formed through partial melting at relatively high temperatures (≈1000 ± 50 °C), high pressures (>400 MPa), and low water contents (<3.3 wt.%). These P–T conditions are higher than those determined for the generation of the 40 ka Mendeleev caldera magma and lie well within the amphibole stability field, implying the presence of amphibole in the residual mineral assemblage. However, the low water contents observed only in the late stages of magmatic evolution in the Mendeleev caldera pre-eruption history do not fit this scenario for explaining the origin of the 40 ka Mendeleev caldera magma. An alternative scenario proposes the direct generation of dacitic magma within the middle-upper crust, not far from the main magma storage site. The estimated lower temperatures (<900 °C) and pressures (<300 MPa) support this alternative scenario as a better explanation for the pre-eruptive stored magma of the 40 ka Mendeleev caldera. A similar scenario has been proposed for the origin of the 20 ka Vetrovoy Isthmus dacitic magma on

Iturup Island (Smirnov et al., 2019). These findings suggest that partial melting within the upper crust is an effective mechanism for the formation of relatively large reservoirs of felsic magmas in island-arc settings, indicating that the melting of amphibole-containing rocks likely occurs throughout almost the entire crust thickness.

No amphibole-bearing xenoliths in rocks of Kunashir Island have been reported in this or earlier studies, except for the melted amphibole relics discussed in this paper. The presence of amphibole relics in pyroxenes and plagioclase indicates the involvement of some precursor amphibole-bearing assemblages, although their precise nature remains uncertain. Arc magmas are known to often contain plutonic xenoliths, including amphibole-bearing rocks (e.g., hornblende gabbro) and amphibole-rich rocks (e.g., hornblendites) (e.g., Wilshire et al., 1988; Stamper et al., 2014; Melekhova et al., 2019). Moreover, these rocks can be equilibrated and accumulated throughout almost the entire arc crust (e.g., Melekhova et al., 2019). Thus, dacites may form at a peritectic distributary reaction boundary over a wide range of depths in the arc crust (Beard & Lofgren, 1991; Rapp & Watson, 1995; Petford & Atherton, 1996; Petford & Gallagher, 2001; Izbekov et al., 2004; Blatter et al., 2017; Waters et al., 2021). This result implies that long-lived primitive magma or recharge of volatiles are necessary to induce persistent production of dacite magma in the upper crustal regions, while amphibole-bearing cumulates in the crust may provide a fertile source for melts and fluids.

Regarding the heat source for partial melting under upper-crustal conditions at Mendeleev volcano, this represents an important problem requiring further discussion. Taking into account the higher degrees of melting of Pleistocene mafic magmas of Kunashir Island, (Martynov & Martynov, 2017) concluded that their generation corresponded to a period of local or regional extension accompanied by increasing heat flow in the supra-subduction mantle. This process was accompanied by abundant subaerial eruptions of basaltic fissure volcanoes. Extensional conditions changed to compressional during the Holocene (Martynov et al., 2015; Martynov & Martynov, 2017). During this period, mantle-derived magmas were unable to reach the surface and most likely formed intrusions in the upper crust. The heat from these intrusions and their possible recharging, if available for a sufficiently long period, could have provided enough heat for partial melting of the upper-crustal rocks (Huppert & Sparks, 1988; Petford & Gallagher, 2001; Annen & Sparks, 2002). Thus, I propose that Pleistocene extension and consequent local uplift of the asthenospheric mantle led to massive generation of mafic magmas. During the Late Pleistocene, these magmas intruded the island crust but did not erupt due to the transition from tectonic extension to compression. The accumulated magmas in the

upper crust supplied sufficient heat for the intensive generation and accumulation of felsic magmas through the partial melting of crustal rocks.

In addition, I compare Vp profiles for Kunashir Island and other Islands. Geophysical observations in Kunashir Island suggest that thickness of the upper crust below Mendeleev takes 7-11 km range, while lower from 7-11 to 23 km (Zlobin et al., 1997). Vp on the seismic discontinuity between upper and lower crust is 7.1-7.3 km/s. These Vp values may correspond to such rocks as gabbro and hornblendites with density higher than 3.0 g/cm^3. Compare to other arcs this is very shallow conditions for such high Vp value (e.g., Kodaira et al., 2007; Takahashi et al., 2007; Kopp et al., 2011; Melekhova et al., 2019, and many others) (Fig. 2.14). This may be additional indirect evidence that there are dense mafic-ultramafic rocks on Kunashir in very shallow conditions, which we do not see, but they serve as a protolith for partial melts.

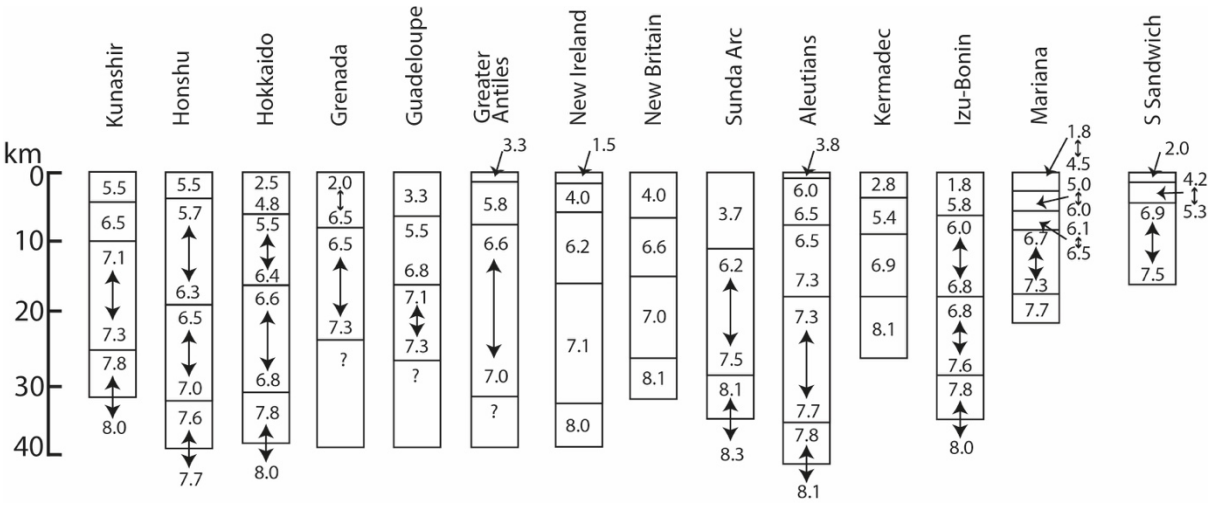

Figure 2.14. Comparison of crustal structure of a selection of island arc based on geophysical observations (updated and modified from Melekhova et al., 2019). The range in Vp (km/s) within individual crustal layers is shown by the double-ended arrows. Seismic discontinuities are shown by solid horizontal lines. A question (?) indicates a poorly resolved Moho. References for the arcs are provided by Boynton et al., 1979; Zlobin et al., 1997; Iwasaki et al., 2001; Iwasaki et al., 2004; Christeson et al., 2008; Kopp et al., 2011; Shillington et al., 2004; Kodaira et al., 2007; Takahashi et al., 2007.

2.9. Conclusions

The eruption of the Mendeleev caldera, which occurred around 40,000 years ago on Kunashir Island in the southern Kurils, involved a low-K dacitic magma, a characteristic trait of southern Kuril calderas. Pre-eruptive magma crystallization temperatures varied between 830 and 890 °C, with the magma evolving in shallow upper-crustal conditions at pressures ranging from 77 to 195 MPa and at an oxygen fugacity of 0.85-1.05 above the NNO buffer.

The main volatiles dissolved in the magma of the 40 ka Mendeleev caldera eruption were water and chlorine, with minor amounts of CO_2 and sulfur species. Pre-eruptive melts

were water-saturated, and their H_2O contents ranged from 4.2 to 5.8 wt.% H_2O (mean = 5.1 wt.% H_2O), which aligns with magmatic water contents found in other calderas of the southern Kurils and Hokkaido (Miyagi et al., 2012; Kotov et al., 2021). During the period of pre-eruptive crystallization of plagioclase and pyroxenes, H2O contents in the magmatic melts slightly decreased, indicating minor magma degassing. As quartz joined the other crystallizing minerals during magma ascent, the rate of degassing increased, leading to H_2O contents in the melt decreasing to 3.3-4.2 wt.%. The major eruption resulted in significant magma degassing, and the latest portions of magma extruded as domes were almost devoid of water. The depletion of H_2O in the groundmass of the syncaldera extrusive dome rocks, without a notable change in SiO_2 content, suggests that syneruptive degassing did not involve substantial crystallization.

A comprehensive examination of pumice mineralogy revealed that the early 'gabbro-noritic' assemblage, comprising plagioclase, augite, hypersthene, and Fe-Ti oxides, crystallized due to Mg-hornblende dehydration breakdown. Considering the rhyolitic compositions of the primary melt inclusions in these minerals, it is likely that their occurrence is linked to dehydration partial melting accompanying magma generation. The absence of mineral zoning and melt-inclusion compositions indicating precursor mafic or intermediate parental melts suggests that partial melting was the primary mechanism for felsic magma generation during the 40 ka Mendeleev caldera eruption. This magma comprised rhyolitic melt mixed with mafic products from the amphibole breakdown reaction, resulting in a dacitic magma composition. In the final stages of magmatic evolution, minor amounts of plagioclase and quartz crystallized directly from the residual rhyolitic melt, as confirmed by the evolutionary trends of the melt inclusion compositions.

The data indicate that the magma was generated at depths ranging from 107 to 314 MPa (~4.2 to 12.3 km), likely through the partial melting of amphibole-bearing crustal rocks. Crystallization of the early minerals occurred at these depths, while the later quartz-plagioclase assemblage crystallized as a consequence of magma ascent to depths of 3-4.5 km. This suggests that the magmatic system of Mendeleev volcano extended from the magma source to the caldera eruption reservoir, potentially occupying most of the upper crust of Kunashir Island, in agreement with geophysical observations.

The partial melting of previously erupted rocks can be triggered by repeated intrusions of hot mafic magma into the upper crust, as proposed in the model of (Petford & Gallagher, 2001). This process aligns with the findings of (Martynov & Martynov, 2017), who inferred

regional stretching of Kunashir Island during the Pleistocene, leading to substantial thermal inflow into the island-arc crust from multiple intrusions of mantle-derived mafic magmas.

The data and conclusions regarding the 40 ka Mendeleev caldera eruption magma are consistent with previously reported results for the 20 ka Vetrovoy Isthmus caldera eruption on neighboring Iturup Island (Smirnov et al., 2019). Similar findings of amphibole breakdown relics together with rhyolitic melt inclusions in dacitic pumices from neighboring Hokkaido Island (Miyagi et al., 2012) provide strong evidence for the generation of silicic magmas under upper-crustal conditions through the partial melting of crustal rocks. This mechanism is likely applicable to other magmatic systems in young island arcs.

Chapter 3. Evolution of the crustal magma plumbing system beneath Onikobe and Naruko calderas, NE Honshu

3.1. Introduction

The study of multistage or repeated caldera eruptions belonging to the same system (in the broad sense) is interesting because it allows us to trace the changes occurring in the magmatic system over time. It is also likely that conditions may change during the accumulation of high-siliceous magmas in the sources, which, in turn, may lead to attenuation or, conversely, accumulation or remobilization of potentially hazardous magmas. In this context, calderas with several stages or phases of eruptions separated in time are extremely interesting. Many recent works have shown that multistage caldera and volcanic eruptions can be caused by reasonably rapid remobilization of magmas, which is reflected in the disequilibrium mineral zoning (e.g., Till et al., 2015; Cooper et al., 2017; Flaherty et al., 2018; Sato et al., 2022). A description of the differences in mineral composition and volatile and melt inclusions may help better understand how siliceous magmas change over time. Here I consider tow Pleistocene calderas (Naruko and Onikobe) located in NE Honshu close to each other. Both calderas belong to the same "hot finger" and related to the same magmatic system in broad sense. But their petrological features differ significantly. Thus, here I describe in details whole-rock, minerals and melt inclusions compositions for both caldera-forming deposits and suggest scenarios of magmatic evolution.

3.2. Naruko caldera-forming eruption. Yanagisawa tuffs

3.2.1 Geological settings

Naruko volcano is located in the central part of the NE Honshu region. Based on the previous works of (Sakaguchi & Yamada, 1988; Soda &Yagi, 1991), Naruko's eruptive history began with the two caldera eruptions on which this study focuses. These caldera eruptions appear to be the first manifestation of Naruko as an active volcanic center. The caldera's size is approximately 7 km in diameter and was formed by these paroxysmal eruptions. The deposit of the first caldera eruption is called the Nizaka pyroclastic flow (72 ka, 2.5 km^3); the second deposit is called the Yanagisawa pyroclastic flow (45 ka, 10 km^3). After caldera eruptions, lava flows and domes were formed in the inner part of the caldera. Three units present these lavas: Ogatake–Kurumigatake lava dome, Matsugamine lava, and Toyagamori lava. The Toyagamori lava is younger than 11830 ±555 years BP based on a ^{14}C dating (Omoto, 1993). The previous

study (Ban et al., 2005) provided a detailed petrological investigation of post-caldera lavas and mafic inclusions therein. The only historical eruption occurred in AD 837 (Murayama, 1978).

Naruko volcano is an active volcano and exhibits constant fumarolic activity. Several geophysical studies show an active magmatic system beneath the volcano (Okada et al., 2014). Using seismic tomography showed a distinct seismic low-velocity zone beneath the Naruko volcano. Their results suggested the presence of molten magma in the lower crust. Also (Okada et al., 2014) indicated some small aseismic low-V and high-Vp/Vs areas in the upper crust, which could correspond to an area with molten magma. A magnetotellurometric study (Ogawa et al., 2014) also showed the presence of regions of low conductivity beneath Naruko volcano, which reach depths up to 5 km below the surface. As well (Ogawa et al., 2014) suggested that fluids are supplied by a partial melting zone at a greater depth, and self-sealed rocks cap the top of fluid reservoir at temperatures of approximately 400°C. The seismic velocity structure also shows a molten region in the upper mantle-lower crustal region beneath Naruko volcano (Nakajima and Hasegawa, 2003), and a narrow conduit with low Vp and low Vs was detected in the upper crust. This conduit is linked to the low Vs and high Vp/Vs anomaly in the lower crust and is caused by H_2O rather than melt as it does not exhibit a high Vp/Vs value. The result of a study of the $^{3}He/^{4}He$ ratio in the volcano gases and magnetotellurometry also indicated a robust magmatic contribution to the gases and the presence of a constant flow of mantle-delivered aqueous fluid under the volcano (Asamori et al., 2010; Hernandez et al., 2011).

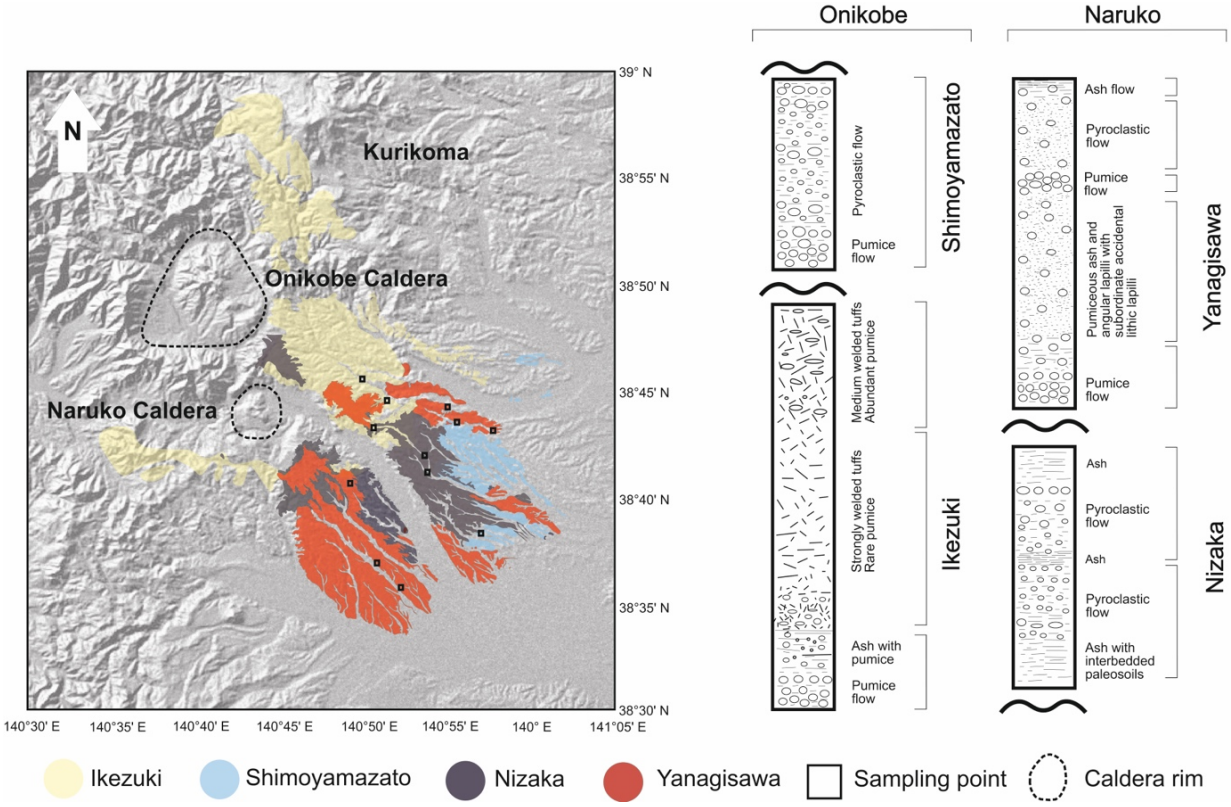

Figure 3.1. Schematic map and stratigraphy column of the Naruko and Onikobe caldera deposits based on (Tsuchiya et al., 1997; Sakaguchi and Yamada, 1988). Digital elevation model created with GeoMapApp (Ryan et al. 2009).

3.2.2. Whole-rock composition, mineralogy, and petrography of Yanagisawa caldera-forming deposit

The deposits of both eruptions consist of non-welded pyroclastic flows. Pumice from both eruptions is white, with no signs of heterogeneity. The matrix is colorless, transparent, and crystal poor. There is no significant difference in the matrix texture in Yanagisawa and Nizaka pumice. The size of pumice blocks in the Nizaka sediments is up to 1 m, while the size of pumice blocks in the Yanagisawa tuffs does not exceed 30 cm, and most pumice blocks do not exceed 5 cm. The pumice porosity in both eruptions is approximately 60 vol.%. The Yanagisawa deposit contains abundant accidental materials presented by lithic fragments of rhyolitic composition. The Nizaka deposit has much less accidental. Total crystallinities for the dacites range from 9 to 16 vol% for both eruptions. For both eruptions, quartz and plagioclase are the largest, most abundant phase and makeup between 70 and 85% of the total crystallinity of each sample. Orthopyroxene is the next most abundant mineral phase and smaller than plagioclase crystals in size (generally $\leq$ 1.5 mm). Amphibole is the fourth most common in the Yanagisawa pumice, while amphibole is absent from the Nizaka pumice as a phenocryst. Fe–Ti oxides typically have the lowest abundances.

The bulk rock major element compositions of the Yanagisawa eruptive products are reported in Supplementary Table S3.1 and shown in Fig. 3.2 a-d. Eruptive products belonged to the moderately-K rhyolites (Fig. 3.2 b).

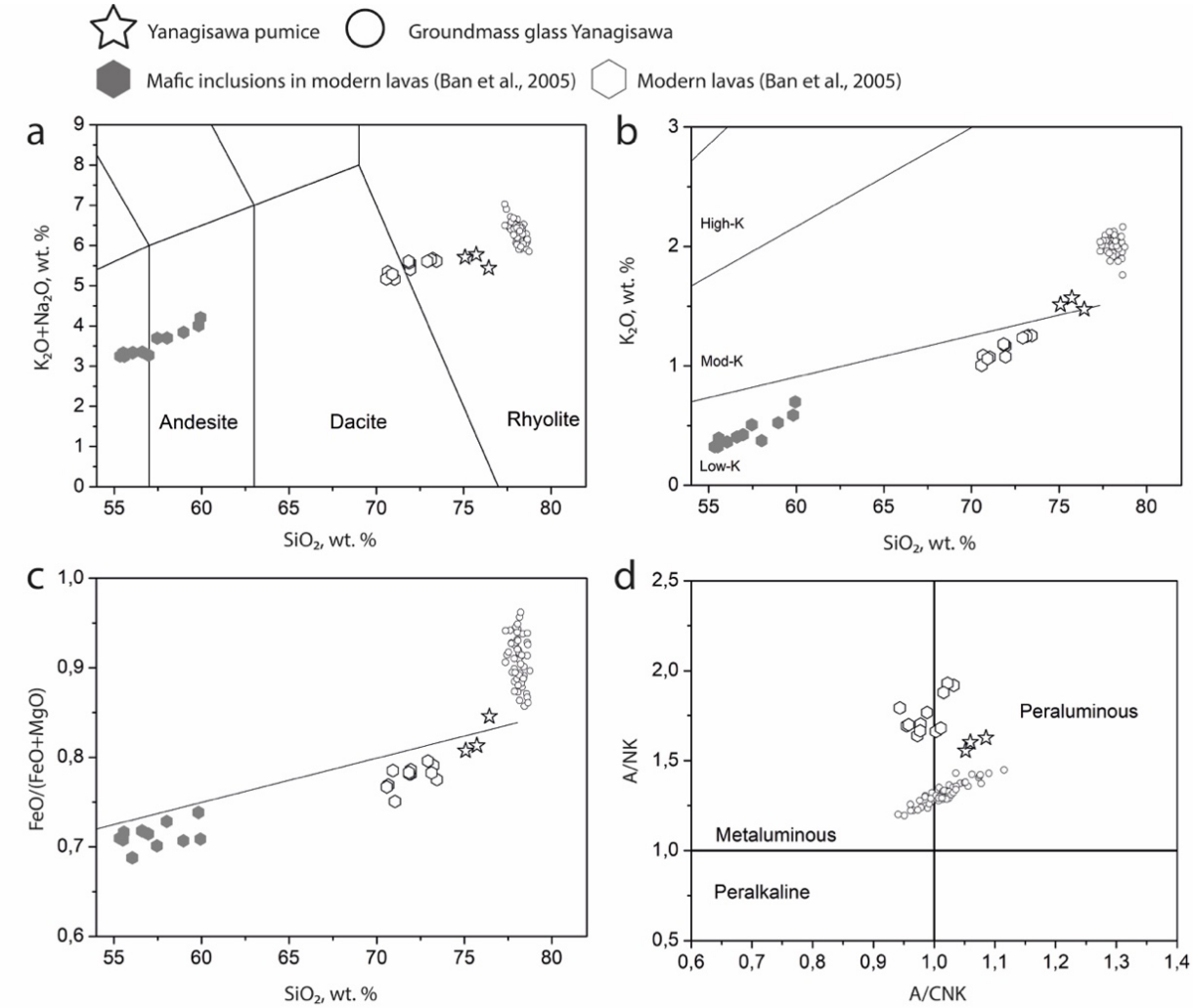

Figure 3.2. Whole-rock compositions of Naruko volcanic products. Compositions of modern lavas and mafic inclusions from (Ban et al., 2005). Classification diagrams of (a) $Na_2O + K_2O$ versus SiO_2 (Bas et al., 1986), (b) K_2O versus SiO_2 (Rickwood, 1989), (c) $FeO/(FeO + MgO)$ versus SiO_2 (Frost et al., 2001) and (d) A/NK versus A/CNK (Shand, 1943). All data are volatile-free and normalized to 100 wt.%. All Fe is FeO. $A/CNK = (Al_2O_3/101.96)/(CaO/56.08 + Na_2O/61.98 + K_2O/94.2)$; $A/NK = (Al_2O_3/101.96)/(Na_2O/61.98 + K_2O/94.2)$; $MALI = Na_2O + K_2O - CaO$.

Plagioclase

Plagioclase phenocryst is abundant in all samples. Phenocrysts are usually clear and euhedral (up 2 mm long). Plagioclase from Yanagisawa pumice often has reverse zoning. Plagioclase cores correspond to an An_{33-42} composition, and the rims at contact with the groundmass have an An_{42-48} composition (Fig. 3.3 a-c). There is often evidence of resorption at the boundary of low- and high-calcium zones (Fig. 3.3c). Only Fe-Ti oxides and rare

orthopyroxene occur as inclusions in Yanagisawa plagioclase. There are rare finds of plagioclase with patchy cores.

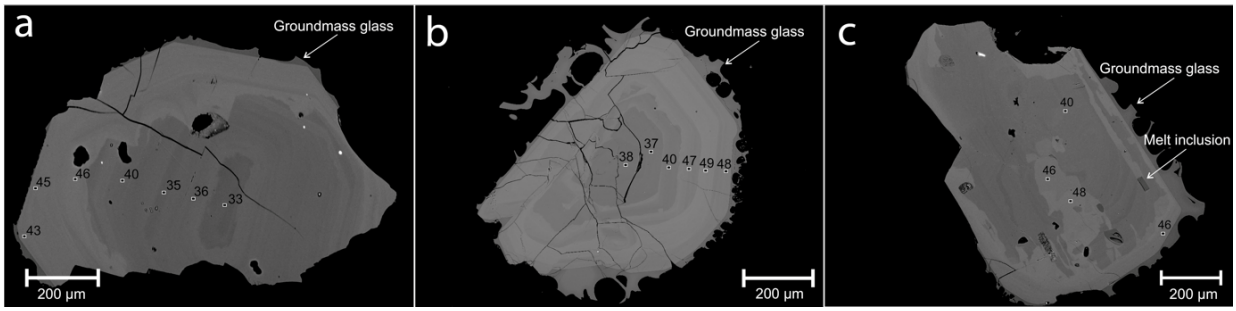

Figure 3.3. BSE images of the plagioclase phenocrysts from Yanagisawa pumice with reverse zoning and evidence of resorption on the border between Low-Ca and High-Ca zones. Numbers are shown An mol% based on EPMA analysis in black spots where is An mol%= [XCa/(XCa + XNa+XK) × 100].

Orthopyroxene. Zonation, types, and proportions

The Yanagisawa orthopyroxene is very informative in terms of the types of chemical and textural zoning presented. Hereinafter, we focus separately on the features of the textures and composition of orthopyroxene for a more extended discussion of the diffusive zoning in the next paragraph. In all samples, only orthopyroxene is present; clinopyroxene is not found. Orthopyroxene forms well-shaped crystals up to 1.5 mm in size. According to the IMA classification, orthopyroxene can be classified as enstatite in both eruptions (Morimoto et al., 1988).

A total of 192 orthopyroxene crystals from Yanagisawa pumice were studied. These proportions are considered to be representative because all crystals were handpicked and mounted randomly before zoning observation in BSE. Crystals were picked from crushed and sieved pumice into fractions of 125-250, 250-500, 500-1000, 1000-2000 microns. Summary of zonation shown in the figure 3.4. Zoned crystals of each eruption were classified according to the type of zonation observed: single zonation (normal or reverse) and multiple zonation. Each type considering as a travers from core to the rim.

In Yanagisawa pumice 72% are zoned, with a prevalence in single-zoned and particularly in reverse-zoned crystals. Only 28% of observed grains have not distinguishable zoning patterns. Among single-zoned crystals, those with reverse zoning are dominant (80%). Among multiple-zoned crystals, those in which reverse zoning from the core to the rim and streaky (sandwich) zoning at the rim prevail (Fig. 3.4. e-g). Thus, with the rarest of exceptions, in Yanagisawa orthopyroxenes, the core is always less magnesian than the rim. Mg-number is

54–60 in the cores and 61–65 in the rims, respectively. The outer High-Mg zones are relatively broad and vary within 20–160 μm. Mg-number is inversely correlated with MnO (1.1–2.0 wt %) and positively correlated with Al_2O_3 (0.2–0.9 wt %) and CaO (0.6–1.6). We note that orthopyroxene from Yanagisawa eruptions has diffusion zoning rather than sharp zones.

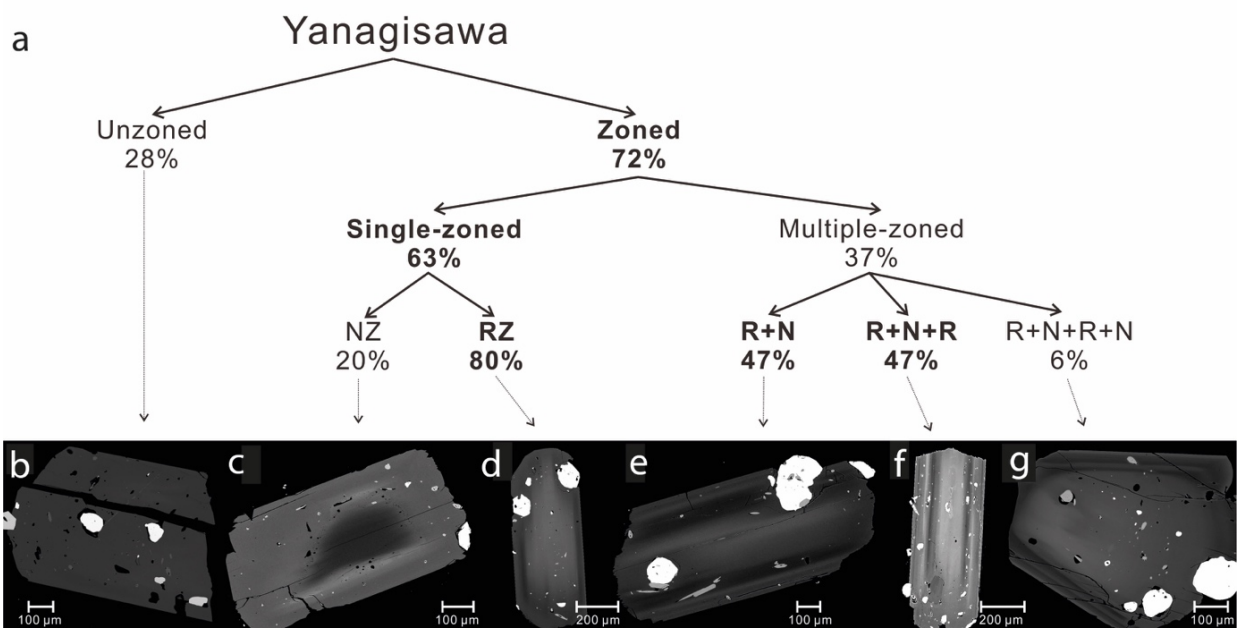

Figure 3.4. Statistical distribution of orthopyroxenes in the pumice of the Yanagisawa (a) deposits, respectively. The predominant types for each eruption are shown in bold.

Amphibole

Yanagisawa tuffs contain abundant phenocrysts of amphibole. The phenocrysts are well-shaped (Fig. 3.5 a and b). There are no melted or resorbed forms. The size does not exceed 1 mm in elongation. Inclusions of Fe-Ti oxides and slightly crystallized MIs in rhyolitic composition are extremely rare. The amphibole is not found as an inclusion in other minerals, indicating that it crystallized during the final stages of Yanagisawa magma evolution. Most amphibole belongs to the magnesio-ferri-hornblende groups with Mg-number 58–67, Al_2O_3 5.5–9.2 wt %, and Na_2O 1.1–2.1 wt % (Figure 3.6). Only one crystal with weak zoning has been found with a core composition of 9.2 wt% Al_2O_3, 2.1 wt% Na_2O, Mg-number 58, and rim 5.9–6.4 Al_2O_3, 1.4–1.5 Na_2O, and Mg-number 65.

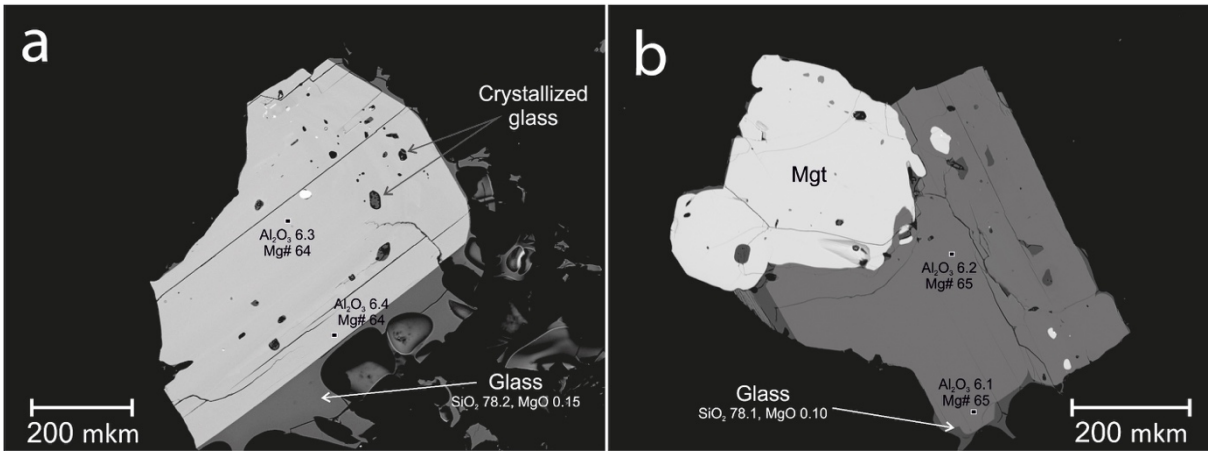

Figure 3.5. BSE images of the amphibole Yanagisawa Tuffs (d-f). Numbers showing Mg-number based on EPMA analysis in black spots Mg-number = [$X_{Mg}/(X_{Mg} + X_{Fe}) \times 100$]. Mgt- Magnetite, Amph- amphibole.

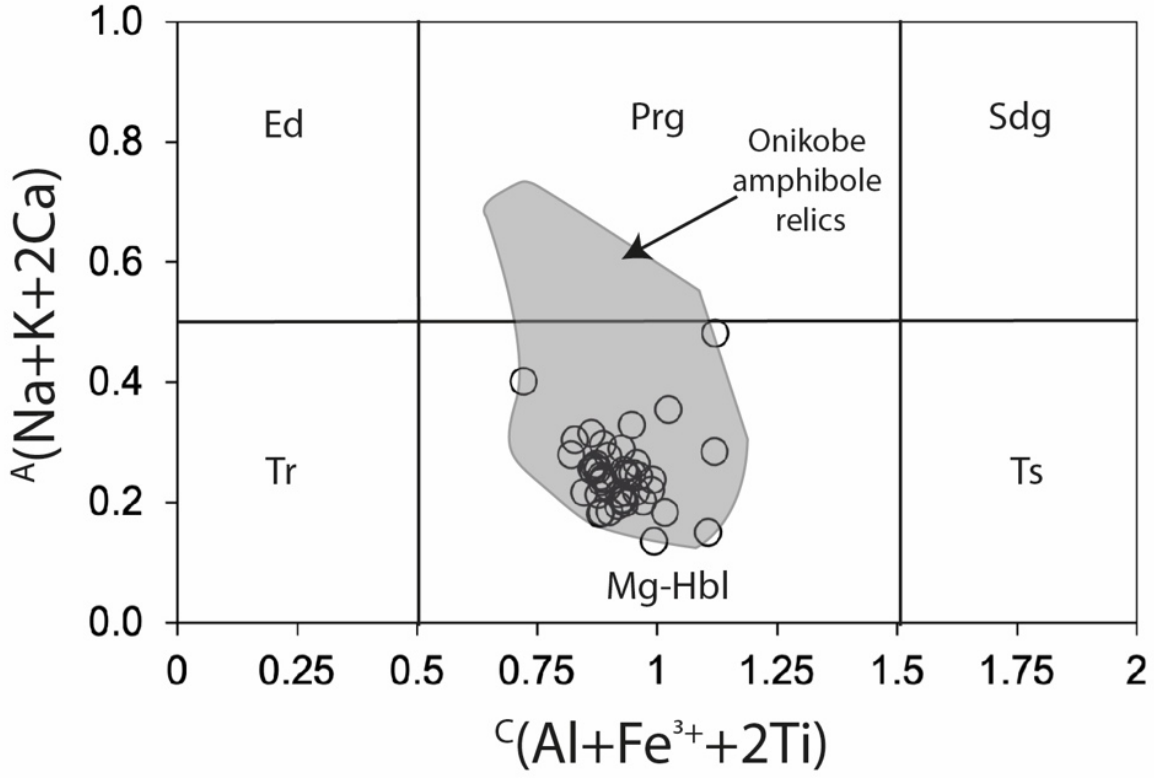

Figure 3.6. Amphibole composition diagram by (Hawthorne et al., 2012); Calculated using a spreadsheet, formula units were calculated based on 22 oxygens (Locock, 2014). Ed - edenite; Prg - pargasite; Sdg - sdanagaite; Tr - tremolite; Mg-Hbl - magnesio-hornblende; Ts – tschermakite. Grey field correspond to the amphibole composition from Onikobe pyroclastic discussed below.

Quartz

Quartz crystals from both eruptions reach 3 mm in size and have an irregular isometric shape, often melted rims. Quartz from both eruptions does not occur as inclusions in other minerals and does not contain any other minerals. Quartz contains abundant melt embayments.

Based on cathodoluminescence observation we found different zoning patterns in quartz from both eruptions. More detailed zoning features described in the Chapter 5.

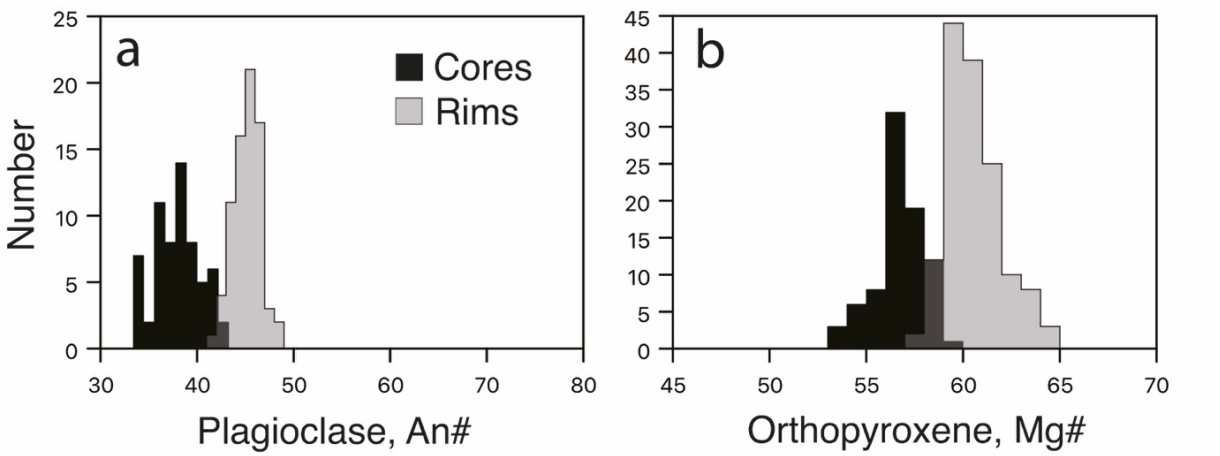

*Figure 3.7. Histograms of core and rim composition of zoned crystals of plagioclase (a) and orthopyroxene (b) in Yanagisawa tuffs. An#=Ca*100/(Ca+Na+K); Mg#=Mg*100/(Fe+Mg).*

Fe-Ti oxides

Titanomagnetite and ilmenite are present as phenocrysts in Yanagisawa pumice. There are no clear correlations between these minerals' abundance or distribution within the studied pyroclastic sequence. It also appears as an inclusion within these minerals. Titanomagnetite phenocrysts contain abundant apatite inclusions, rare Fe-sulfides (up to 5 μm in size), and rhyolitic MIs. All studied titanomagnetite and ilmenite grains are homogeneous in composition. Ilmenite is much rare than titanomagnetite in both eruptions. Titanomagnetite and ilmenite often occur together as inclusions within the same growth zones in pyroxenes and less frequently in plagioclase. In both eruptions, the most abundant Fe-Ti oxide is in inclusions in the outer zones of orthopyroxene. Sometimes they form clusters with pyroxenes. Touching pairs of titanomagnetite-ilmenite is rare. Titanomagnetite from Yanagisawa tuffs contains 8.5–9.2 TiO_2, 0.63–0.93 MnO, and 0.84–1.05 MgO. Ilmenite contains 0.87–1.31 MnO and 1.70–2.10 MgO.

3.3. Onikobe caldera-forming eruptions: Ikezuki and Shimoyamazato tuffs

3.3.1. Geological settings

Onikobe caldera located northwest of Naruko Volcano in the same volcanic cluster (Fig. 3.1). In this study, we consider two deposits related to the Onikobe caldera eruptions Ikezuki tuffs and Shimoyamazato tuffs. Estimated volume of caldera eruptions for Ikezuki tuffs of 18 km^3 DRE (as a minimum because of significant erosion) (Tsuchiya et al., 1997). There are no reliable estimates of the volume of erupted material for the Shimoyamazato tuffs, but rough

estimates suggest that the volume of erupted material is in the first km^3. The most recent thermoluminescence age studies suggest that the Ikezuki eruption occurred in the period around 296 ± 38 ka and 268 ± 33 ka (for different parts of deposit). The Shimoyamazato tuffs have been dated to 169 ± 43 ka and 170 ± 69 ka at two sites (Takashima et al., 2006). Results of previous geophysical investigations show low Vp/Vs anomalies at the surface, caused by the presence of a hot vapour phase in the Onikobe caldera area. Onikobe exhibit low Vp and low Vs anomalies at depths greater than 10 km, whereas at 2.5 km depth, no prominent low-velocity anomalies corresponding to caldera exist (Nakajima and Hasegawa, 2003; Tamura and Okada, 2016).

Ikezuki pyroclastic flow is common north and east of the Onikobe caldera. The maximum thickness reaches 100 m. At the basement of the pyroclastic flow is a layer of pumice and ash not more than 2 meters thick. The overlying main part of the pyroclastic flow is composed of dense welded tuffs. In the welded tuffs deposit, there are several pyroclastic flows, which are sometimes separated by thin ash layers. It is noted that the welded tuffs contain inclusions of non-welded pumices up to 4-5cm (not fiamme), which, however, have a flattened shape. The number of pumice inclusions increases upward in the deposit (Tsuchiya et al., 1997). Tuffs include abundant lithic nonmelted xenoliths.

Shimoyamazato tuff is widespread in the east side of the Onikobe caldera. The deposits of eruptions consist of non-welded pyroclastic flows. Most of the tuffs are deposits of pyroclastic flows filling the valleys, so their thickness varies greatly depending on the location of observation, but the thickest layers are about 30-40 m thick. The Shimoyamazato tuffs unconformably overlie the Ikezuki tuffs. The Shimoyamazato tuff consists of ash deposits at the base of the section and overlying pumice pyroclastic deposits. The pyroclastic flow deposits consist of several flow units, but each unit is 10 meters or more thick, and overlap of several flow units in one outcrop is rare (Tsuchiya et al., 1997). Lithologic differences between the flows are not observed. In this dissertation we use samples taken from all parts of the both deposits.

3.3.2. Whole-rock composition and mineralogy

The bulk rock major element compositions of the Shimayamazato and Ikezuki eruptive products are shown in Fig. 3.8. a-d. Samples Ikezuki pyroclastic flow belong to low- to moderate-potassium dacites. At the same time, we note that non-welded pumice from earlier pumice-pyroclastic deposits is slightly enriched in SiO_2, and alkalis compared to subsequent

deposits of the pyroclastic flow composed by welded tuffs. Shimoyamazato eruptive products belong to the moderately-K rhyolites (Fig. 3.8. b) (1.7–1.8 wt% K_2O).

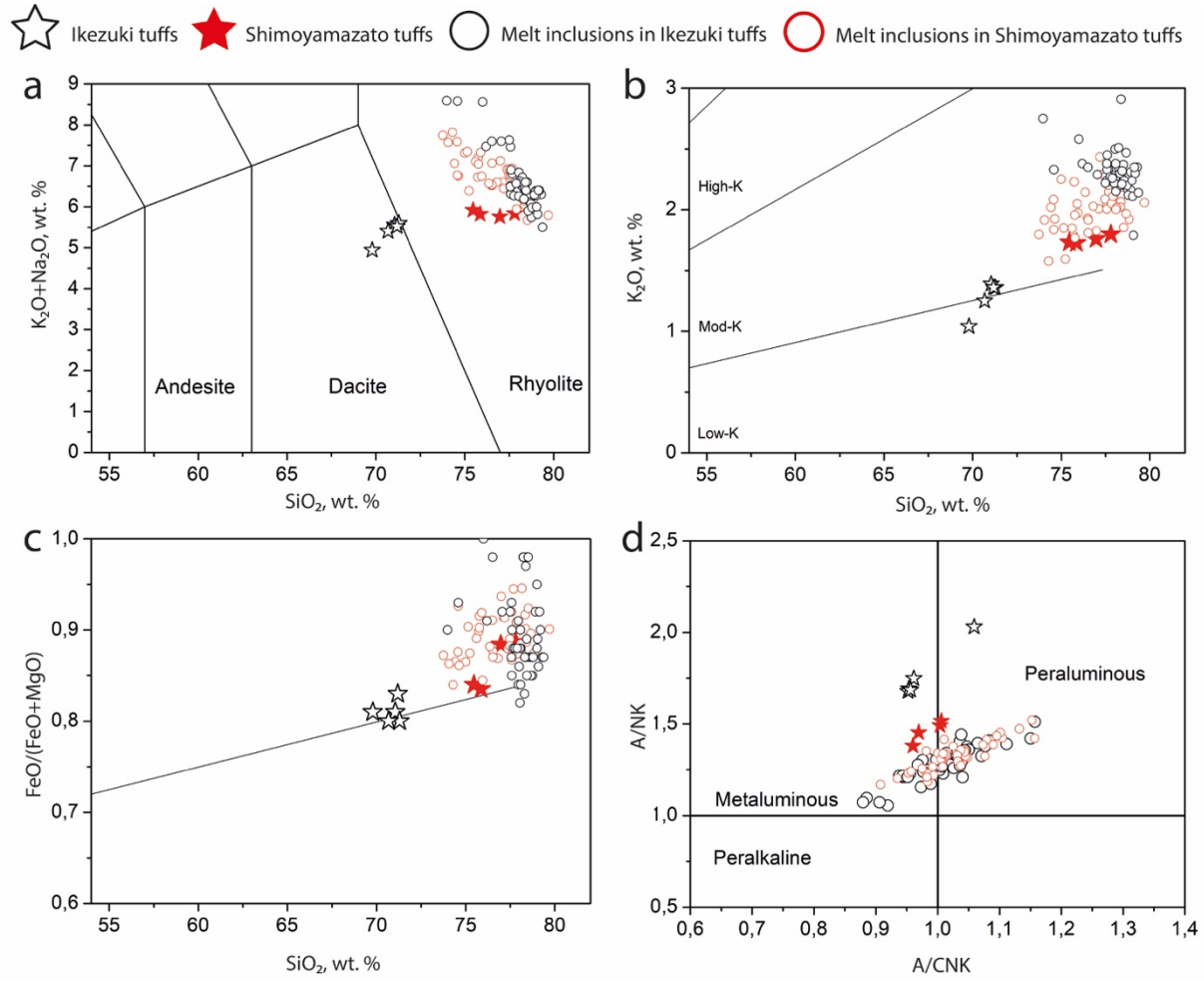

Figure 3.8. Whole-rock compositions of Onikobe caldera eruptions. Classification diagrams of (a) Na_2O + K_2O versus SiO_2 (Bas et al., 1986), (b) K_2O versus SiO_2 (Rickwood, 1989), (c) FeO/(FeO + MgO) versus SiO_2 (Frost et al., 2001) and (d) A/NK versus A/CNK (Shand, 1943). All data are volatile-free and normalized to 100 wt.%. All Fe is FeO. A/CNK = $(Al_2O_3/101.96)/(CaO/56.08 + Na_2O/61.98 + K_2O/94.2)$; A/NK = $(Al_2O_3/101.96)/(Na_2O/61.98 + K_2O/94.2)$; MALI = $Na_2O + K_2O - CaO$.

Mineral assemblage and textural compositions are similar in non-welded bottom part and welded tuffs of Ikezuki tuffs. Ikezuki mineral assemblage consists of quartz, plagioclase, ortho- and clinopyroxene, Fe-Ti oxides and extremely rare, melted amphibole. Shimoyamazato mineral assemblage consist of quartz, plagioclase, orthopyroxene and Fe-Ti oxides. Amphibole and clinopyroxene absence as a phenocryst.

Plagioclase

In both Ikezuki and Shimoyamazato deposits, we can distinguish two types of plagioclase texture: first type correspond to concentrically zoned plagioclase dominates in the

phenocryst association of both deposits. Composition of plagioclase do not vary significantly in such crystals. Second type correspond to plagioclase with complex zoning presented by patchy core and concentrically zoned outermost part.

Plagioclase is abundant in Ikezuki tuffs, up to 2.0-2.5 mm size. Phenocrysts are usually clear and euhedral. Compositional and textural diversity of minerals are similar in the lower unwelded tuffs and in the upper welded pyroclastic flows of Ikezuki. Unzoned plagioclase crystals and plagioclase at the contact with groundmass always have composition of An mol% = 54-61. Plagioclase with complex texture (patchy core and concentric outermost part) is very abundant in Ikezuki tuffs (Fig. 3.9 a-c). Patchy plagioclases contain abundant inclusions of clino- and orthopyroxenes, Fe-Ti oxides and rare melted amphibole inclusions, usually together with rhyolitic glass. Composition of high-Ca patches in such cores vary within An mol% 81-91.

In Shimoyamazato tuffs plagioclase phenocrysts are usually clear and euhedral (up 2 mm long). Concentrically zoned plagioclase dominates in the phenocryst association. Such plagioclase has a weakly oscillatory structure with the composition varying within An_{35-56}. The maximum range of An content in such crystals does not exceed 15 units (Fig. 3.9 e). It is not easy to establish a single pattern of zoning variation for this type. Plagioclase with complex texture (patchy core + concentric outermost part) are observed much less frequently than in the Ikezuki tuffs. In the patchy cores, dark patches have the composition of andesine (An_{41-56}), whereas the compositions of light patches are bytownite (up to An_{78}) (Fig. 3.9. d). As it moves away from the core, such crystals cease to be patchy and overgrow with weak zones andesine, gradually decreasing the An content. In patchy cores, low-calcium plagioclase is earlier and overgrown with high-calcium. Also, such High-Ca replacement has been found in the crystal's cores and mantle parts (Fig. 3.9. f). Rims of plagioclase in contact with groundmass glass always have a narrow composition range of nearly An_{36-41}. Thus, plagioclase from Shimoyamazato tuffs always has a rim with a lower or the same calcium content as the core. Fe-Ti oxides and rarely orthopyroxene occur as inclusions in Shimoyamazato plagioclase. Also, we found one amphibole inclusion in the patchy core. This amphibole is located in a dark patch with the composition of An_{51}.

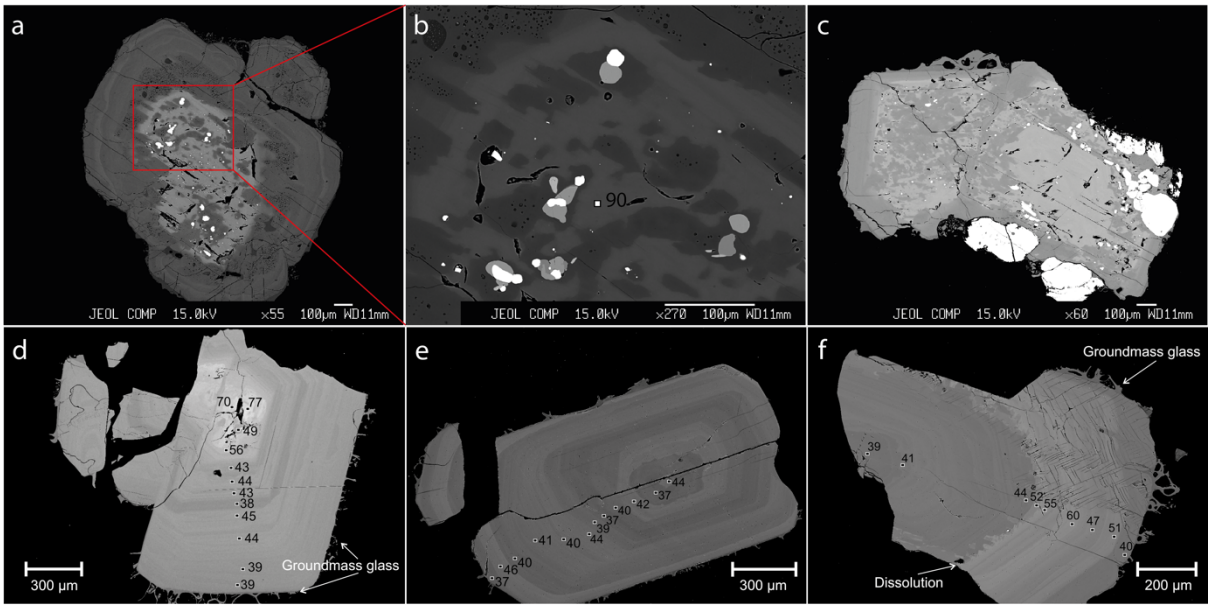

Figure 3.9. BSE images of the plagioclase phenocrysts from Ikezuki tuffs (a-c) and Shimoyamazato tuffs (d-f). (a) Ikezuki plagioclase with complex zoning (patchy core + concentric outer part and (b) zoomed patchy core of the same crystal with abundant inclusions of clino- and orthopyroxenes and Fe—Ti oxides; (c) Intergrowth of two Ikezuki plagioclase crystals with complex texture; (d-f) Shimoyamazato plagioclase with complex zoning (d), concentric zoning (e), and evidence of resorption on the border between Low-Ca and High-Ca zones (f). Numbers are shown An mol% based on EPMA analysis in black spots. #An = [XCa/(XCa + XNa+XK) × 100].

Pyroxenes

Ikezuki tuffs contain both clino- and orthopyroxenes. Composition of pyroxenes from bottom non-welded part and upper welded tuffs overlapped (Fig. 3.11a).

Clinopyroxene forms individual euhedral and subhedral crystals and crystal clots with Fe–Ti oxides, complex-zoned plagioclase, and orthopyroxene(Fig. 3.10. a-c). The clinopyroxene is classified as augite, with Mg# = 65-71 (Fig. 3.11a) (Morimoto, 1988). Clinopyroxene phenocrysts do not show significant compositional variations. Mg# values typically vary by only 1-5 units in an individual crystal.

Orthopyroxene in Ikezuki tuffs classified as enstatite (Fig. 3.11a). Mg-number vary within 54-61 units. Sometimes orthopyroxene have normal zoning with higher Mg-number in the core and lower in the rim with compositional difference less than 6 Mg#.

In addition, we pay attention to the presence of “mafic” clots represented by clino-, orthopyroxene and sometimes patchy plagioclase (Fig. 3.10 a). The composition of pyroxenes in such assemblages is slightly more enriched with MgO (Cpx Mg# 72-79 and Opx Mg# 67-71) than in other crystals from Ikezuki assemblage. Both pyroxenes in such assemblages contain

abundant inclusions of melted amphibole together with rhyolite melt. Sometimes it is possible to observe crystals of clinopyroxene, which contain oriented lamellae of orthopyroxene and amphibole (Fig. 3.10 b and c).

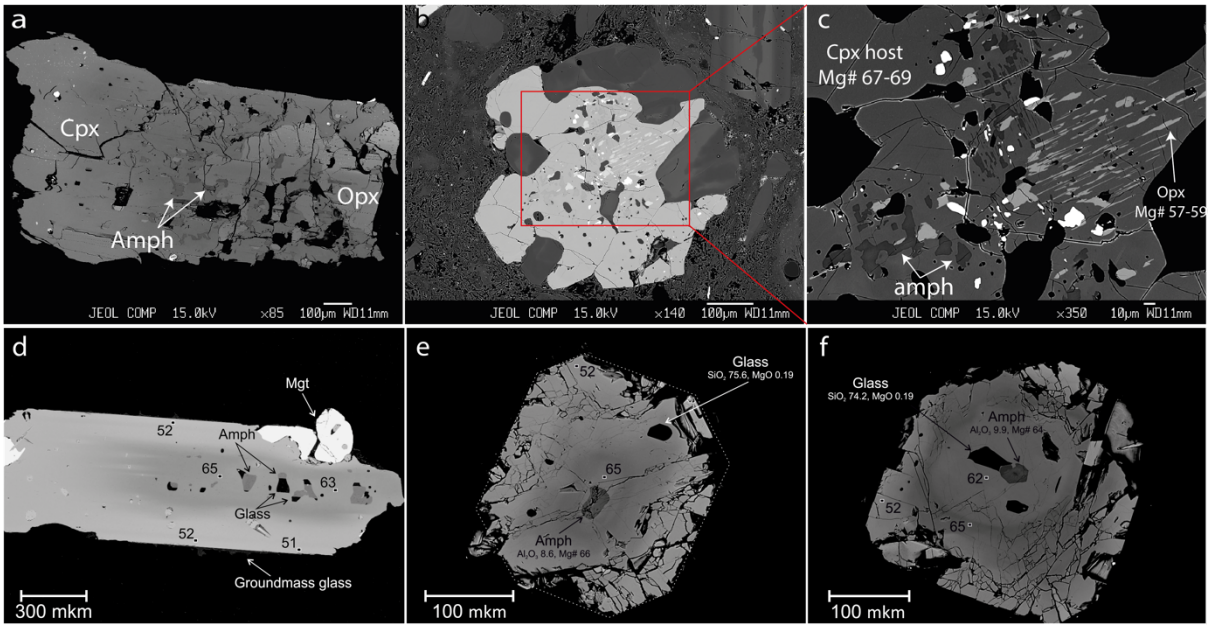

Figure 3.10. BSE images of the pyroxenes from Ikezuki tuffs (a-c) and Shimoyamazato Tuffs (d-f). (a) "Mafic" clot of clino- and orthopyroxene crystals in Ikezuki tuffs with abundant amphibole inclusion; (b and c) Ikezuki clinopyroxene crystal oriented lamellae of orthopyroxene and amphibole; (d) Shimoyamazato orthopyroxene crystal cut along the C axis with amphibole inclusions located in the Mg-rich core; (e and f) Shimoyamazato orthopyroxene crystal cut across the C axis with amphibole inclusions located in the Mg-rich core; Note the mantle High-Mg zone between core and rime in the crystals cut across C-axis. Numbers showing Mg-number based on EPMA analysis in black spots Mg-number = [$X_{Mg}/(X_{Mg} + X_{Fe}) \times 100$]. Mgt- Magnetite, Amph-amphibole.

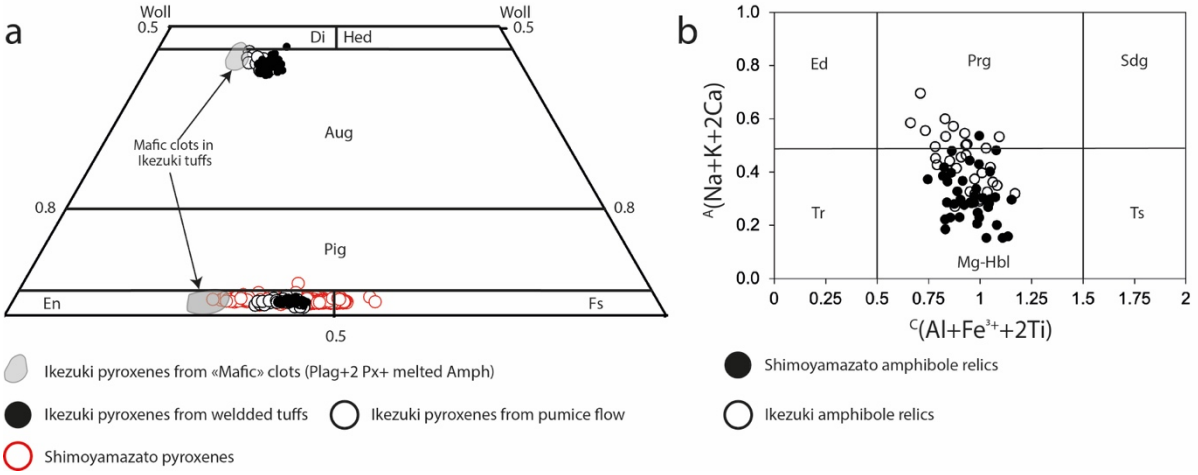

Figure 3.11. Compositions of mafic minerals in the Ikezuki tuffs and Shimoyamazato tuffs: (a) Classification of pyroxenes according to (Morimoto, 1988); (b) classification of amphiboles following (Hawthorne et al., 2012). Calculated using a spreadsheet, formula units were calculated based on 22 oxygens (Locock, 2014). Ed, edenite; Prg, pargasite; Sdg, sadanagaite; Tr, tremolite; Mg-Hbl, magnesio-hornblende; Ts, tschermakite.

Shimoyamazato tuffs include only orthopyroxene. The composition of orthopyroxenes of the Shimoyamazato orthopyroxenes varies in much greater ranges than that of the Ikezuki orthopyroxenes. In Figure 3.12, we present the results of statistical analysis of the zoning patterns of the Shimoyamazato orthopyroxene to summarize the variety of textures. Such statistical analysis was performed only for the Shimoyamazato and Yanagisawa orthopyroxenes and was not done for the Ikezuki tuffs in this dissertation. Zoned crystals of each eruption were classified according to the type of zonation observed: single zonation (normal or reverse) and multiple zonation. Each type considering as a travers from core to the rim. In Shimoyamazato pumice, of 156 crystals studied, 54% are zoned, with a prevalence in single-zoned and particularly in normal-zoned crystals. No one reverse single-zoned crystal observed in Shimoyamazato assemblage. Among multiple-zoned crystals, those with combination of reverse and normal zoning from the center to the rim prevail (Fig. 3.12 d and f). Rims at contact with the groundmass glass have Mg-number 48–52. Sometimes phenocrysts cut perpendicular to the crystallographic axis C have a mantle high-Mg zone with a slightly higher Mg composition than the core (Fig. 3.12 d). However, this pattern is rare. Such abundant reverse and/or multiple zoning in Shimoyamazato orthopyroxene is similar to the observed features for Shimoyamazato plagioclase. Thus, we can distinguish three composition group of Shimoyamazato orthopyroxene: (1) Intermediate-Mg (Mg-number 54–64) form cores, (2) High-Mg broad zone (Mg# 64–69) mostly form mantle zone, but rare occurred as a core and (3) Low-Mg (48–53) which forms outermost part on the contact with groundmass glass or unzoned crystals. The Mg-number has a strong positive correlation with SiO_2 content (50.5–53.5 wt %), Al_2O_3 (0.2–1.5 wt %), weakly positive with CaO (0.8–1.6), and strong inverse with MnO (0.9–2.4 wt %). The TiO_2 (0.04–0.33 wt %) contents do not correlate with Mg-number. The most abundant minerals included in Shimoyamazato enstatite phenocrysts are apatite, magnetite, ilmenite, and melted amphibole (in the cores with Intermediate Mg-number 54–64 (group 1) .

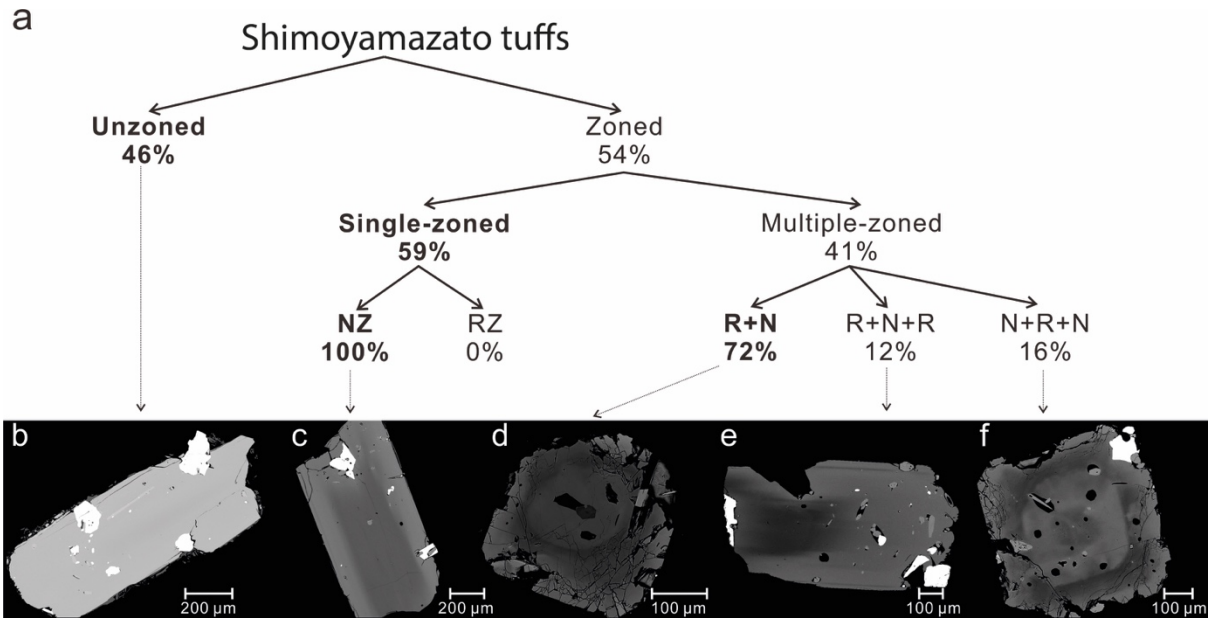

Figure 3.12. Statistical distribution of orthopyroxenes in the pumice of the Shimoyamazato deposits. The predominant types for each eruption are shown in bold.

Amphibole

Amphibole is absent in the form of phenocrysts and is present only as melted relict inclusions in both eruptions of the Onikobe caldera discussed here.

In Ikezuki tuffs amphibole is abundant as melted inclusions in both pyroxenes and rarely in patchy plagioclase cores. Amphibole inclusions belong to the Mg-hornblende and Tschermakite groups with Mg-number 53–71, Al_2O_3 6.25–10.0 wt %, and Na_2O 1.5–2.9 wt%. Most Mg-rich amphibole found in those "mafic" Cpx-Opx-Plag clots (Fig. 3.10 a; Fig. 3.11).

Like Ikezuki tuffs, Shimoyamazato tuff does not contain amphibole phenocrysts, but this mineral occurs as inclusions in orthopyroxene cores (Mg-number 54-65) and is rare in patchy cores of plagioclase. Such inclusions have a melted irregular shape and often occur together with rhyolite glass. Amphibole inclusions belong to the Mg-hornblende group with Mg-number 58–73, Al_2O_3 5.8–9.9 wt %, and Na_2O 1.2–2.2 wt%. Mg-number of host orthopyroxene correlates positively with Mg-number of amphibole inclusion.

3.4. Melt composition in Naruko and Onikobe magmas

Primary MIs found in all minerals from both Onikobe and Naruko deposits. MIs are arranged as azonal groups or along crystal growth zones. Quartz contains only azonal groups in different crystal parts, while plagioclase and pyroxene contain both azonal and zonal groups of MIs. Apatite also contains tubular MIs. Inclusions in quartz and plagioclase are usually strongly devitrified and brown. The degree of devitrification may vary slightly within a single

crystal, but good correlation between the location of the MI and the degree of crystallization was not found. Inclusions in pyroxenes, on the contrary, are less devitrified. Some MIs in pyroxene may show nucleation of daughter minerals and crystallization of the host mineral on the wall of inclusion, but there are also MIs without evidence of post-entrapment crystallization. Degree of crystallization and PEC is much higher in welded Ikezuki tuffs than in all other deposits because of significant overheating during the eruption. This study used only MIs in quartz and plagioclase after the homogenization experiment (see chapter "Melt inclusion homogenization experiments" or inclusions in orthopyroxene and clinopyroxene without significant evidence of PEC.

Inclusions of all minerals from Onikobe and Naruko eruptions have a rhyolitic composition. At the same time, slight differences were noited in composition depending on the host mineral and belonging to one of the two calderas. Here we consider MIs from both calderas togheter.

In the Figure 3.13. we show composition of MIs from Ikezuki, Shjimoyamazato and Yanagisawa deposits together. MIs in Ikezuki tuffs have the same almost same composition as MIs from Shimoyamazato tuffs and vary within SiO_2 70.8–76.2 wt%, Al_2O_3 10.5–13.9 wt % , FeO 1.0–1.5 wt %, MgO 0.1–0.3 wt %, CaO 1.0–1.6 wt %, Na_2O 3.2–5.9 wt %, K_2O 1.5–2.1 wt % (all hydrous). We note only slight enrichment in K_2O and depletion in FeO, MgO and CaO compared to MIs from Shimoyamazato. Those differences might be related to higher degree of MIs crystallization in Ikezuki and not complete homogenization after experiments (not all Fe-, Mg-, and Ca-rich daughter phases melted).

For MIs in Shimoyamazato pumice we note difference in composition between MIs in orthopyroxene and quartz. Mis in orthopyroxene have the lowest SiO_2 composition (70.2–74.3 $SiO_{2(hydrous)}$ wt%), with Al_2O_3 composition 11.9–13.6 wt %, FeO 1.1–1.9 wt %, MgO 0.1–0.3 wt %, CaO 1.1–2.1 wt %, Na_2O 4.2–5.9 wt %, K_2O 1.5–2.1 wt % (all hydrous). MIs from quartz in Shimoyamazato pumice mostly evolved in the composition of all major elements, which the better shown in SiO_2 composition 71.6–75.6 wt %, Na_2O 3.4–4.5 wt %, and K_2O 1.8–2.3 wt %. Groundmass in Shimoyamazato tuffs overlapped in composition with MIs from quartz.

MIs from Yanagisawa phenocrysts vary within a narrower range, but we note the same difference in composition between MIs in quartz and orthopyroxene (Fig. 3.13 a-e). All MIs in orthopyroxene take a more primitive position in all elements compared with MIs in quartz and groundmass. SiO_2 concentration in MIs from orthopyroxene in Yanagisawa pumice vary within

72.2–75.0 wt %, with Al_2O_3 composition 11.3–12.1 wt %, FeO 1.5–1.8 wt %, MgO 0.1–0.2 wt %, CaO 1.3–1.7 wt %, Na_2O 4.0–4.7 wt%, K_2O 1.6–2.0 wt % (all hydrous). The difference between MIs in orthopyroxene and quartz is not so significant, but we note that MIs from pyroxene have mostly fractionated composition in all major elements. Groundmass composition in Yanagisawa pumices is completely overlapped in composition with MIs composition.

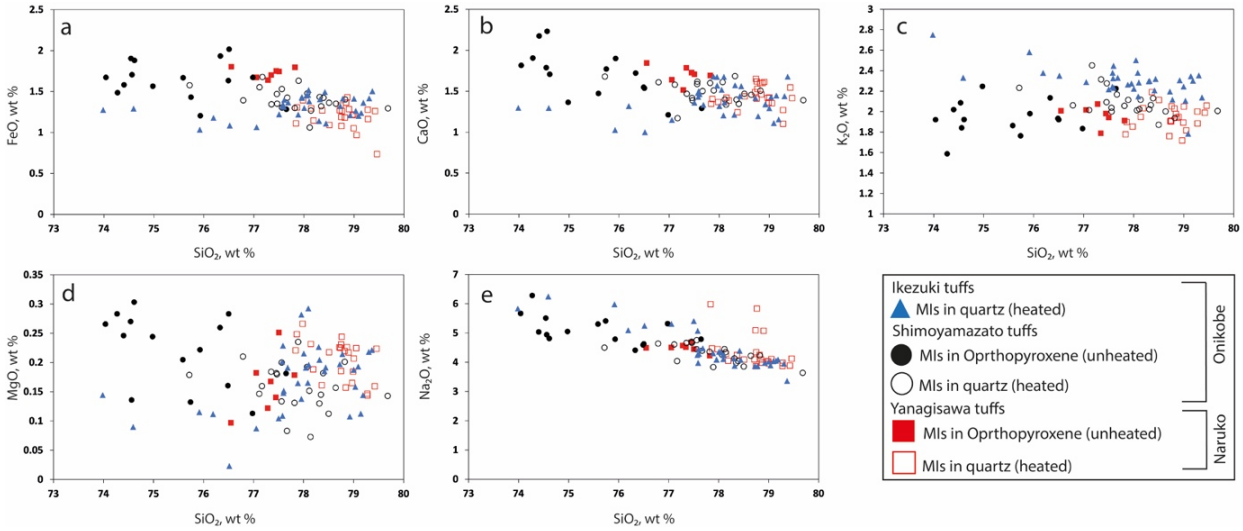

Figure 3.13. Variations of the major elements in MIs from orthopyroxene and quartz and groundmass glasses from Ikezuki tuffs, Shimoyamazato pumice and Yanagisawa pumice. All data are plotted volatile-free, normalized to 100%. Al Fe as FeO.

3.5. Volatile content in melts from Onikobe and Naruko calderas

SIMS has been used for volatile elements (H, C, P, S, F, Cl) determination in MIs from both calderas and groundmass glass (Fig. 3.14).

No clear differences were not found in volatile content between inclusions in different minerals or different pyroclastic flows Ikezuki. MIs from Ikezuki tuffs depleted (3.6-4.8 wt %) in H_2O compared to melts from Shimoyamazato pumice (4.3–5.9 wt %). CO_2 content vary from the detection limit (3 ppm) to 16 ppm in Ikezuki tuffs and from detection limit to 17 ppm in Shimoyamazato. Ikezuki melts are slightly enriched in sulfur content compared to Shimoyamazato melts. In Ikezuki melts concentrations of P_2O_5 range between 0.015 and 0.044 wt. %. Fluorine content in MI ranges between 510 and 707 ppm and positively correlates with chlorine concentration. Chlorine concentration varies from 0.14 to 0.23 wt % in all MIs. Ikezuki melts are enriched in halogens compared to Shimoyamazato ones (Fig. 3.14 b).

In Shimoyamazato melts concentrations of P_2O_5 range between 0.020 and 0.035 wt. % in MIs. Fluorine content in MI ranges between 106 and 640 ppm and positively correlates with chlorine concentration. Chlorine concentration varies from 0.10 to 0.21 wt % in all MIs. Shimoyamazato quartz is considerably enriched in fluorine compared to orthopyroxene (518–640 ppm in quartz against 303–588 ppm in orthopyroxene). The only exceptions are the three MI analyses in quartz, which are significantly depleted in fluorine (F 106–133 ppm) and fall outside of this trend. The reasons for this depletion remain unclear because the loss of volatiles due to homogenizing experiment for these inclusions is ruled out. After all, the water content of these inclusions is the same as that in the other inclusions (H_2O 4.75–4.93 wt %). One more exceptional analysis is MI in orthopyroxene, which has a chlorine composition of 0.22 wt % and falls from the common trend in Shimoyamazato MIs (Fig. 3.14 b).

MIs from Yanagisawa quartz and orthopyroxene have H_2O contents of 4.0–5.1 wt%. CO_2 content from the detection limit (3 ppm) to 18 ppm. Sulfur content from the detection (0.1 ppm) limit to 38 ppm S. Concentrations of P_2O_5 range between 0.024 and 0.031 wt% of P_2O_5. Fluorine content in MI ranges between 28 and 450 ppm and positively correlates with chlorine concentration. Chlorine concentration from 0.12 to 0.18 wt% in all MIs.

The groundmass glass are relatively depleted in H_2O (1.5–2.4 wt%) and fluorine (120–201 ppm), but there is no significant difference in S (19–22 ppm), Cl (0.15 wt%), and P_2O_5 (0.029 wt%) concentrations compared to the Yanagisawa melts.

The concentrations of volatiles in the melt inclusions of both calderas are typical for silicious magmas and are not out of line with the general trend throughout the NE Honshu-Hokkaido-South Kurile region. On average, rhyolitic MIs in dacites and rhyolites of this NE Honshu – Southern Kuril region have 3–7 wt.% H_2O (mean 4.5–5 wt.%), markedly low CO_2 and S contents (<50 and <250 ppm, respectively), 0.1–0.4 wt.% Cl, and up to 0.18 wt.% F (Miyagi et al., 2012, 2017; Amanda et al., 2019; Smirnov et al., 2019; Kotov et al., 2021; Kotov et al., 2023).

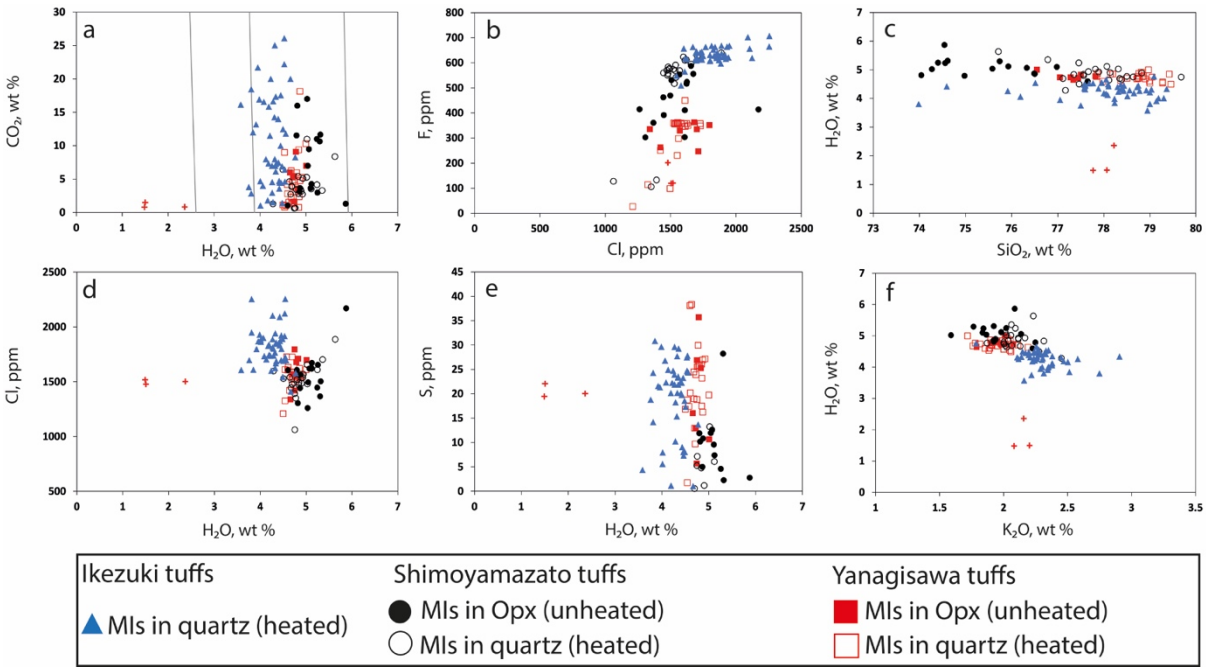

Figure 3.14. Volatile elements variations MIs from orthopyroxene, quartz, and groundmass glasses from Ikezuki, Shimoyamazato, and Yanagisawa tuffs. SiO_2 and K_2O content are plotted volatile-free, normalized to 100%. Isobars plotted based on VolatileCalc calculation under 850°C (Newman & Lowenstern, 2002).

3.6. Discussion

3.6.1. P-T-fO parameters of Ikezuki and Shimoyamazato magma

Based on the observed mineralogy, we applied the following geothermometers: (1) Touching Fe–Ti oxide pairs (Ghiorso and Evans, 2008) and (Andersen and Lindsley, 1985); (2) plagioclase-melt geothermometer (Putirka, 2008); (3) orthopyroxene-melt geothermometers (Putirka, 2008) and (4) Amphibole geothermometry (Ridolfi and Renzully, 2012; Putirka, 2016; Ridolfi, 2021).

In Ikezuki tuffs we applied two-pyroxene (Putirka, 2008 equation 26 and equation 27). Orthopyroxene-clinopyroxene pairs from "mafic" clots (e.g., Fig. 3.10a) yield temperature 886-940 °C, while other pairs from tuffs yield 788-852 °C (Fig. 3.15a).

In Ikezuki tuffs plagioclase liquid thermometry of (Putirka, 2008, equation 24a) has been applied for pairs of MIs - host plagioclase only for homogenized MIs with known H_2O content after SIMS analysis. Resulting temperature varies between 830-856 °C (Fig. 3.15a).

We applied (Ghiorso and Evans, 2008) and (Andersen and Lindsley, 1985) geothermometers and oxygen barometers to titanomagnetite and ilmenite compositions to determine pre-eruptive temperatures and oxygen fugacity. Temperature and oxygen fugacity are estimated for all touching pairs. Further, we used non-touching pairs from the same

pyroxene zone because their compositions are identical to the touching pairs, and we obtained overlapping results. All used pairs passed the (Bacon and Hirschmann, 1988) test of Fe–Ti oxide equilibrium. In Shimoyamazato tuffs, using the (Ghiorso and Evans, 2008) model, Fe–Ti oxides could be in equilibrium at temperatures of 761–808°C and oxygen fugacity of ΔNNO to ΔNNO-0.25. Following the (Andersen and Lindsley, 1985) model, Fe–Ti oxides could be in equilibrium at temperatures of 777–815 °C and oxygen fugacity of ΔNNO to ΔNNO-0.45 (Fig. 3.15c).

Orthopyroxene-liquid thermometry (Putirka, 2008, equation 28a) has been applied to pairs of Orthopyroxene rim and groundmass glass. For the temperature estimation we set H_2O content in glass as the average H_2O concentration in MIs from quartz. Only pairs with KD_{Fe-Mg} fall into the range 0.29±0.06 we used (Putirka, 2008); the temperature estimation for those pairs varies within 801-832°C (Fig. 3.15c). In Ikezuki tuffs this thermometer was not applied.

Plagioclase liquid thermometry of (Putirka, 2008, equation 24a) has been applied for pairs of groundmass glass-plagioclase in Shimoyamazato tuffs. Water content for estimation was taken as an average concentration in MIs from quartz. Resulting temperature varies between 789-813 °C in Shimoyamazato tuffs (Fig. 3.15c).

Even though Onikobe tuff does not contain amphibole phenocryst but only relict, we still estimated the pressure using equation P1b (Renzully and Ridolfi, 2012; Ridolfi 2021). The resulting pressure lies in the range from 101–232 MPa (±30 MPa) in Ikezuki and 97-253 MPa (±30 MPa) in Shimoyamazato tuffs (Fig. 3.15 b and d). We note that the instability of this amphibole does not allow these estimates to be used as reliable, but this amphibole is considered to be stable in low-pressure conditions.

In addition, we estimated H_2O-CO_2 saturation pressure using known H_2O and CO_2 content in MIs by VolatileCalc 2.0 (Newman & Lowenstern, 2002). Water saturation pressure is between 87-134 MPa in Ikezuki and 116–197 MPa in Shimoyamazato magmas (Fig. 3.15 b and d). These estimations should be considerate as a minimum possible pressure because of presence other volatiles and possible undersaturation of magmas.

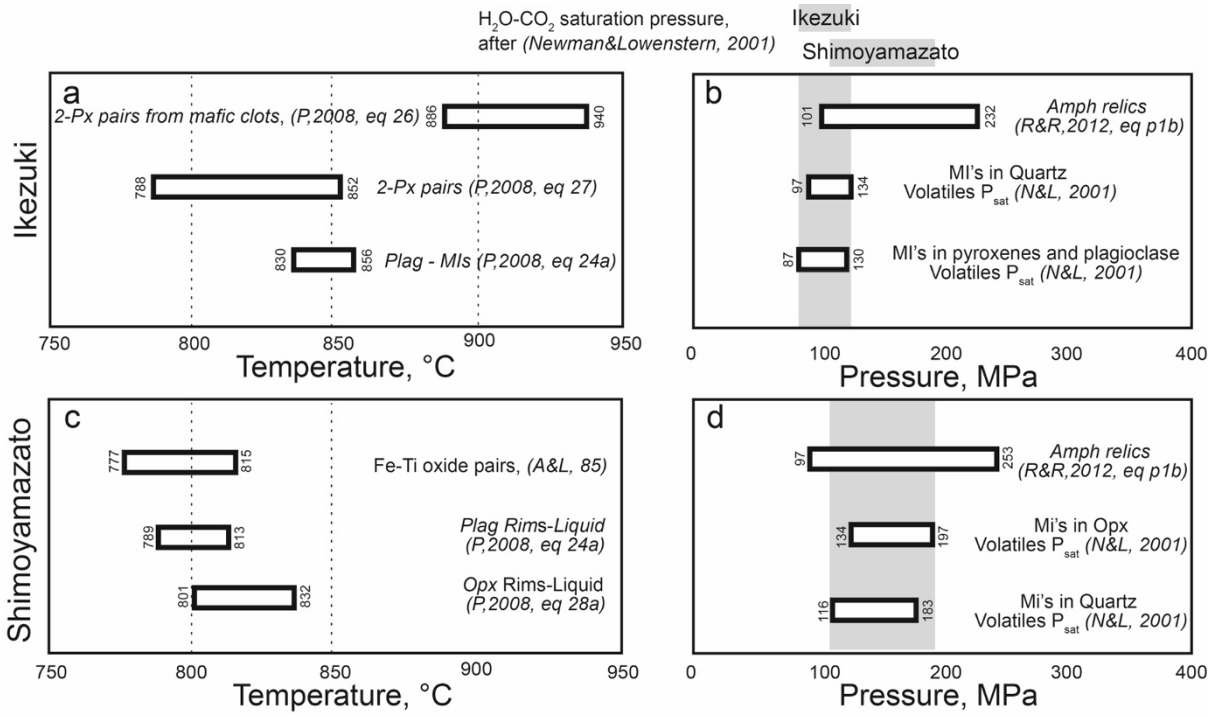

Figure 3.15. Result of thermometry and barometry application for the Ikezuki tuffs (upper row) and Shimoyamazato tuffs (bottom row), respectively. Amph - amphibole, Opx – orthopyroxene, Plag – plagioclase.

3.6.2. P-T-fO parameters of Yanagisawa magma

In Yanagisawa Tuffs using the (Ghiorso and Evans, 2008) model, Fe–Ti oxides could be in equilibrium at temperatures of 773–812°C and oxygen fugacity 0.3–0.6 above ΔNNO buffer. Following the (Andersen and Lindsley, 1985) model, Fe–Ti oxides could be in equilibrium at temperatures 804–838 °C and oxygen fugacity 0.2–0.6 above ΔNNO buffer (Fig. 3.16a).

Plagioclase liquid thermometry of (Putirka, 2008, equation 24a) has been applied for pairs of groundmass glass-plagioclase rims but not for the MIs because all MIs in plagioclase are crystallized. Water content for estimation was taken as an average concentration in MIs from quartz. In Yanagisawa, tuffs temperature varies between 821–832°C (Fig. 3.16 a).

The composition of amphibole rims from Yanagisawa tuffs and touched groundmass glass has been used for the temperature estimation (Putirka, 2016, equations 8 and 9). Amphibole crystallization temperature based on equation 8 was estimated as 790–833 °C (±47°C) and based on equation 9 as 792–816°C (±27°C). Crystallization temperature is based only on amphibole composition (Renzully and Ridolfi, 2012; Ridolfi, 2021), where models vary within a wide range of 778–882°C (±22°C). However, we note that most estimations are between 778 and 830°C, and only three analyses fall outside of this group (Fig. 3.16 a).

Pressure has been estimated using amphibole geobarometry (Ridolfi and Renzully, 2012; Putirka, 2016; Ridolfi, 2021) and yield results of 90–199 MPa (±20 MPa) (Fig. 3.16 b). For Yanagisawa we suggest that melts were H_2O-saturated before eruption because of abundant presence of fluid inclusions. Estimated H_2O-CO_2 saturation pressure is 126-157 MPa in Yanagisawa magmas (using VolatileCalc 2.0 by Newman & Lowenstern, 2002) (Fig. 3.16 b).

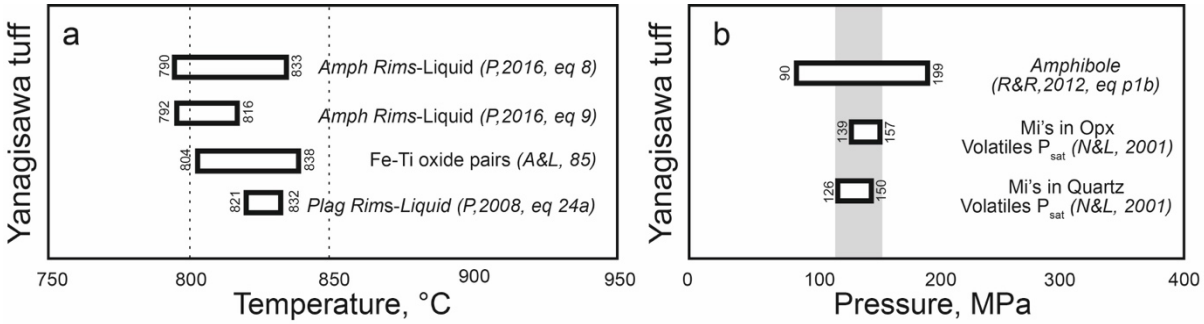

Figure 3.16. Result of thermometry and barometry application for the Yanagisawa tuffs. Amph - amphibole, Opx – orthopyroxene, Plag – plagioclase.

3.6.3. Magmatic environments and pre-eruptive magma dynamics. Case of Ikezuki and Shimoyamazato magmas

The textural and compositional features of the orthopyroxene and plagioclase phenocrysts in the both calderas strongly suggest various magmatic conditions and repetitive mixing processes.

Recently (Kahl et al., 2011) suggested an approach to define different magmatic environments (ME) in order to describe the long-term history of magmatic systems. Each internal part of a crystal can has a diverse and complex growth history, but the zoning features common to a large part of all crystals allow us to outline systematically some environments which correspond to some step in magmatic evolution history. The magmatic environment is determined by temperature, pressure, volatile and compositional content, which in turn directly affects the composition of crystallizing minerals.

Here I distinguish certain MEs for Onikobe and Naruko magmas, which show variations in major-element composition (Mg#) that can be related to changes in the magmatic system. These changes can lead to either reverse zoning, typically associated with higher temperatures, higher pressures, and higher water fugacity, or normal zoning, typically associated with cooler and shallower environments (Kahl et al., 2011; Solaro et al., 2020). The identification of ME is based on the presence of compositional plateaus in the minerals. Compositional plateaus can be interpreted as a result of growth in some defined ME, with residence times in each ME long enough to be reflected by crystal growth, but short enough that the compositional feature has

not been removed by diffusional equilibration. The repetitive appearance of compositional plateaus indicates that zoning is not a result of fractionation during growth only, but by subsequent and fast changes during crystal growth in response to a change from one ME to another, i.e., by changing temperature, pressure, *f*O, and volatile content. Thus, if the crystal grew from core to rim, then cores correspond to the first ME recorded by crystals while rims represent the latter ME (Solaro et al., 2020). Here this approach was applied to orthopyroxenes from both Naruko and Onikobe calderas in order to highlight changes in ME.

Among Shimnoyamazato orthopyroxenes, we distinguish three groups of magmatic environments: ME1 (Mg# 54-64), ME2 (Mg# 64-68), and ME3 (Mg# 48-53) (Fig. 3.17). As shown above, ME1 usually forms orthopyroxene cores in the zoned crystals. ME3 usually corresponds to either crystal rims or the entire crystal if it is unzoned. All found unzoned crystals (46%) belong to ME3. The distinguishing of ME2 is based on two reasons: 1) some Shimoyamazato multiple-zoned crystals have an mantle high-Mg zone that contrasts significantly in composition with the core and outermost part, enriched in Al_2O_3, Cr_2O_3, CaO, depleted in MnO, and is up to 100 microns thick; 2) relics of melted amphibole crystals were found only in those cores that correspond to ME2 and are surrounded by discussing ME3, indicating that the amphibole ceased to be stable when the magmatic environment changed from ME2 to ME3.

The deposit of the Ikezuki eruption contain a population of orthopyroxenes that varies in the range of Mg# 54-61 and completely coincides with ME1 for the Shimoyamazato tuffs. That is, in fact, the earliest orthopyroxenes of Shimoyamazato are the same orthopyroxenes from the Ikezuki association (e.g., Fig. 3.11a). At the same time, mafic assemblages found in Ikezuki tuffs with Mg# 67-71 completely overlap with ME2 compositions for Shimoyamazato tuffs.

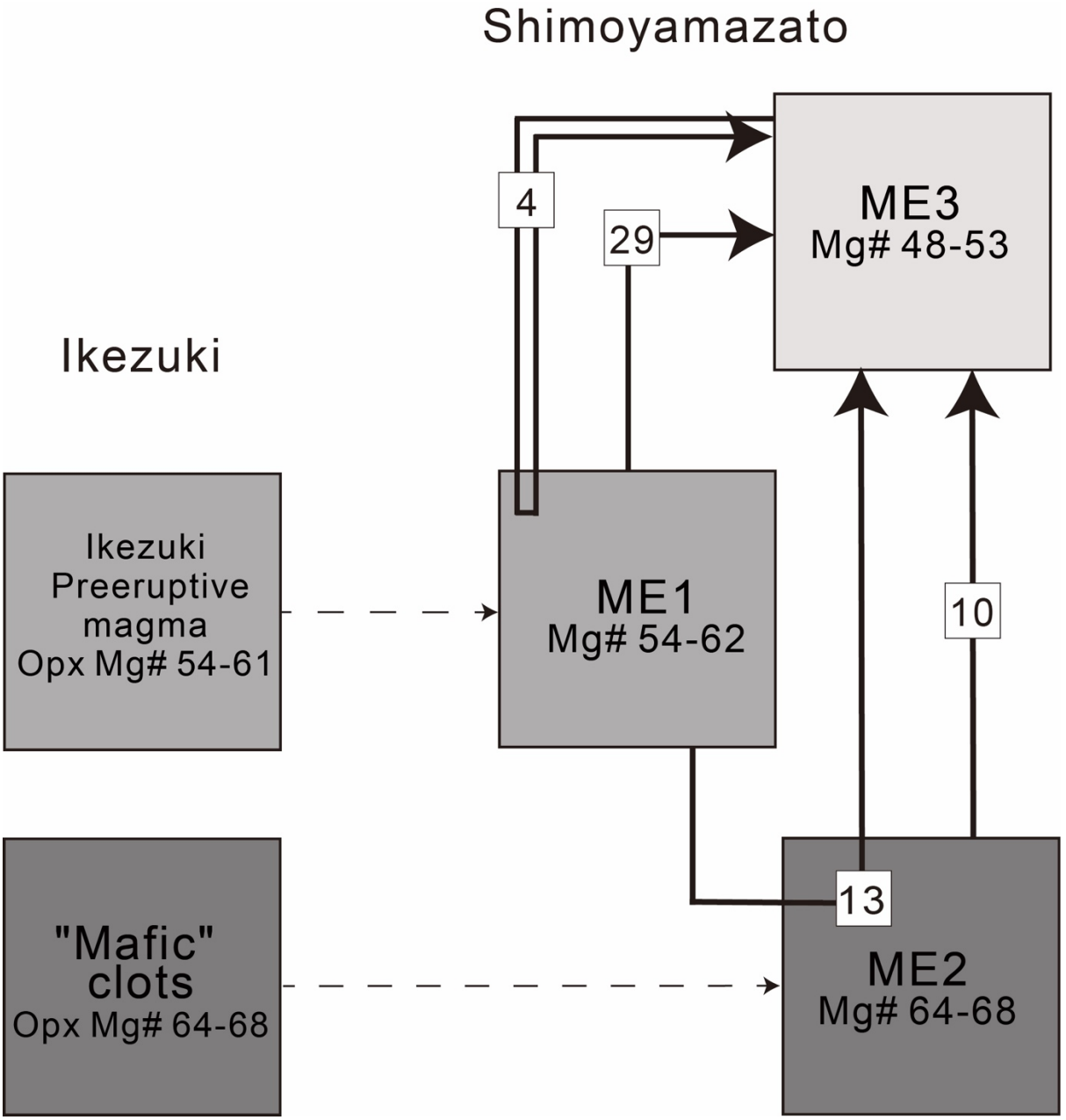

Figure 3.17. Schematical ME's connection pathways for Ikezuki and Shimoyamazato magma. Each arrow corresponds to the number of EPMA travers from core to rim, indicated observed zoning patterns.

Ikezuki magma was formed by the fractional crystallization or partial melting of those more primitive rocks that contained Mg-rich pyroxenes and tschermakite amphibole. The mechanism of formation remains debatable, because it could be either partial melting according to the example described above for Mendeleev volcano or fractional crystallization. Despite on mechanism, dacitic magma chamber was formed, the evolution of which later led to the eruption of the Ikezuki tuffs.

For the formation of the Shimoyamazato magma, we suggest that the main mechanism was remobilization of residual Ikezuki magmas, as evidenced by the specific zoning (orthopyroxene cores with amphibole inclusions are similar to those of the Ikezuki mineral

assemblage). Remobilization probably occurred under the influence of the same hot more primitive magmas from which the Ikezuki dacites were formed and to which the mafic assemblages belong.

Thus, we suggest that Shimoyamazato magma formed due to the melting of upper crustal rocks by injecting hot magma. The abundant appearance of crystals with ME1 to ME3 or ME2 to ME3 (Fig. 3.17) suggest broad processes of intrusion of hotter magmas into colder ones and further re-equilibration. The thick (>100 microns) outer zones of ME3 suggest that this process of hot magma intrusion was not the cause of the eruption and that the crystals had time to equilibrate and turn into thick outer zones (ME3). At the same time, the reverse zoning is expressed only in the transition between zones ME1 to ME2 (core to mantle), which means that ME2 was the magma that served as a source of heat.

3.6.4. Magmatic environments and pre-eruptive magma dynamics. Case of Yanagisawa magma

Observed increasing of An mol% and Mg# in plagioclase and orthopyroxene, as well as disequilibrium between melt and pyroxenes, indicate mixing with less evolved hotter magma or its rejuvenation due to interaction with it at early stages of evolution in the course of Yanagisawa magma formation.

Among Yanagisawa orthopyroxenes, we distinguish two groups of magmatic environments: ME1 (Mg# 54-60) and ME2 (Mg# 61-65) (Fig. 3.18). ME1 usually forms orthopyroxene cores in the zoned crystals, or, sometimes, outermost parts in multiple-zoned grains. ME2 correspond to the rim or mantle zones and rare to the cores if crystal have normal zoning.

Among Yanagisawa crystals, those with reverse (often multiple) zoning predominate. Evidence from the presence of mantle dark exterior zones in Yanagisawa orthopyroxene as well as resorption in inner zones of plagioclase (e.g., Fig. 3.3 and 3.4) represent mixing with, or rejuvenation through interaction with, a less evolved and/or hotter melt (e.g., Cooper et al., 2016; 2017).

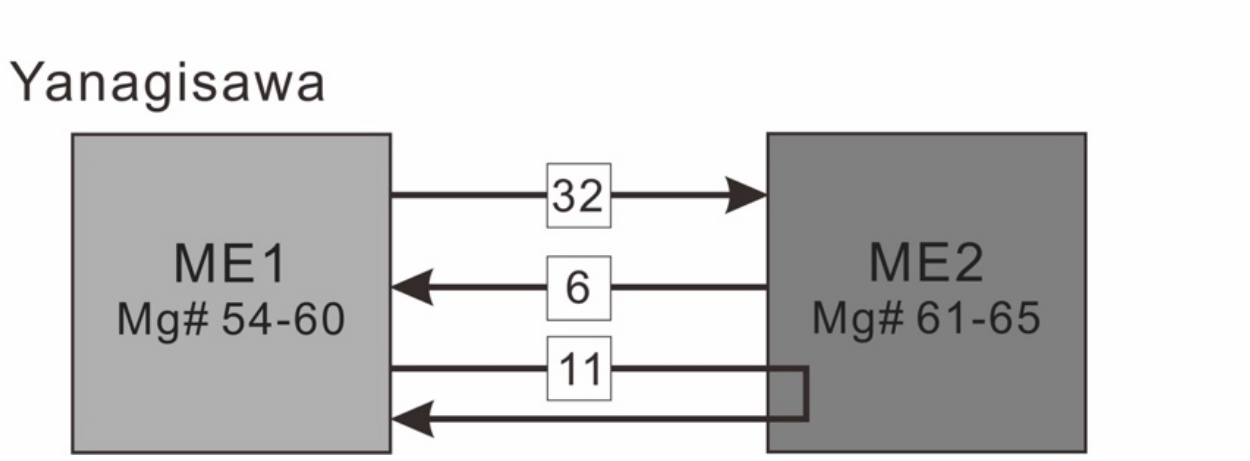

Figure 3.18. Schematical ME's connection pathways for Yanagisawa magma. Each arrow corresponds to the number of EPMA travers from core to rim, indicated observed zoning patterns.

The injection of hotter magma into a cooler host may rejuvenate (recycling the mush to generate an eruptible magma) this and initiate magma body growth and eruption. Mafic injection may penetrate the mush, producing various degrees of mixing (Bergantz & Breidenthal, 2001; Bergantz et al., 2015) or may rejuvenate it by supplying heat and (or) fluid but without material mixing (e.g., Bachmann and Bergantz, 2006; Huber et al., 2011).

Yanagisawa rhyolites have no evidence of significant admixture of other magmas, which is expressed in the (1) uniform composition of melt inclusions in all mineral zones, (2) the absence of xenoliths or xenocrysts, (3) homogeneous bulk composition, and (4) textures of all caldera deposits. In addition, there are only single crystals with normal ME2 to ME1 zoning, which implies a limited degree of mixing of these magmas.

Thus, the Yanagisawa magma formation through the rejuvenation of crystal mush (ME1) suggests due to the injection of hotter primitive magmas (ME2) (Fig. 3.19). However, this process rather did not lead to the migration of heated portions to shallower part, as there is no evidence such as broad outermost zones with lower-Mg or lower-Ca content, unlike the observed ME3 in the Shimoyamazato magma. That is, the erupted Yanagisawa magma was formed in situ and did not migrate far from place of its generation. The presence of streaky outermost zones with multiple zoning suggests that the same magma portions could have been heated many times. Probably, this is evidence of the growth of the magmatic chamber directly from the crystal mush without segregation of mobile portions to the shallower part.

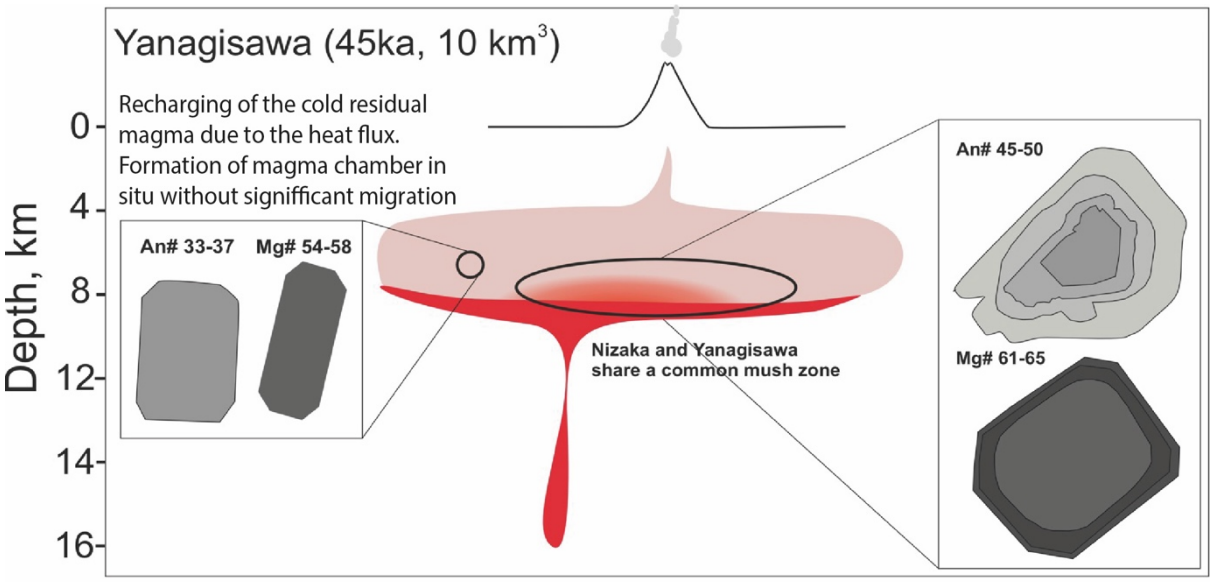

Figure 3.19. Cartoon cross-section of the Yanagisawa magma system. The magmatic processes inferred from crystal textures and chemistry (discussed in the text).

3.7. Conclusions

In this section, by studying in detail the mineralogy and inclusions in the Onikobe and Naruko caldera-forming deposits, the nature of the origin of their magmas were elucidated. In both cases, the magmas were dislocated in upper crustal low-depth conditions before eruption.

The "mafic" clots in the Ikezuki magma indicate a significant influence of more primitive magmas. But it remains unclear whether this was partial melting of more primitive crustal rocks or whether the mafic assemblages are xenoliths from the parental melt, the crystallization of which led to the formation of Ikezuki dacites. Detailed observation of the distribution of mineral zoning patterns allows us to suggest that the most probable mechanism of Shimoyamazato magmas is the rejuvenation of Ikezuki magmas due to the strong influence of hotter magmas. The mobilized portions of magma were re-equilibrated with the rhyolite melt. The process was not accompanied by significant mixing and hybridization of newly formed magmas. Before the eruption, both magmas stored at 777–858°C, 87–197 MPa. There is not significant difference in P-T conditions. Ikezuki magma relatively depleted in H_2O content than Shimoyamazato.

The magmas of the Yanagisawa eruption were generated at P-T conditions of 790–838°C, 126–157 MPa. Yanagisawa magmas formed by rejuvenation of crustal mush zone due to the injection of hotter primitive magmas. This process was not accompanied by magma mixing, but only heat and volatiles were injected into the mush to form the Yanagisawa magmas. Mineral zoning in Yanagisawa phenocrysts reflects the multiple injections of hotter

magma below rhyolites that lead to thermal convection and remobilization of the resident magma. These conditions led to the formation of an association of phenocrysts with broad reverse zoning and did not provoke an eruption long enough to generate 10 km^3 of chemically homogeneous magma (given that the entire range between the two eruptions is 27 thousand years).

Thus, those observations suggest that rejuvenation processes of already existing magmas stored in the upper crust are critical in the preparation of large explosive eruptions in NE Honshu.

Chapter 4. Timescales of formation and mobilization of the silicic magma: insight from diffusion chronometry in orthopyroxene and quartz from Naruko and Onikobe deposits

4.1. Introduction

The textures, compositions, and thickness of growth zones in crystals can be used to distinguish the different magmatic processes responsible for zoning (Kahl et al., 2011; Saunders et al., 2012; Costa et al., 2020, 2021). Minerals can reveal details such as pressure, temperature, fO_2, and timescales of magmatic processes (e.g., Cashman et al., 2017; Cooper, 2019; Costa et al., 2020). Diffusion zoning, which occurs at the crystal boundary when the surrounding parameters change, can be used to estimate the equilibration time of this crystal during the transition from one ME to another. Thus, it is possible to estimate the timing of such processes as the movement of magmas from depth to shallower parts, mixing of magmas, remobilization of mush, and initiation of eruptions through mafic recharge. Diffusion chronometry, which is applied to such compositionally zoned crystals, provides important insights into pre-eruptive magmatic timescales (Costa et al., 2008; Dohmen et al., 2017; Costa et al., 2020; Costa, 2021; Sato et al., 2022; Elms et al., 2023). There can also be discrepancies in time scales estimated from different phases recording seemingly common processes (e.g., Chamberlain et al., 2014), so if zonality in crystals permits, it is important to consider time scales across multiple phases.

Understanding the timescales and processes through which magma bodies form and develop in the crust prior to eruption is vital for volcanic monitoring and interpreting future unrest signals, particularly at caldera volcanoes. Abundant reverse zoning in Yanagisawa tuffs suggest that rejuvenation process play a crucial role during magma formation. Thus, here, we present pre-eruptive timescales for the assembly of final melt-dominated eruptive bodies derived from Fe-Mg interdiffusion in orthopyroxene from Yanagisawa and Ti diffusion in quartz from the pumice of Yanagisawa and Shimoyamazato eruption. Here we consider only orthopyroxene from Yanagisawa, because it has abundant reverse zoning with diffusion nature, while orthopyroxenes from Ikezuki and Shimoyamazato are most likely normal zoned and zoning rather correspond to the crystal growth.

4.2. Methodology

Fe-Mg diffusion zones have a strong negative relationship with the greyscale value in BSE image (e.g., Allan et al., 2013; Cooper et al., 2017). In addition, greyscale profiles provide

a better spatial resolution than the EPMA spot analysis. Thus, high resolution BSE images of each crystal were taken to study crystal zonation features. Choosing the wrong crystallographic orientation of the crystal yields incorrect timescales (Costa et al., 2008). To obtain accurate results from diffusion modelling, I carefully selected only those crystals which cut parallel to the (010) based on the crystal shape and cleavage. All greyscale profiles were taken perpendicular to the crystal edge from BSE images using ImageJ software (Schneider et al., 2012; http://rsb.info.nih.gov/ij/). In each crystal, at least one profile was analysed by EPMA, traversing from core to edge, after which the composition was correlated with greyscale. For each crystal, the greyscale value was calibrated to the Mg# content with a R^2>0.95.

Diffusion time modelling suggests that initially, when P-T conditions changed around the crystal, its composition changed abruptly, and step-wise concentration gradients were formed. This gradient was changed over time by Fe-Mg interdiffusion, resulting in sigmoidal concentration gradients (Fig. 1.2; 4.1f). The assumption that the sigmoidal gradient is a result of diffusion only yields the maximum timescale.

Diffusion timescales were modelled in AUTODIFF spreadsheet, done by Dr. D. J. Morgan (Pers. comm., before published only as demo version for olivine (Couperthwaite et al., 2020). AUTODIFF is built around 1 D composition-dependent diffusion curves calculated using a finite difference method. A detailed description of the sequence of calculations and the AUTODIFF principle are described in (Couperthwaite et al., 2020).

Another important step in calculating the diffusion time is to choose the interdiffusion coefficient. For orthopyroxenes, there are two most used sets of coefficients proposed by (Dohmen et al., 2016) and (Ganguly and Tazzoli, 1994). (Dohmen et al., 2016) provided a new set of coefficients obtained in experiments using high-magnesium orthopyroxenes (En 91-98). These compositions are more likely to correspond to mantle orthopyroxenes and should be used with caution for shallow silicic magmas. Another set of coefficients was proposed by (Ganguly and Tazzoli, 1994), using pyroxenes close to the data of the present study and determined a more significant compositional dependence. For the calculating diffusion coefficient, it is also important to consider the oxygen fugacity, which determines the degree of iron oxidation. It has been suggested that the fO_2 dependence may have the same form as for olivine (Ganguly and Tazzoli, 1994). For oxygen fugacity, (Dohmen et al., 2016) suggest a much lower fugacity dependence than that found in olivine (exponent 1/6, e.g., Dohmen & Chakraborty, 2007), This result conflicts with the value of the oxygen fugacity relationship suggested by (Ganguly and Tazzoli, 1994) based on an analogy with olivine. Probably such correction for oxygen fugacity

can be correct for high-magnesian pyroxenes, however it remains unclear how it affects the results for less magnesian pyroxenes. Based on the above, we use (Ganguly and Tazzoli, 1994) equation but without the oxygen fugacity component as already done in the similar magmatic systems (e.g., Cooper et al., 2017).

$$\log_D(Fe-Mg)_{c-b} = -5.54 + 2.26X_{Fe} - \frac{12530}{T} \quad \text{(Equation 4.1)}$$

The only intensive parameter used for modeling in this case is temperature. Therefore, all modeled timescales have been calculated for a fixed temperature of 821°C (±33°C) for Yanagisawa based on Fe-Ti oxides thermometry as a more reliable temperature before the eruption (see paragraph 3.6.2. "P-T-*f*O parameters").

Quartz zoning patterns were observed by cathodoluminescence (CL) imaging. Its known that brightness (greyscale intensities) of the quartz CL image directly corresponds to Ti concentration (Wark et al. 2007). The observation conducted using SEM-CL, Hitachi S-3400N of Graduate School of Science, with 9 a working distance of 10 mm, an acceleration voltage of 20 kV, and a probe current of 90 μA. Grayscale profile were extracted from CL images using ImageJ software (Schneider et al., 2012; http://rsb.info.nih.gov/ij/), in the same manner as profiles in orthopyroxene. Diffusion was estimated using web-based software "Diffuser" (Wu, et al., 2022). Interdiffusion coefficient has been calculated using Arrhenius equation from (Cherniak et al., 2007) for the temperature ranges of 821°C (±33°C) in Yanagisawa case.

4.3. Results and implications of diffusion timescales from Yanagisawa orthopyroxene

The most common zoning in Yanagisawa orthopyroxene is reverse, where the rim is relatively broad (>40 microns) and always darker than the core. This zoning can be either single or multiple with a mantle broad dark zone. Evidence from the presence of mantle dark exterior zones in Yanagisawa orthopyroxene (e.g., Fig. 3.4 and 4.1) represent mixing with, or rejuvenation through interaction with, a less evolved and/or hotter melt (e.g., Chamberlain et al., 2014; Cooper et al., 2017; 2019). Based on Fe-Mg diffusion, this process occurred within 15-930 years (centuries are predominant). Usually, this boundary is enclosed in the crystal at a distance from the rim and is followed by a zone corresponding to the crystallization of the crystal and sometimes an outer narrow rim part with a diffusion boundary. Thus, we consider that the dark mantle zones correspond to the interaction of the hot less evolved magma through underplating at the base of the mush column, essentially primed a volume of material for

eruption through thermal rejuvenation and/or volatile exchange, rather than being the eruption trigger itself. The ubiquitous presence of such zoning patterns in Yanagisawa orthopyroxenes suggests that magmatic rejuvenation might have a system-wide influence. Also, we note, that small number of crystals finds with a normal zoning pattern (ME 2 En_{65-61} to ME 1 En_{54-60}) suggests that the mixing was limited.

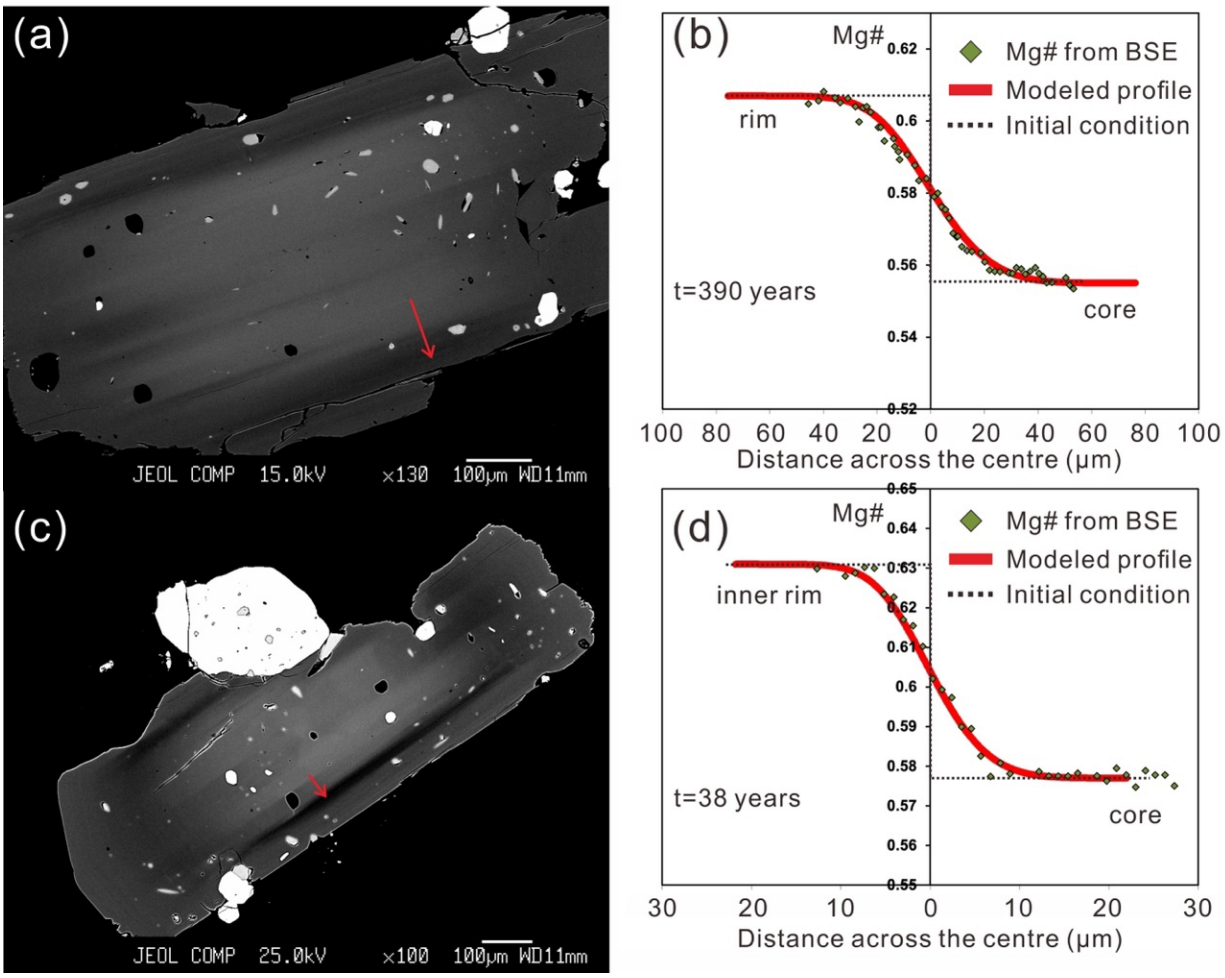

Figure 4.1. Diffusion timescale profile (b and d) through core to inner rim boundary in Yanagisawa orthopyroxene (a and c), respectively.

Outermost narrow dark zones at the crystal rim also correspond to episodes of interaction with, a less evolved and/or hotter melt. However, the position strictly at the rim on the contact with groundmass glass with no evidence of subsequent crystallization or re-equilibration implies that these episodes may be the trigger of an eruption. such zones are often observed in multizonal crystals, where there is a wide boundary between the nucleus and the inner edge and an outer banded zone (Fig. 4.2a-f). In the case of Yanagisawa orthopyroxene outermost dark rims yield 2-54 years.

Based on those results, we see that the inner broad boundaries in the crystals of both eruptions give longer periods of time, which apparently correspond to such processes as melting of crustal rocks and extraction of magmas from crystal-rich bodies into melt-rich shallower zones. The outer narrow zones may indicate much more rapid processes associated with the final mobilization and triggering of magma, which could have led to the eruptions.

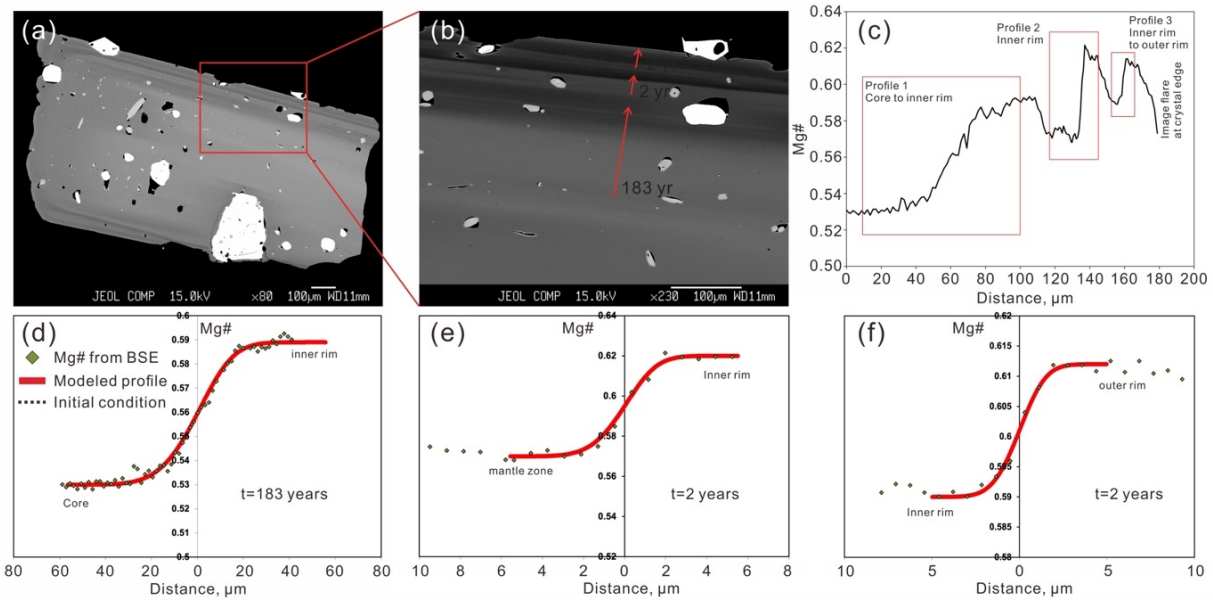

Figure 4.2. Yanagisawa multiple-zones orthopyroxene with thick border between core and inner rim and streaky outermost part (a-c); Modelled profiles (d), (e) and (f) correspond to the borders in the direction from core to the rim, respectively, which are indicated by red arrows in figure (b).

4.5. Textural characteristics and timescales of Shimoyamazato and Yanagisawa quartz

Here we consider quartz from Shimoyamazato (Onikobe) and Yanagisawa (Naruko) together to compare different zoning futures in the neighboring calderas.

In Shimoyamazato and Yanagisawa pumices, quartz forms euhedral, often bipyramidal, crystals up to ~2.0-2.5 mm. CL imaging of quartz reveals oscillatory and complexly zoned grains with the greyscale intensity inferred to reflect Ti composition (Wark et al., 2007; Matthews et al., 2012). Crystals from both eruptions have a multiple zoning pattern and abundant melt embayments. In the Table 4.1 we classified all observed crystals into three groups: (1) quartz with dark rims (low-Ti), (2) quartz with bright rims (high-Ti), and (3) grains with no significant contrast at the rim (Table 4.1).

Table 4.1. Summary of quartz textures based on CL intensities				
Deposit	Temperature, °C	Rim darker than core	Rim lighter than core	No signifficant change
Shimoyamazato (Onikobe)	796 ± 33	67 %	11 %	22 %
Yanagisawa (Naruko)	821 ± 33	3 %	65 %	32 %

Table 4.1. Statistical analysis of quartz textures based on CL images.

In Shimoyamazato quartz, crystals with bright (high-Ti) cores or without distinguishable CL zoning are abundant. Findings of crystals with a bright outer rim at the contact with the groundmass are extremely rare. Within a Shimoyamazato pumice, quartz with darker rims (low-Ti) dominate over those with lighter rims and serve as an evidence of an apparent temperature decrease prior to eruption. This is consistent with zoning observed in orthopyroxene and plagioclase from Shimoyamazato pumice. This down-temperature signal is interpreted as a movement of Shimoyamazato magma to a shallower storage level before caldera eruption.

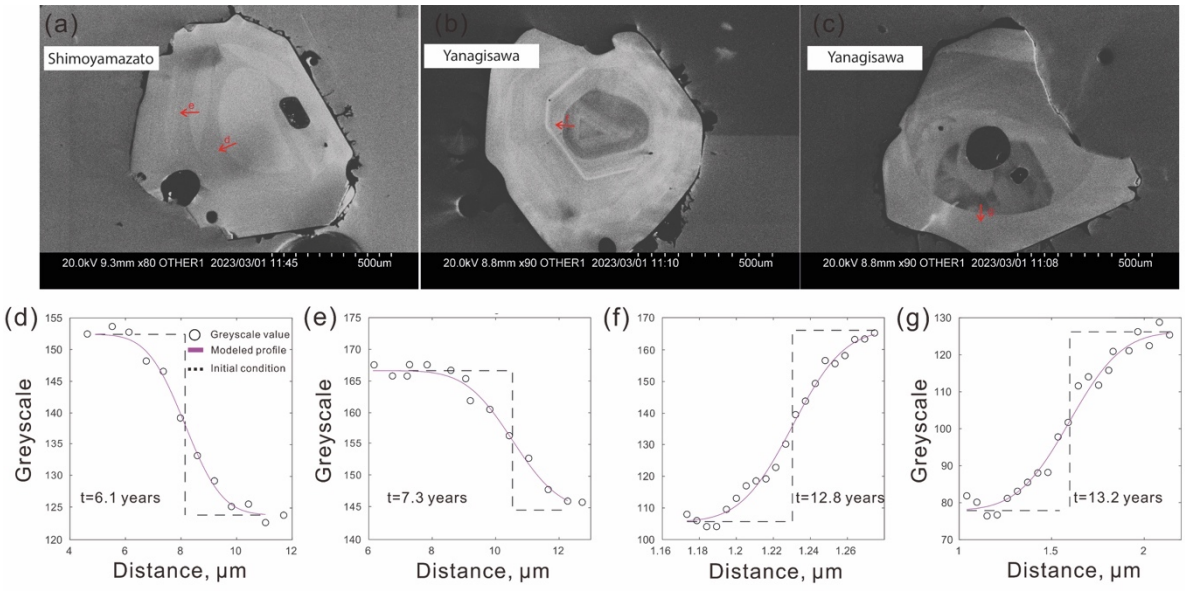

Figure 4.3. CL-images of Shimoyamazato quartz (a) and Yanagisawa (b, c). Red arrows indicated modelled border for Shimoyamazato quartz (d and e) and Yanagisawa (f and g).

Crystals with dark (low-Ti) cores predominate in Yanagisawa quartz, which agrees with the observed patterns in orthopyroxene (low-Mg cores and high-Mg rims). Also, distinct bright

rim zones (high-Ti) are sometimes observed in Yanagisawa quartz, which may indicate an increase in temperature shortly before the eruption.

The complexity of the zoning patterns did not allow for a distinctive zone common to all grains to be modelled and correspond magmatic environment and zone in quartz. Therefore, all zones with diffusive nature have been considered together. Titanium diffusion timescales across boundaries ranging from the core to the rim of Shimoyamazato quartz vary within 0.6-22 years of eruption. The ages increase from 22 years to a peak at ~3 years. Titanium timescales from Yanagisawa quartz vary within 0.2-21 years of eruption and are very similar to the Shimoyamazato timescales. The ages peak at ~1-3 years prior to eruption.

4.6. Conclusions

Orthopyroxene and quartz from the Shimoyamazato and Yanagisawa deposits contain evidence of the open-system processes before each caldera eruption.

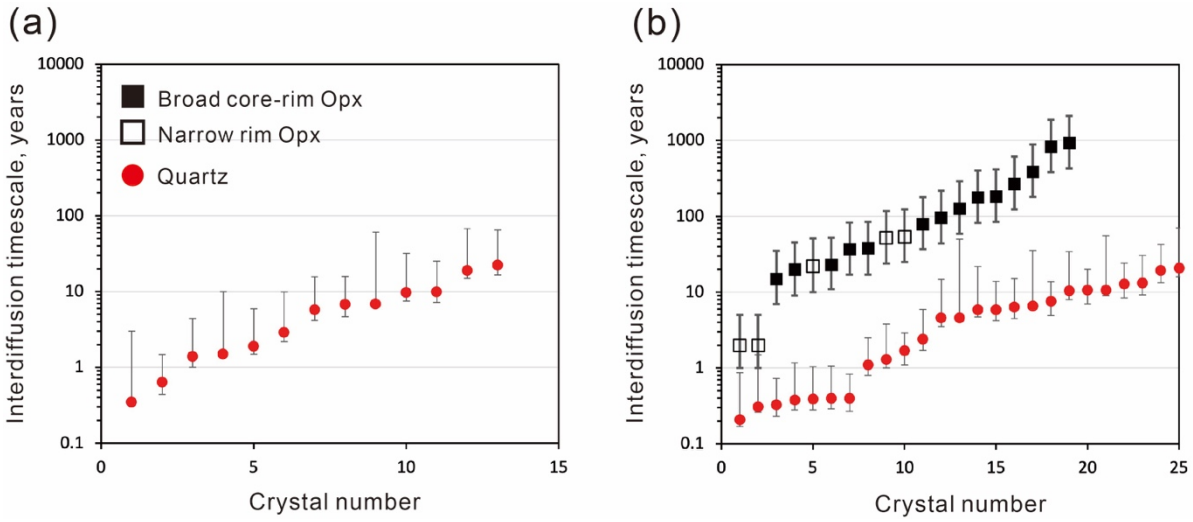

Figure 4.4. Summary plots of the model ages derived from diffusion profiles in (a) Shimoyamazato quartz and (b) Yanagisawa orthopyroxene and quartz, respectively.

In Yanagisawa magma, we observe strong evidence of the remobilization of the upper-crustal magma supported by widespread reverse zoning. Multiple reverse zoning predominantly on the orthopyroxene rims indicated the repetitive process of heating the Yanagisawa magmas shortly before the eruption. This process also occurred within centuries years, but this process was most prevalent only decades prior to eruption. Narrow dark rims suggest triggering of eruption through mafic recharge, which occurred within years-decades.

Zoning patterns within quartz from both eruptions are similar to those in orthopyroxene. Thus, quartz could have been present throughout the evolution of the Naruko magmas together

with orthopyroxene. Quartz from Shimoyamazato pumice presents a lighter (high-Ti) core than rim or absence of zoning. While Yanagisawa quartz usually have a reverse zoning pattern with significantly resorbed cores and often contains bright rims.

The timescales presented here are comparable to those representing the remobilisation and rejuvenation of voluminous siliceous magmas in the arc settings (e.g., Morgan et al., 2006; Saunders et al., 2010, Allan et al., 2013, Chamberlain et al., 2014; Cooper et al., 2017; Sato et al., 2022; Elms et al., 2023).

Based on the interpretation of mineral chemistry and zoning patterns, it can be inferred that several important processes govern the formation and behavior of melt bodies in the crust. These processes include melt segregation, magma body assembly from the source mush, and the residence of magma in the upper crust. The timeline for these processes spans from a few decades up to thousands of years. Notably, priming events, such as heating caused by basaltic injection, appear to occur in the years leading up to the main eruption (e.g. rims in orthopyroxene from Yanagisawa or Quartz zoning).

These findings emphasize the complexity of the processes involved in the formation and movement of melt bodies within the crust. They suggest that the assembly and residence of magma can take considerable time, ranging from decades to millennia. Additionally, the occurrence of priming events preceding major eruptions highlights the potential significance of short-term processes in influencing volcanic activity.

The study also underscores the importance of considering multiple timescales when studying magmatic processes. While some processes may occur over longer periods, others can have more immediate effects, impacting the behavior of magma reservoirs and influencing volcanic monitoring initiatives. Overall, this research provides valuable insights into the dynamics of magma within the crust and offers implications for geophysical imaging of magma reservoirs and volcanic monitoring efforts. Understanding the various timescales of magmatic processes is crucial for accurately assessing volcanic hazards and enhancing our knowledge of volcanic behavior.

Chapter 5. Water excess and fluid accumulation during the formation of the silicious magma in the upper crust.

5.1. Introduction

Formation of any shallow magma chamber related to the crystallization of mantle-derived less evolved magma. The extensive crystallization of basalt may supply a vastly excessive amount of magmatic volatile components to an overlying felsic magma chamber. But water dissolved in the parental mantle-derived magmas cannot be completely dissolved in the felsic endmember magmas dislocated in shallow conditions due to the limited solubility of volatiles. Thus, volatiles excess exists. That undissolved water migrated upward and forms potential geothermal reservoirs. Using a petrological approach, it is going to clarify the bulk composition of the parent and terminal rocks and the P-T-fO conditions of their storage, as well as the water content in the melt inclusions of both terminal members. Using these data, we conduct simulations in Rhyolite-Melts software to estimate the degree of crystallization of the parental melt to form the final shallow reservoir and the mass of water that is (1) dissolved in the final reservoir and (2) water that has not melted and turned into fluid. Therefore, the amount of separated fluid can be estimated.

5.2. Water excess during equilibrium crystallization. Rhyolite-Melts modelling for Naruko magma.

In an attempt to estimate the aqueous outcome in the formation of silicic magmas by crystallizing less primitive magmas, we using Naruko magmas as an natural example. These magmas did not form in this way, however, here I consider an exclusively theoretical scenario that can also be applied to any other volcanic center where the compositions of endmember magmas and the conditions of their generation are known. This approach has already been successfully applied to some silicic magmas in NE Honshu, such as Kutcharo-Mashu system (Miyagi et al., 2012) or Kakkonda granite (Miyagi, 2022).

We applied Rhyolite-Melts (Gualda et al. 2012; Asimow and Ghiorso, 1998; Ghiorso and Sack, 1995) modeling for the equilibrium batch crystallization of the most primitive known rock from Naruko volcano. The most primitive composition of the mafic inclusions in modern Naruko lavas (basaltic andesite) described in sample (Ban et al., 2005, Sample TR-4) was taken as the starting composition. By using this composition, because no more primitive rocks are known from Naruko volcano, the basaltic andesite should correspond to the already slightly differentiated magmas. Two main modeling aims are: (1) to check the possibility/impossibility

of producing Naruko rhyolites from primitive magmas and their possible affinity; and (2) to assess the degree of fractional crystallization and the volume of differentiated primitive magmas that produced rhyolite.

The simulations used the same approach (Miyagi et al., 2012; Miyagi et al., 2017). The ranges of pressures, temperatures, oxygen fugacity, H_2O, and CO_2 concentrations are 0–800 MPa in 10 MPa steps, 700°C to 1400°C in 1°C steps, FMQ −1 to FMQ + 3 log-units, 0–8.0 wt% H_2O in 0.2 wt% steps, and 0.001, 0.010, 0.001 wt% CO_2, respectively. The total number of combinations of these different parameters is approximately 3.36 million.

Of all the results obtained, we selected only those where the oxygen fugacity was set as FMQ+2 (based on data from Ban et al., 2005), and CO_2 content was taken as 0.001 wt% (because rhyolite is CO_2-poor). The total water content and pressure were manually selected so that the residual melt successfully reproduced the composition of Naruko rhyolites.

The scenario that most successfully reproduces Naruko rhyolites for all parameters (e.g., H_2O=4.9 wt. % (average in MIs), T = 810–820 ºC) selected by combining different scenarios and suppose parameters of 150 MPa; H_2O=4.2 wt. %, CO_2=0.001 wt. % in parental magma. Such a scenario suggests producing Naruko rhyolites through 70 percent crystallization of the starting composition. Rhyolite-MELTS modeling with lower initial water concentrations can also yield Naruko rhyolites. However, the crystallization percentages of the initial basalt become considerably high (>85%), which is an unrealistic scenario because producing large volumes of caldera-forming magmas (12.5 km^3) require too much initial melt. At the same time, the water content of 4.2 wt. % in the initial primitive magma is typical for Honshu (Ushioda et al., 2014 and references therein). In (Fig. 5.1a-f), we show the best-fit crystallization pathways of the most primitive mafic inclusion sample (TR-4) under 150 MPa pressure and 300 MPa for comparison.

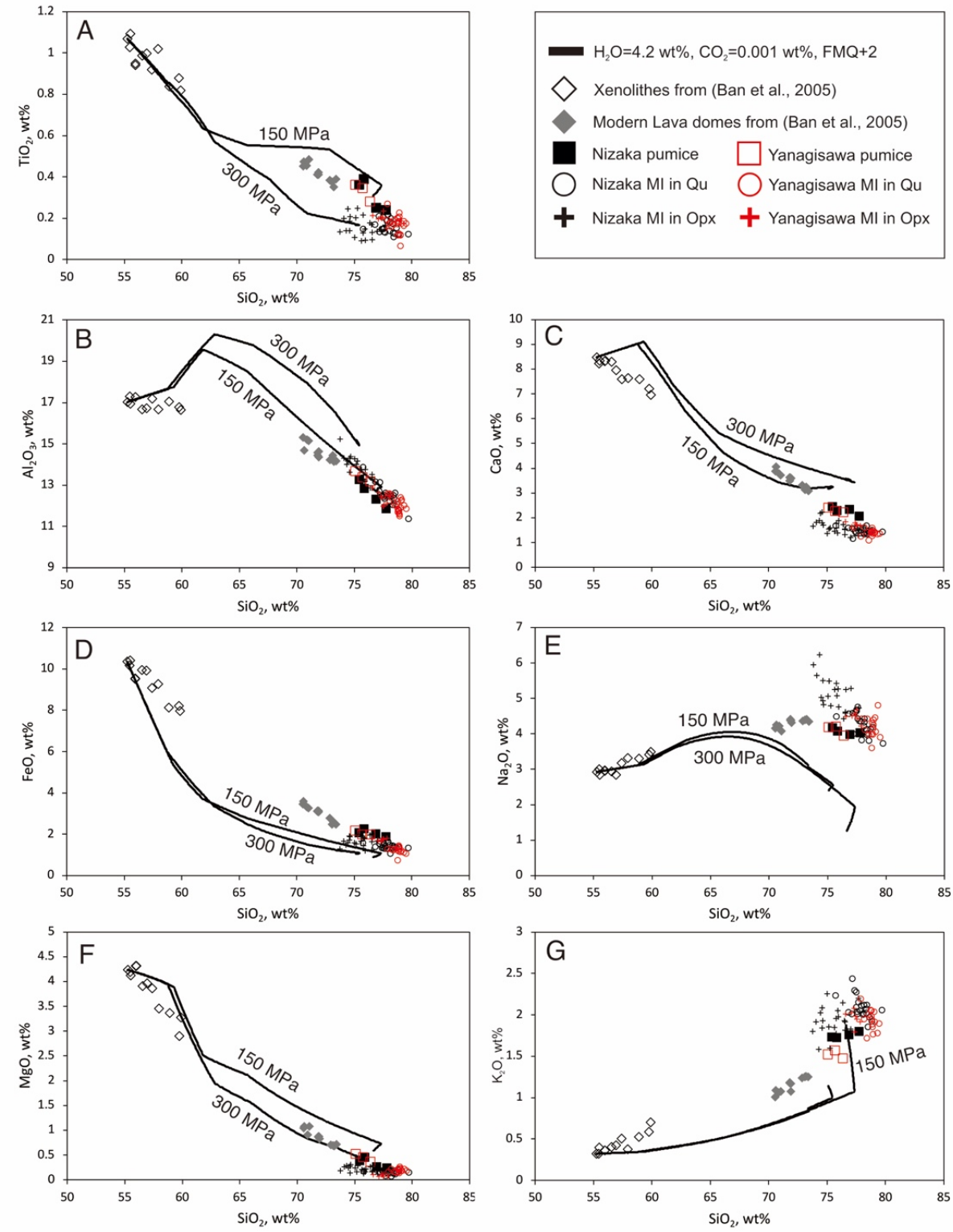

Figure 5.1. Variation diagrams showing bulk rock data, melt inclusion data and melt compositions estimated using the Rhyolite-Melts software. Data are volatile-free, normalized to 100%. All Fe as FeO. Two lines for 150 and 300 MPa modeling, respectively, are shown for comparison.

Another significant value of the Rhyolite-Melts simulation we applied is our attempt to discuss the excess water that can be released during the crystallization of basalt to rhyolite.

Crystallization of basalt may supply excessive amounts of volatile magmatic components to the overlying felsic magmatic bodies. However, the newly generated rhyolite cannot dissolve all of the volatile components contained in the parental magma because the concentration of volatiles in the melt is limited by pressure-dependent solubility. Thus, while petrogenic elements are entirely distributed between the restite and the more evolved melt, volatiles cannot dissolve in any magmatic phases significantly, leading to their separation and degassing with the concomitant formation of geothermal deposits and ore halos (Richards, 2011). Rhyolite-Melts results suggest the formation of Naruko rhyolites during isobaric cooling and crystallization of basalts in a magma storage area (or roughly near) and release of fluid due to the "second boiling" process (e.g., Candela, 1997)

As the most suitable scenario is the reproduction of the Naruko rhyolites through 70 percent crystallization of basaltic andesite, we can estimate the mass of the original parent magma using a simple mass-balance calculation. We use the known volume of erupted Naruko material (12.5 km^3 DRE) and a magma density of 2223 kg/m^3, calculated using densityX software (Iacovino and Till, 2019). The calculated mass of the required parental melt at 70% crystallization is 92 gigatons ($1Gt=10^{12}$ kg), equivalent to approximately 40 km^3 of magma and is a geologically realistic estimation. According to the best simulation scenario, the parental melt contains 4.2 wt% H_2O, equivalent to 3.86 Gt bulk water content in parental magma.

Using the averaged concentration of water in the Naruko rhyolite melt inclusions (4.9 wt.%) and the estimated mass of the Naruko rhyolites (28 Gt), we estimate the mass of dissolved water to be 1.36 Gt of water, which is equivalent to 35 wt.% of the original bulk water in the parental magma (as 1.36/3.86). Recently, Uno et al. (2017), based on mass balance calculation for the crust–melt reaction zones, suggested that the original >5.0–5.6 wt.% of H_2O within the arc magma is partitioned into ≤3.7 wt.% H_2O consumed by the hydration of local crustal material and ≥1.3–1.9 wt.% H_2O expelled to the overlying upper crust. These observations suggest that approximately 25% of initial water content in parental magma melts can be excess during intrusion and solidification of the granitic melts and subsequently transported to the overlying crust.

Thus, it is possible to estimate that approximately 2.5 Gt of water has not been dissolved in the rhyolitic end member. But it became excessive due to pressure limitation of water dissolution in the melt (Fig. 5.2). This estimate can be used as a maximum because of no consideration of the contamination by crustal rocks, which could have melted and contributed

volatiles to the newly formed rhyolites. Additional studies are required to account for the contribution of this process.

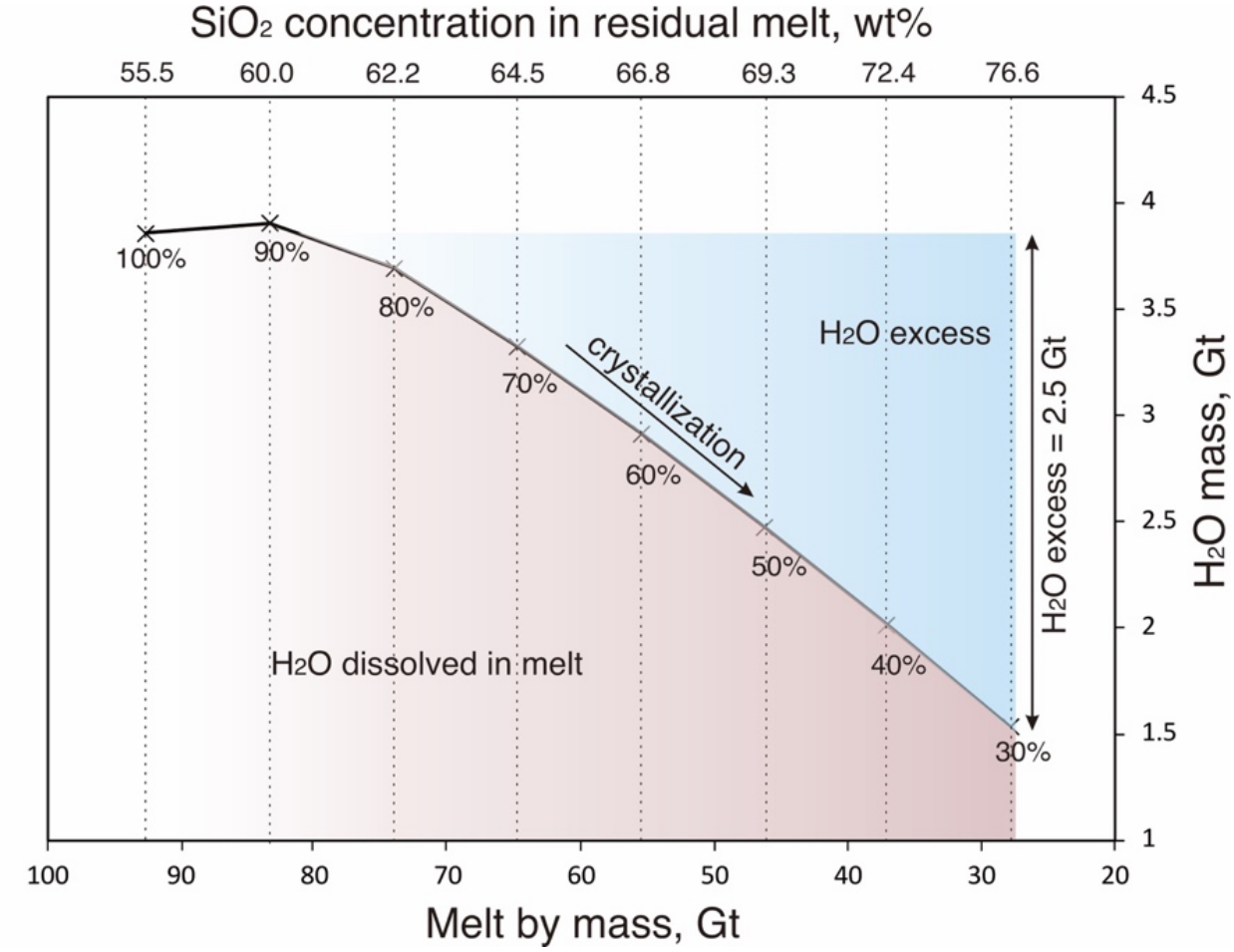

Figure 5.2. Crystallization result of andesite-basalt Naruko in Rhyolite-MELTS at a constant pressure of 150 MPa, fO_2 of FMQ+2, initial H_2O=4.2 wt% and CO_2=0.001 wt%. The blue field shows the mass of water that was not dissolved in the final residual melt due to pressure solubility limitation. The red field corresponds to the mass of dissolved water in the residual melt. The upper abscissa axis shows the SiO_2 concentrations in the residual melt calculated on a volatile-free basis and normalized to 100%. All Fe as FeO.

5.3. Water excess during partial melting. Case study of Mendeleev caldera.

A significant portion of the lower arc crust may be amphibole- or mica-rich in composition and without a free fluid phase (e.g., Rushmer, 1991). Partial melting of these rock may be responsible for the formation of arc dacites. Mendeleev dacites formed through dehydration partial melting in relatively shallow crustal conditions (<12 km). In an attempt to determine water excess during the formation of dacites, the case of Mendeleev magmas was considered as a natural example.

Partial melting can be fluid-saturated, fluid-absent, or fluid-assisted (fluid presents but below saturation) (e.g., Beard & Lofgren, 1991; Li et al., 2022). The presence or absence of fluid saturation during melting of amphibole-bearing rocks produces different melts and cause of the stabilization of minerals of different compositions. As previous description in Chapter 2, Mendeleev melts are rather formed in the absence of fluid (dehydration melting). Dehydration melting experiments (Beard & Lofgren, 1991) have the most similar final compositions to Mendeleev's, which are reproduced at realistic low pressures and temperatures. That process does not produce a free fluid that could separate due to limited solubility. To illustrate this, we consider results of (Beard & Lofgren, 1991) on dehydration melting experiments as an example (Fig. 5.3)

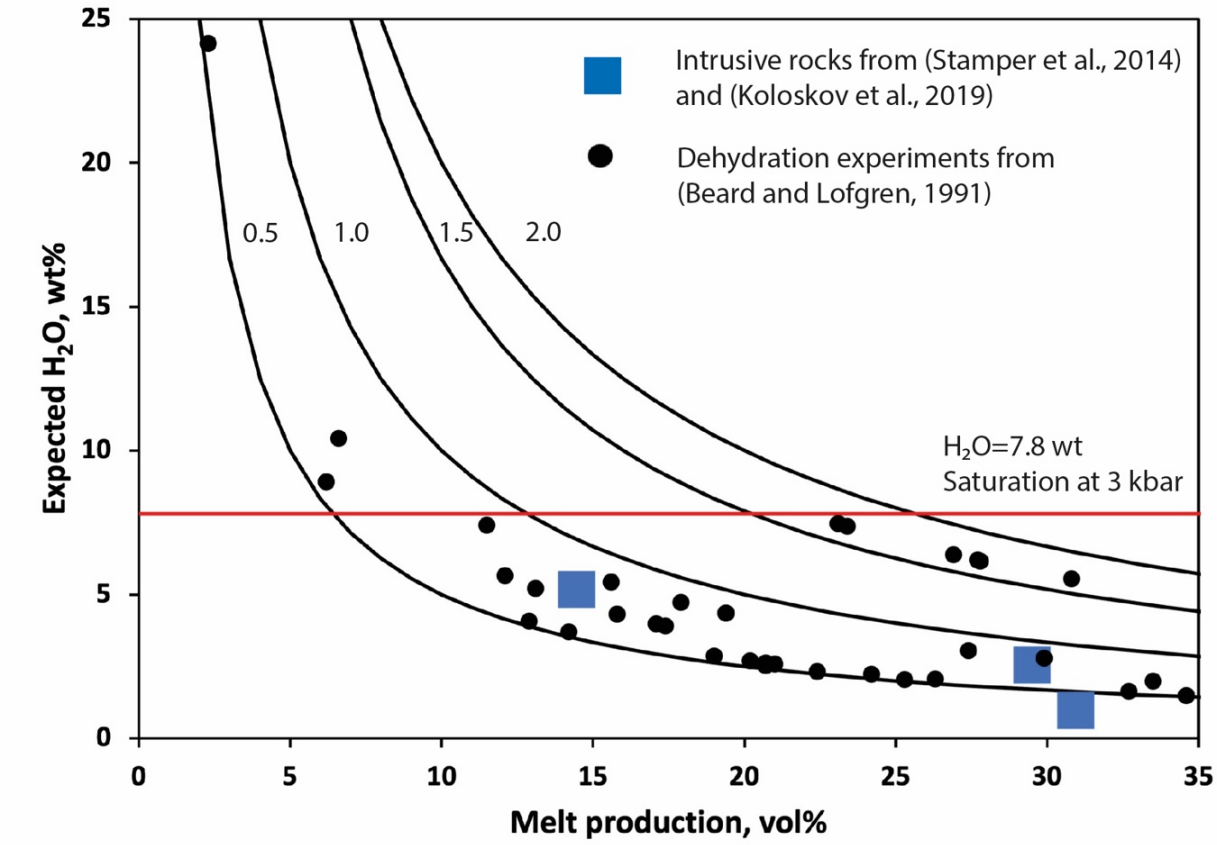

Figure 5.3. Results of dehydration melting experiments from (Beard and Lofgren, 1991). Isoplets indicate the water content of the amphibole-bearing source that is being melted. For example, melting of pure hornblende with 2 wt% water content will produce melts along isopleth 2.0. Here we do not consider situations where a substrate with more than 2 wt% water content melts because the geochemistry of the Mendeleev dacites and the absence of findings of other water minerals besides amphibole indicates that the main water-bearing phase is amphibole only. The expected amount of water is the content that should be in the experimental melt obtained, assuming that all the water from the source has dissolved into it. The red line shows the water saturation limit for Mendeleev melts at 3 kbar (calculated using VolatileCalc by Newman & Lowenstern, 2002). Blue squares – natural intrusive rocks. See text for details

Figure 5.3 shows the dehydration melting results from (Beard & Lofgren, 1991). The melt portion is taken from (Beard & Lofgren, 1991). The expected water content is calculated as $M_{H2O\ expected} = M_{H2O\ source} * \Delta M_{melt}$, where is ΔM_{melt} – mass portion of the melt in the experiment. Several natural intrusive samples were taken for comparison: amphibolite from Grenada Island (Stamper et al., 2014, sample GR-42) and amphibolite and gabbro from Shikotan Island (Koloskov et al., 2019, Samples 11 and 12). The bulk water content of these rocks was calculated based on the assumption that amphibole is the only water-bearing phase with an H_2O concentration=2.0 wt.%. The melt mass to be produced by the complete melting of these rocks was calculated using the GeoBalance mass balance calculation program, which is written with Visual Basic for Applications (VBA) and built in a macro-enabled Excel worksheet (Li et al., 2020). The working algorithm is based on solving the least square problem using pseudo-inverse of matrix and singular value decomposition (SVD) of matrix. During the calculation, the program reproduces a realistic mineral assemblage and phase proportions consistent with those observed in the Mendeleev pumice and in experiments (Beard and Lofgren, 1991). The red line illustrates the water solubility for Mendeleev melts at 3 kbar (using VolatileCalc 2.0; Newman & Lowenster, 2002), which is the maximum expected solubility for Mendeleev magmas. with rare exceptions, all points fall in the field below the saturation line at 3 kbar, which means that the produced melts are undersaturated with water. These results indicate that the generation of rhyolitic peritectic melts during the partial melting of amphibole-bearing rocks in the Kunashir crust rather does not produce an excess of aqueous fluid per se (fluid absent).

However, as was shown above, Mendeleev magmas are water-saturated before eruption. Thus, we expect an excess of aqueous fluid during the formation of the Mendeleev magma body; however, this occurs not during the partial melting of crustal rocks, but during their ascent from the place of generation to the storage place in the shallower part. In an attempt to estimate water excess, we model this process through Rhyolite-Melts (Gualda et al. 2012; Asimow & Ghiorso, 1998; Ghiorso and Sack, 1995). The concept is summarized in (Fig. 5.4a) For the starting composition, we take the less-evolved composition of rhyolitic melt inclusion observed in the clinopyroxene core, which contains relicts of melted amphibole. The maximum generation pressure of these melts according to the data is 3 kbar, which corresponds to the lower crust of Kunashir Island. The solubility limit at this pressure is 7.8 wt% H_2O (Newman & Lowenstern, 2002). The minimum water content of the Mendeleev MIs is about 4 wt.%.

Thus, it assumes scenarios with initial water content of 4.0 - 7.8 wt% H_2O without CO_2, as its value is considered negligible.

The basic concept is crystallized obtained rhyolite melt at the amphibole melting point at 950 °C and 300 MPa and crystallize it to the conditions at which the magma was stored immediately before eruption. Proceeding from the fact that Mendeleev's dacites contain no more than 1 vol % of quartz, we perform crystallization until the appearance of the first quartz. From the analyzed MIs in quartz, we know that the water saturation pressure for these melts is 77-116 MPa. The homogenization temperature of melt inclusions in quartz is 825-832 °C at atmospheric pressure, which should be close to the crystallization temperature of the quartz itself (Rhoeder, 1984). These parameters restrict the final P-T conditions at which crystallization should stopped. Crystallization is carried out under dynamically changing pressure and temperature. Two DP/DT gradients of 16.6 (cooler) and 20 (hotter) are used to conduct this simulation. Crystallization of Rhyolite-Melts at these parameters is mainly controlled by plagioclase, which fully consistent with our proposed two-step model of formation of Mendeleev magmas (1. partial melting and 2. late crystallization of plagioclase and quartz).

The results show that the final melts similar to the glass of the bulk of the Mendeleev pumice are formed after 14-36% crystallization of the initial melt. At the same time, water saturation is observed in all scenarios. Based on the phase proportions in the Mendeleev samples (Table S2.2), we calculate the mass of melt. The density calculated using densityX software (Iacovino & Till, 2019). The mass of the rhyolite melts in erupted Mendeleev magma estimated to be 94-101 Gt (The range is determined by differences in the modal compositions of the pumice See Table S2.2). In this case, based on the range of measured water contents in melt inclusions (4-6 wt%), we estimate the mass of water in the final shallow reservoir to be in the range of 3.8-5.7 Gt (Mean is 4.82 Gt). The variation in water excess is almost identical for both crystallization scenarios and is determined more by the initial concentration. At DP/DT=20, the excess water is 1.57-5.32 Gt (24-52% of initial mass); at DP/DT=16.6, the excess is 1.03-5.34 Gt (18-53% of initial mass).

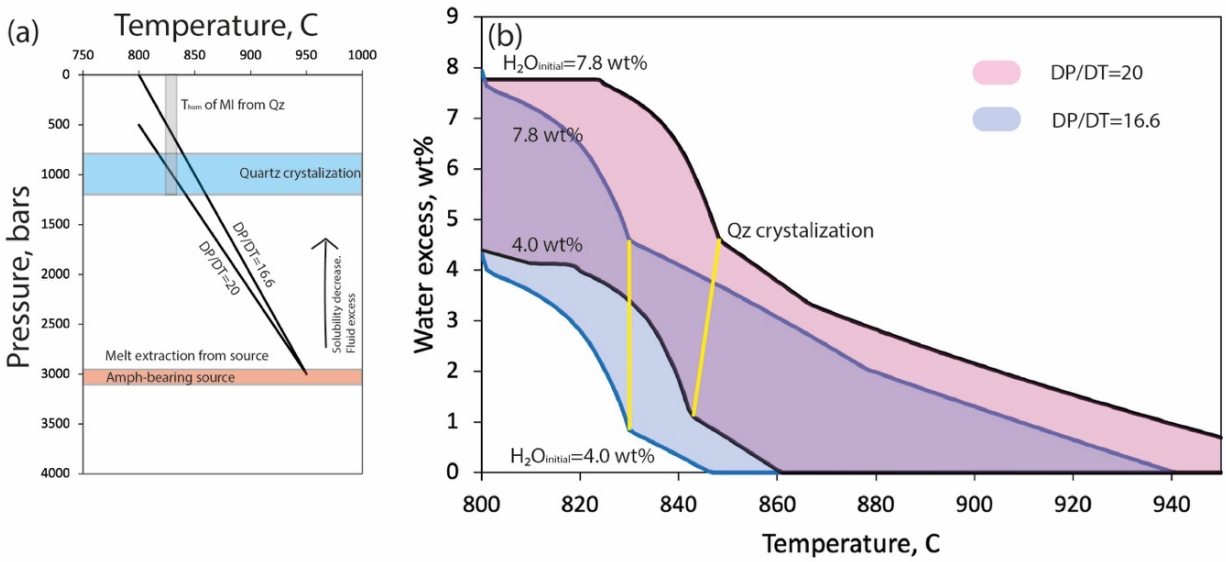

Figure 5.4. (a) Concept of Rhyolite-Melts modelling for Mendeleev magma case. Orange field correspond to the maximum estimated pressure based on the amphibole relics and considering here as a possible place of partial melt extraction. Blue area corresponds to the range of saturation pressure for MIs from quartz based on volatile content (using VolatileCalc 2.0, Newman & Lowenstern, 2002). Grey field correspond to the range of homogenization temperatures of MIs from quartz, that expected to be close to quartz crystallization temperature. Black lines correspond to the crystallization pathways in Rhyolite-Melts with DP/DT=16.6 and 20 respectively. Figure (b) present results of Rhyolite-Melts simulation, where is Y-axis is total water excess in wt.% of magma. Yellow lines highlighted points where first quartz crystalize in all scenarios.

5.4. Conclusion

On the basis of hypothesis that Naruko magma originated through simple batch crystallization of the basaltic andesite (the most primitive sample from the Naruko volcano), Rhyolite-Melts modeling results suggest that the Naruko rhyolites can be obtained by 70% crystallization of parental melts with initial concentrations of H_2O=4.2 wt. %, CO_2=0.001 wt. % and at a pressure of 1.5 kilobars. Based on the Rhyolite-Melts results and mass balance calculation, we estimated the mass of water that could be dissolved in the parental magma in the final Naruko rhyolite and the part that was not dissolved in the final rhyolite and probably was separated as a free fluid. We estimate that the parental melt contained 3.86 Gt bulk water content when the final rhyolite dissolved only 1.36 Gt. Thus, approximately 2.5 Gt of water (65 wt.%) has not been dissolved in the rhyolitic endmember but became excessive due to pressure limitation of water dissolution in the melt.

For Mendeleev volcano, a realistic scenario where water-unsaturated melts are separated from the source at 3 kbar and accumulated in a shallow chamber at pressures and temperatures corresponding to quartz crystallization. In this case, water saturation occurs not during generation of melts at the source, but during their uprising and degassing. In the pre-eruptive

melt was dissolved 3.8-5.7 Gt (Mean is 4.82 Gt) of water. During the uprising of melt from the source to the pre-eruptive magma body, degassing occurred and provide water excess of 1.03-5.34 Gt (18-53 wt.% of initial mass).

In both considered cases, the amount of released water is comparable to the amount which is dissolved in the final pre-eruptive melt (in terms of orders). Moreover, these calculations are in complete agreement with other similar studies (e.g., Uno et al., 2017; Miyagi, 2022).

Chapter 6. Conclusion

I have described in detail the petrology of three Pleistocene silicic calderas: Onikobe (Ikezuki and Shimoyamazato tuffs), Naruko (Yanagisawa tuffs) located in NE Honshu and Mendeleev caldera (Kunashir Island).

The 40 ka Mendeleev caldera eruption on Kunashir Island, southern Kurils, shows that the eruption involved a low-K dacitic magma, which is typical of southern Kuril calderas. Pre-eruptive temperatures of magma crystallization vary within 830–890 °C. Pre-eruptive magma of this eruption stored upper-crustal conditions at pressures ranging from 77 to 195 MPa and at an oxygen fugacity of 0.85–1.05 above the NNO buffer. Formation of this magma occurred due to the partial melting of amphibole-bearing source at the depth no less than 12.3km. A detailed analysis of pumice mineralogy revealed that the early 'gabbro-noritic' assemblage represented by plagioclase + augite + hypersthene + Fe–Ti oxides crystallized owing to Mg-hornblende dehydration breakdown. Taking into account the rhyolitic compositions of the primary melt inclusions in these minerals, we consider that their occurrence is related to dehydration partial melting that accompanied magma generation. The absence of mineral zoning and melt-inclusion compositions that would point to precursor mafic or intermediate parental melts indicates that the partial melting was the major mechanism of felsic magma generation for the 40 ka Mendeleev caldera eruption. This magma was composed of rhyolitic melt mixed with mafic products of the amphibole breakdown reaction, which together resulted in a magma with dacitic composition. During the latest stages of magmatic evolution, minor amounts of plagioclase and quartz crystallized directly from the residual rhyolitic melt, which ascend from source region to the shallower part of 3.0–4.5 km depth.

The "mafic" clots in the Ikezuki magma indicate a significant influence of more primitive magmas. But it remains unclear whether this was partial melting of more primitive crustal rocks or whether the mafic assemblages are xenoliths from the parental melt, the crystallization of which led to the formation of Ikezuki dacites. Detailed observation of the distribution of mineral zoning patterns allows us to suggest that the most probable mechanism of Shimoyamazato magmas is the rejuvenation of Ikezuki magmas due to the strong influence of hotter magmas, and further migration the colder reservoir. Thus, magmas of both eruptions were distinct. The process was not accompanied by significant mixing and hybridization of newly formed magmas. Before the eruption, both magmas stored at 777–858°C, 87–197 Mpa at the similar conditions.

Yanagisawa magmas were generated at close P-T conditions: 790–838°C, 126–157 MPa. Yanagisawa magmas formed by rejuvenation of crustal mush due to the injection of hotter primitive magmas. However, this process rather did not lead to the migration of heated portions to shallower part, as there is no evidence such as broad outermost zones with lower-Mg or lower-Ca content. That is, the erupted Yanagisawa magma was formed in situ and did not migrate far from place of its generation. The presence of streaky outermost zones with multiple zoning suggests that the same magma portions could have been heated many times. Probably, this is evidence of the growth of the magmatic chamber directly from the crystal mush without segregation of mobile portions to the shallower part.

By fitting of diffusion profiles in orthopyroxene and quartz from the Naruko eruptions, time duration of the magma formation processes could be estimated. Timescales modelled across Yanagisawa inner boundaries suggest that formation of magma occurred within within 15-930 years, while outermost dark rims yield 2-54 years. Titanium timescales from Yanagisawa quartz vary within 4-21 years of eruption. The ages peak at ~5 years prior to eruption. Results for both magmas show that the processes of mobilization formation and magma extraction from the source (whether crustal rock melting or extraction from mush zones) take place over timescales ranging from decades to millennia. At the same time, the processes that can lead to an eruption (triggers) occur very quickly in the years or decades before the eruption.

To estimate water flux within upper crust during the formation of silicic magma bodies, Rhyolite-melts modelling was applied. On the basis of a hypothesis that Naruko magma originated through simple batch crystallization of the basaltic andesite (the most primitive sample from the Naruko volcano)., Rhyolite-Melts modeling results suggest that the Naruko rhyolites can be obtained by 70% crystallization of basaltic andesite with initial concentrations of H_2O=4.2 wt. %, CO_2=0.001 wt. % and at a pressure of 1.5 kilobars. Based on the Rhyolite-Melts results and mass balance calculation, the mass of water that could be dissolved in the parental magma in the final Naruko rhyolite and the part that was not dissolved in the final rhyolite and probably was separated as a free fluid. The parental melt contained 3.86 Gt bulk water content when the final rhyolite dissolved only 1.36 Gt. Thus, approximately 2.5 Gt of water (65 wt.%) has not been dissolved in the rhyolitic endmember but became excessive due to pressure limitation of water dissolution in the melt.

For Mendeleev volcano, I considered the realistic scenario where water-unsaturated melts are separated from the source at 3 kbar and accumulated in a shallow chamber at pressures

and temperatures corresponding to the beginning of quartz crystallization. In this case, water saturation occurs not during generation of melts at the source, but during their uprising and degassing. In the pre-eruptive melt was dissolved 3.8-5.7 Gt (Mean is 4.82 Gt) of water. During the uprising of melt from the source to the pre-eruptive magma body, degassing occurred and provide water excess of 1.03-5.34 Gt (18-53 wt% of initial mass). In both considered cases, the amount of released water is comparable to the amount which is dissolved in the final pre-eruptive melt (in terms of orders).

Analytical methods

Whole-rock analyses (XRF and ICP-MS)

Major- and trace-element compositions of the pumice rocks from Mendeleev volcano were determined by X-ray fluorescence (XRF) analyzes using a Thermo Fisher ARL-9900 XL instrument and by inductively coupled plasma–mass spectrometry (ICP–MS) using a Finnigan Element-2 mass spectrometer at the Center for Multielement and Isotopic Study of the Institute of Geology and Mineralogy, Siberian Branch of the Russian Academy of Science, Novosibirsk, Russia. Loss on ignition for XRF analyses was determined by heating rock powder in a dry furnace at 950 °C in the air atmosphere for 2 h.

Whole-rock major and minor element composition for Onikobe and Naruko were obtained using WDS X-ray (Rigaku 25X Primus IV) and ED–XRF (PANalytical Epsilon 5)) spectrometers at Tohoku University, Sendai, Japan. For the WDXRF analyses of major elements, samples were prepared using the glass disk method. Six grams of rock powder for each sample were heated at 105 °C for 2 h to remove moisture. Glass disks were prepared using a mixture of 5.4 g of flux (a mixture of $LiBO_2$ 49.5%, $Li_2B_4O_7$ 49.5%, and LiBr 1%) and 0.6 g of each heated sample in a muffle furnace at 1050 °C. The glass disk was irradiated using X-rays from an Rh anode tube with 75 kV acceleration voltage and 8 mA beam current. Loss on ignition (LOI) values were estimated by keeping the samples at 950 °C for 2 h.

For EDXRF analyses, samples were prepared using the powder pellet method for minor elements. A polyvinyl chlorite ring sample holder 3 cm in diameter and 0.5 cm thick was used to make the pellet. Each pellet was pressed at 150 MPa and ≥ 200 MPa for 5 min for each press (Yamasaki, 2018). An acceleration of voltage 75 kV and a beam current of 8 mA were used to measure V, Cr, Co, Ni, Cu, and Zn, whereas Rb, Sr, Y, and Zr were determined using an acceleration voltage of 100 kV and a beam current of 6 mA. The standard samples used for the WDXRF and the EDXRF measurements were from the GSJ Igneous Rock Series and 26 geological and environmental standard reference materials (Yamasaki et al., 2018).

Mineral chemistry (EPMA)

Identification of growth zoning in single phenocrysts and analysis of glomerophyric cluster textures in Mendeleev mineral assemblage were carried out in carbon-coated epoxy pellets and thin sections by EDS scanning electron microscopy (SEM) using a TESCAN MIRA-3 LMU field-emission electron microscope at the Center for Multielement and Isotopic Study of the Institute of Geology and Mineralogy SB RAS. Major-element compositions for mineral

identification were obtained by energy-dispersive spectrometry using an Oxford Instruments X-Max 80 detector. The spectra were processed using INCA Energy 450+ software. Samples were measured using an accelerating voltage of 20 keV and a beam current of 1 nA.

Precise mineral compositions for Onikobe, Naruko and Mendeleev calderas were determined using an WDS electron microprobe analyzer (EPMA; JEOL JXA-8200) at the Graduate School of Environmental Studies, Tohoku University, Japan. For all mineral analyses, we used an accelerating voltage of 15 kV, a beam current of 12 nA, and a focused electron beam size of <1 μm. Natural and synthetic standards were used for calibration (wollastonite for Ca and Si, corundum for Al, rutile for Ti, eskolaite for Cr, hematite for Fe, manganosite for Mn, periclase for Mg, albite for Na, potassium feldspar for K, and halite for Cl). The counting times for peaks and backgrounds were 10 and 5 s, respectively. Calibration precisions were assessed by conducting analyses on secondary standards using commercial mineral standard SPI #02753.

Melt inclusion chemistry (EPMA)

To obtain precise data on the compositions of melt inclusions and groundmass (GM) glass, we used multiple-beam conditions during single-spot EPMA analysis. Glass compositions were determined using an accelerating voltage of 15 kV and a defocused electron beam size of 10 μm. Major elements (Na, Ca, K, Si, and Al) were analyzed using a 4 nA beam current, which prevents extensive Na loss during hydrous silicate glass analysis (Morgan & London, 2005). Minor elements (Ti, Fe, Cr, Mn, Mg, and Cl) were analyzed at 20 nA to reach lower detection limits and better accuracies of measured contents. The counting times for peaks and backgrounds were 10 and 5 s, respectively for the major elements and 30 and 15 s for the minor elements. Calibration precisions were assessed by conducting analyses on secondary standards using Smithsonian microbeam standard glasses (Jarosewich et al., 1980).

Table A1. Summary of repeated analyses of a secondary standards by EPMA

EPMA (JEOL JXA-8200) at the Gradute School of Environmental Studies, Tohoku University, Japan												
	SiO_2, wt%	TiO_2, wt%	Al_2O_3, wt%	Cr_2O_3, wt%	FeO, wt%	MnO, wt%	MgO, wt%	CaO, wt%	Na_2O, wt%	K_2O. wt%	Cl, wt%	Total
Kaersutite												
Repeated analysis (average), N=10	39.91	5.17	12.44	na	12.33	0.17	12.67	11.46	2.51	1.13	na	97.78
1σ	0.26	0.24	0.17	-	0.33	0.03	0.31	0.15	0.06	0.05	-	
Reference value recommended for SPI#2753-29	40.09	5.04	12.36	na	12.23	0.18	12.55	11.56	2.44	1.17	na	97.60
Cr-Diopside												
Repeated analysis (average), N=7	54.69	0.10	na	0.61	1.29	na	17.32	25.64	0.39	na	na	100.05
1σ	0.39	0.02	-	0.09	0.08	-	0.20	0.12	0.10	-	-	
Reference value recommended for SPI#2753-16	54.59	0.10	na	0.50	1.39	na	17.14	25.50	0.44	na	na	99.66
Plagioclase												
Repeated analysis (average), N=12	54.29	0.10	28.75	na	0.43	na	0.10	11.92	4.34	0.37	na	100.31
1σ	0.43	0.04	0.17	-	0.05	-	0.05	0.18	0.09	0.02	-	
Reference value recommended for SPI#2753-35	54.21	0.07	28.53	na	0.37	na	0.13	11.80	4.35	0.41	na	99.87
Rhyolitic glass VG-568												
Repeated analysis (average), N=12	76.59	0.09	12.13	na	1.16	0.027	0.03	0.51	3.64	4.74	0.10	99.02
1σ	0.31	0.004	0.14	-	0.09	0.005	0.01	0.06	0.11	0.09	0.02	
Reference value recommended for Rhyolitic glass USNM 72884 VG-568 from (Jarosewich et al., 1980)[1]	76.71	0.12	12.06	na	1.23	0.03	<0.1	0.5	3.75	4.89	0.13	99.42

Notes: bdl - below detection limit; n.a.=not analyzed

1. Jarosewich, E., Nelen, J.A. & Norberg, J.A. (1980). Reference Samples for Electron Microprobe Analysis. Geostandart Newsletters 4, 43–47.

Volatile elements (SIMS)

Contents of H_2O, CO_2, S, F, C, and P were measured by secondary ion mass spectrometry (SIMS) using a IMS-1280HR instrument (CAMECA, France) at the Kochi Institute for Core Sample Research, JAMSTEC. SIMS analyses were performed before EPMA to avoid carbon contamination (Rose-Koga et al., 2021). A 20 keV (10 keV at the ion source and 10 keV at the sample surface) 300–500 pA Cs+ ion beam was defocused onto a 10 μm^2 area. Secondary ions were accelerated at 10 kV, and the transfer optics were set at 200× magnification. A primary beam was defocused to a 10-15-μm spot on the surface, and secondary ions from the 5 × 5 μm area in the center were transmitted to the ion optics, to eliminate secondary ion signals from surface contamination and the edge of the primary beam. The $^{16}OH^-$, $^{12}C^-$, $^{19}F^-$, $^{32}S^-$, $^{35}Cl^-$, and $^{31}P^-$ signal intensities were measured using a magnetic peak switching method and normalized with $^{30}Si^-$. The calibration lines were obtained from a set of silicate glass standards reported in (Shimizu et al., 2017; Shimizu et al., 2022). EPR-G3 basalt glass standard was reanalyzed for stability control during all analytical sessions (Supplementary Table A2). Relative standard deviations are 0.8% for H_2O, 3.6% for CO_2, 2% for F, 0.9% for P_2O_5, 0.8% for S and 1.3% for Cl contents (Shimizu et al., 2017). The detection limits of glass H_2O, CO_2, F, P_2O_5, S, and Cl contents derived from the 3σ deviation of pure quartz glass were 12, 3, 0.1, 2, 0.1, and 0.05 ppm, respectively (Shimizu et al., 2017).

Table A2. Summary of repeated analyses of a secondary standard by SIMS

SIMS (IMS-1280HR, CAMECA, France) at the Kochi Institute for Core Sample Research, JAMSTEC, Japan						
	H_2O, wt%	CO_2, ppm	Cl, ppm	S, ppm	F, ppm	P_2O_5, wt%
Basaltic glass EPR-G3						
Repeated analysis (average), N=10	0.23	253	166	1268	146	0.15
1σ	0.002	4	2	4	1	0.001
Reference value recommended for glass EPR-G3 from (Shimizu et al., 2017)[1]	0.22	173	158	1269	147	0.16

Notes: bdl - below dection limit; n.a.=not analyzed

1. Shimizu, K., Ushikubo, T., Hamada, M., Itoh, S., Higashi, Y., Takahashi, E. & Ito, M. (2017). H2O, CO2, F, S, Cl, and P2O5 analyses of silicate glasses using SIMS: Report of volatile standard glasses. Geochemical Journal 51, 299–313.

Melt inclusion homogenization experiments

A significant part of this study is focused on the study of melt inclusions. However, MIs in Onikobe and Naruko deposits are partially or entirely crystallized and are unsuitable for studying the composition of the trapped melt. To homogenize MIs, we performed experiments at a given pressure and temperature. Experiments on the homogenization of inclusions were carried out only with inclusions in quartz. MIs in plagioclase and orthopyroxene were not homogenized for fear of loss of volatiles during the experiment because these minerals are potentially much worse container for volatiles than quartz. However, inclusions in pyroxene often do not show significant post-homogenization crystallization and can be used for analysis without additional experiments. Thus, this study presents the results of the study of homogenized MIs in quartz, inclusions in orthopyroxene that were not homogenized and groundmass glass.

Homogenization experiments were performed using a cold seal pressure vessel at Tohoku University (Okumura et al., 2019). Quartz crystals were put into a welded Au tube. In the experiments, we first increased temperature and pressure, and then the Au tube was set to the hotspot of the furnace using a filer rod, which is movable in a pressure vessel using an outer magnet (Matsumoto et al., 2023 in press). All the experiments were conducted at a temperature of 835°C under a pressure of 140 MPa. The temperature is chosen according to the results of experiments on MIs homogenization at atmospheric pressure in the Lincam1500 stage. The pressure was set at 140 MPa, based on amphibole barometry.

The experiments were carried out for 2 and 5 h. The homogenization result for 2 h showed that not all large MIs in quartz (more than 100 μm) have time to homogenize. In the experiment with a duration of 5 h, most MIs homogenized.

Supplementary material

Table S2.1. Whole rock composition (XRF and ICP)

	Pumice from caldera-forming pyroclastic flow				Syncaldera Extrusion Dome		
	KY-18-01	KY-18-03	KY-18-04	KY-18-05	KY-18-07	KY-18-08	KY-18-09
SiO_2, wt%	66.19	65.36	66.34	66.04	71.22	71.77	73.12
TiO_2, wt%	0.57	0.55	0.53	0.57	0.42	0.44	0.44
Al_2O_3, wt%	14.52	14.30	14.50	14.62	12.97	13.03	13.38
FeO, wt%	4.16	4.41	3.99	4.22	3.10	3.28	3.19
MnO, wt%	0.12	0.11	0.12	0.12	0.08	0.08	0.08
MgO, wt%	1.13	1.08	1.01	1.12	0.67	0.78	0.70
CaO, wt%	4.22	4.14	4.08	4.21	2.99	3.06	3.03
Na_2O, wt%	3.68	3.49	3.69	3.61	4.00	4.06	4.10
K_2O. wt%	1.01	0.95	0.96	0.92	1.11	1.12	1.05
P_2O_5, wt%	0.11	0.10	0.10	0.10	0.06	0.07	0.06
LOI	3.70	4.70	3.93	3.81	3.16	1.54	0.72
Total	99.49	99.28	99.34	99.43	99.88	99.33	99.96
Rb, ppm	9.8	10.4	10.1	11.1	11.8	12.7	9.9
Ba, ppm	262.6	261.1	271.1	267.8	317.0	319.5	341.3
Th, ppm	1.0	1.0	1.0	1.1	1.5	1.6	1.7
U, ppm	0.4	0.4	0.5	0.5	0.6	0.6	0.7
Nb, ppm	1.1	1.0	1.0	1.0	1.2	1.2	1.2
Ta, ppm	0.1	0.1	0.1	0.1	0.1	0.1	0.1
La, ppm	6.0	5.8	5.8	5.8	6.9	7.1	7.6
Ce, ppm	15.4	15.2	15.7	15.6	18.2	18.7	19.5
Pb, ppm	15.1	11.3	11.2	13.2	13.9	12.2	12.0
Pr, ppm	2.4	2.3	2.4	2.4	2.8	2.9	2.9
Sr, ppm	203.4	204.3	202.2	200.5	151.1	154.6	159.8
Nd, ppm	12.2	12.0	12.1	12.2	14.1	14.5	14.6
Sm, ppm	3.8	3.6	3.7	3.8	4.2	4.2	4.0
Zr, ppm	102.7	100.8	103.0	102.5	130.5	133.5	138.8
Hf, ppm	2.8	2.8	2.9	2.9	3.9	3.8	4.0
Eu, ppm	1.1	1.1	1.2	1.2	1.0	1.0	1.1
Gd, ppm	4.4	4.5	4.5	4.4	5.1	5.3	5.2
Tb, ppm	0.7	0.8	0.8	0.8	0.9	1.0	0.9
Dy, ppm	5.3	5.5	5.7	5.5	6.3	6.6	6.4
Y, ppm	35.8	34.6	35.5	36.2	41.0	41.3	41.2
Ho, ppm	1.3	1.3	1.3	1.2	1.5	1.4	1.5
Er, ppm	3.9	3.7	3.8	3.8	4.4	4.4	4.3
Tm, ppm	0.6	0.6	0.6	0.6	0.7	0.7	0.7
Yb, ppm	4.0	3.9	3.9	4.0	4.4	4.7	4.8
Lu, ppm	0.6	0.6	0.6	0.6	0.7	0.7	0.7

Table S2.2. Phenocrysts modal abundances in Mendeleev pumice

	Pumice from caldera-forming pyroclastic flow				Syncaldera Extrusion Dome		
	KY-18-01	KY-18-03	KY-18-04	KY-18-05	KY-18-07	KY-18-08	KY-18-09
% Plag	16.7	16.5	18.5	16.7	not analyzed	18.9	21.2
% Opx	3.6	3.6	3.0	1.9		1.9	1.5
% Cpx	4.8	3.3	2.8	2.9		1.9	1.4
% Qu	1.0	0.5	0.5	0.7		7.5	9.1
% Oxides	2.4	1.9	1.4	1.2		0.6	0.8
% Groundmass	71.6	74.2	73.9	76.6		69.2	66.0

Table S3.1. Naruko and Onikobe whole-rock composition (XRF)

Deposit	Ikezuki (Onikobe caldera)									Shimoyamazato (Onikobe caldera)			
Description	Unit 1. Strongly welded tuff. Bottom part				Unit 2. Strongly welded tuff. Middle-upper part		Unit 2. Medium welded tuffs. Upper part			Pumice. Bottom part		Pumice. Upper part	
Sample #	7 3 glass	7 4 glass	7 3 Pellet	7 4 Pellet	8(1) glass	8(2) Pellet	9 Pellet	10 Pellet	10 glass	1glass	1pellet	2glass	2pellet
SiO_2, wt%	70.65	72.14	74.40	74.90	73.70	74.07	73.89	74.67	70.52	74.93	73.61	75.71	74.82
TiO_2, wt%	0.50	0.56	0.33	0.32	0.52	0.28	0.31	0.29	0.60	0.36	0.24	0.39	0.23
Al_2O_3, wt%	14.17	14.60	13.96	13.74	14.51	13.20	13.53	14.46	15.46	13.19	11.79	12.80	11.40
FeO, wt%	3.66	4.31	2.32	2.73	4.47	3.13	2.47	2.49	4.48	2.05	1.92	2.26	1.80
MnO, wt%	0.08	0.12	0.07	0.18	0.12	0.12	0.10	0.09	0.12	0.07	0.09	0.08	0.09
MgO, wt%	0.91	1.05	0.29	0.32	0.88	0.28	0.26	0.23	1.02	0.39	0.25	0.45	0.23
CaO, wt%	3.57	3.76	3.36	3.30	3.61	3.18	2.85	2.69	3.84	2.43	2.23	2.29	1.99
Na_2O, wt%	4.20	4.24	4.66	4.38	4.30	4.61	3.87	4.02	3.94	4.16	3.82	4.08	3.88
K_2O, wt%	1.35	1.28	1.35	1.35	1.41	1.40	1.64	1.22	1.05	1.72	1.68	1.72	1.73
P_2O_5, wt%	0.08	0.09	0.15	0.14	0.08	0.15	0.09	0.17	0.08	0.06	0.12	0.06	0.07
Total	99.2	102.2	100.9	101.4	103.6	100.4	99.0	100.3	101.1	99.4	95.8	99.8	96.2
LOI										2.65		2.55	
V, ppm			29	25		32	35	43			19		18
Cr, ppm			bdl	bdl		bdl	bdl	bdl			bdl		bdl
Ni, ppm			5.3	4.9		4.9	5.6	4.8			5.0		5.0
Rb, ppm			31	32		30	33	25			35		37
Sr, ppm			178	177		175	171	185			152		137
Y, ppm			39	36		45	40	36			45		45
Zr, ppm			144	146		135	146	159			165		182
Nb, ppm			4.9	4.9		4.9	4.6	4.9			5.0		6.0
Ba, ppm			376	383		408	354	305			397		414
Co, ppm			5.1	6.9		8.4	6.3	7.0			4.1		3.6
Cu, ppm			10	10		11	9	10			10		7
Zn, ppm			56	56		52	51	49			68		64
As, ppm			1.3	2.2		4.8	1.8	1.0			3.0		3.3
Sn, ppm			1.0	1.5		1.2	1.6	1.9			2.1		1.6
Sb, ppm			0.2	0.4		0.4	0.5	0.6			0.5		0.4
Cs, ppm			1.2	2.1		1.3	1.6	1.0			1.9		2.0
La, ppm			12	12		12	12	12			13		14
Ce, ppm			27	29		27	27	32			30		30
Pr, ppm			2.5	2.9		4.4	3.2	4.1			2.9		2.9
Nd, ppm			16	14		16	14	14			17		18
Pb, ppm			11	12		9	12	11			18		15
Th, ppm			3.6	3.8		3.0	3.4	3.4			4.4		4.8

**bdl – below detection limit*

Table S3.1. Naruko and Onikobe whole-rock composition (XRF) (Continue)

Deposit	Yanagisawa (Naruko caldera)											
Description	Pumice. Bottom part.			Pumice. Middle part				Pumice. Upper part				Ash layer. Upper part.
Sample #	1-3 Yan	1-3 Pumice Yan	1-3 All	4 1 glass	4 2 glass	4 pellet	8-yan	1-1 Yan P	1-1 Yan all	1-1 Yan P	7-yan	1-2 Yan Ash
SiO_2, wt%	74.53	77.68	73.42	74.37	74.72	73.53	71.05	77.15	75.17	76.47	72.21	73.63
TiO_2, wt%	0.34	0.22	0.28	0.34	0.36	0.27	0.24	0.15	0.19	0.14	0.22	0.26
Al_2O_3, wt%	12.62	11.73	12.14	13.15	13.61	12.70	10.79	11.36	11.68	11.30	10.82	11.92
FeO, wt%	2.83	1.65	2.02	1.94	2.16	1.90	1.66	1.34	1.83	1.33	1.64	2.09
MnO, wt%	0.07	0.09	0.09	0.07	0.07	0.09	0.07	0.07	0.07	0.08	0.09	0.08
MgO, wt%	1.00	0.16	0.70	0.45	0.52	0.35	0.23	0.03	0.27	0.04	0.06	0.45
CaO, wt%	1.66	1.93	2.19	2.23	2.39	2.14	2.03	1.17	1.34	1.13	1.82	1.70
Na_2O, wt%	3.14	4.17	3.60	4.13	4.17	3.81	3.46	3.06	2.81	3.02	3.58	3.52
K_2O, wt%	1.64	1.41	1.40	1.54	1.51	1.42	1.57	2.25	2.11	2.29	1.80	1.71
P_2O_5, wt%	0.08	0.05	0.07	0.02	0.02	0.08	0.05	0.04	0.04	0.04	0.07	0.06
Total	97.9	99.1	95.9	98.2	99.5	96.3	91.2	96.6	95.5	95.8	92.3	95.4
LOI				3.05	3.05							
V, ppm	49	10	33			23	25	6	7	3	9	28
Cr, ppm	20	60	27			bdl	25	4	5	20	bdl	9
Ni, ppm	23.9	25.9	14.8			5.0	16.3	11.1	10.9	14.3	10.0	15.0
Rb, ppm	33	31	29			35	36	36	36	37	37	37
Sr, ppm	118	131	165			129	129	97	115	93	138	124
Y, ppm	39	38	32			32	32	58	52	58	46	42
Zr, ppm	133	184	141			171	167	189	179	182	191	176
Nb, ppm	6.0	5.6	4.8			6.0	5.5	7.3	6.6	7.5	6.1	5.4
Ba, ppm	338	393	332			414	404	475	450	477	419	420
Co, ppm	7.1	2.1	3.6			4.0	2.6	0.7	2.5	0.7	1.8	3.8
Cu, ppm	15	9	12			9	8	7	8	7	7	11
Zn, ppm	84	55	67			54	51	74	84	76	64	67
As, ppm	9.9	3.2	3.5			3.8	4.4	2.4	1.9	3.1	4.0	4.6
Sn, ppm	2.0	1.7	1.4			1.8	2.0	2.1	2.1	2.1	1.8	1.5
Sb, ppm	2.1	0.8	0.6			0.4	0.8	1.0	0.7	1.0	0.8	0.7
Cs, ppm	1.0	1.8	1.6			2.6	2.2	1.8	1.9	1.7	1.5	2.3
La, ppm	11	12	11			13	11	17	16	17	12	13
Ce, ppm	24	26	23			29	25	38	35	38	29	28
Pr, ppm	3.4	3.7	3.3			2.5	1.9	4.2	3.4	2.3	2.2	3.6
Nd, ppm	13	14	13			12	11	20	19	21	16	16
Pb, ppm	19	11	12			14	13	13	12	12	15	13
Th, ppm	4.3	4.7	4.8			5.2	5.6	6.5	6.2	6.6	5.6	5.1

**bdl – below detection limit*

References

Allan, A. S., Morgan, D. J., Wilson, C. J., & Millet, M. A. (2013). From mush to eruption in centuries: assembly of the super-sized Oruanui magma body. *Contributions to Mineralogy and Petrology*, 166, 143-164.

Amanda, F. F., Yamada, R., Uno, M., Okumura, S., & Tsuchiya, N. (2019). Evaluation of caldera hosted geothermal potential during volcanism and magmatism in subduction system, NE Japan. *Geofluids*, 2019, 1-14.

Andersen, D. & Lindsley, D.H. (1985). New (and final!) models for the Ti-magnetite/ ilmenite geothermometer and oxygen barometer. *AGU Spring Meeting, American Geophysical Union* 416.

Annen, C. & Sparks, R.S.J. (2002). Effects of repetitive emplacement of basaltic intrusions on thermal evolution and melt generation in the crust. *Earth and Planetary Science Letters* 203, 937-955.

Annen, C., Blundy, J.D. & Sparks, R.S.J. (2006). The genesis of intermediate and silicic magmas in deep crustal hot zones. *Journal of petrology* 47, 505–539.

Asamori, K., Umeda, K., Ogawa, Y., & Oikawa, T. (2010). Electrical resistivity structure and helium isotopes around Naruko volcano, northeastern Japan and its implication for the distribution of crustal magma. *International Journal of Geophysics*, 2010, 1-7.

Asimow, P. D., & Ghiorso, M. S. (1998). Algorithmic modifications extending MELTS to calculate subsolidus phase relations. *American Mineralogist*, 83(9-10), 1127-1132.

Atherton, M.P. & Petford, N. (1993). Generation of sodium-rich magmas from newly underplated basaltic crust. *Nature* 362, 144–146

Bachmann, O., Dungan, M. A., & Lipman, P. W. (2002). The Fish Canyon magma body, San Juan volcanic field, Colorado: rejuvenation and eruption of an upper-crustal batholith. *Journal of Petrology*, 43(8), 1469-1503.

Bachmann, O., & Bergantz, G. W. (2004). On the origin of crystal-poor rhyolites: extracted from batholithic crystal mushes. *Journal of Petrology*, 45(8), 1565-1582.

Bachmann, O., & Bergantz, G. W. (2006). Gas percolation in upper-crustal silicic crystal mushes as a mechanism for upward heat advection and rejuvenation of near-solidus

magma bodies. *Journal of Volcanology and Geothermal research*, 149(1-2), 85-102.

Bachmann, O., & Bergantz, G. W. (2008). Deciphering magma chamber dynamics from styles of compositional zoning in large silicic ash flow sheets. *Reviews in Mineralogy and Geochemistry*, 69(1), 651-674.

Bacon, C.R. & Hirschmann, M.M. (1988). Mg/Mn partitioning as a test for equilibrium between coexisting Fe-Ti oxides. *American Mineralogist* 73, 57–61

Ban, M., Takahasi, K., Horie, T. & Toya, N. (2005). Petrogenesis of mafic inclusions in rhyolitic lavas from Narugo volcano, Northeastern Japan. *Journal of Petrology* 46, 1543–1563.

Barth, A., Newcombe, M., Plank, T., Gonnermann, H., Hajimirza, S., Soto, G.J., Saballos, A. & Hauri, E. (2019). Magma decompression rate correlates with explosivity at basaltic volcanoes — Constraints from water diffusion in olivine. *Journal of Volcanology and Geothermal Research* 387, 106664.

Barth, A. & Plank, T. (2021). The Ins and Outs of Water in Olivine-Hosted Melt Inclusions: Hygrometer vs. Speedometer. *Frontiers in Earth Science* 9, 343.

Bas, M.J.L., Maitre, R.W.L., Streckeisen, A. & Zanettin, B. (1986). A chemical classification of volcanic rocks based on the total alkali-silica diagram. *Journal of Petrology* 27, 745–750.

Bazanova, L.I., Melekestsev, I.V., Ponomareva, V.V., Dirksen, O.V. & Dirksen, V.G. (2016). Late Pleistocene and Holocene volcanic catastrophes in Kamchatka and in the Kuril Islands. Part 1. Types and classes of catastrophic eruptions as the leading components of volcanic catastrophism. *Journal of Volcanology and Seismology* 10, 151-169.

Beard, J.S. & Lofgren, G.E. (1991). Dehydration melting and water-saturated melting of basaltic and andesitic greenstones and amphibolites at 1, 3, and 6.9 kb. *Journal of Petrology* 32 365–401

Bergantz, G. W., & Breidenthal, R. E. (2001). Non-stationary entrainment and tunneling eruptions: A dynamic link between eruption processes and magma mixing. *Geophysical Research Letters*, 28(16), 3075-3078.

Bergantz, G. W., Schleicher, J. M., & Burgisser, A. (2015). Open-system dynamics and mixing in magma mushes. *Nature Geoscience*, 8(10), 793-796.

Blatter, D.L., Sisson, T.W. & Hankins, W.B. (2017). Voluminous arc dacites as amphibole reaction-boundary liquids. *Contributions to Mineralogy and Petrology* 172, 27.

Blundy, J. & Cashman, K. (2005). Rapid decompression-driven crystallization recorded by melt inclusions from Mount St. Helens volcano. *Geolog*y 33, 793–796.

Boynton, C. H., Westbrook, G. K., Bott, M. H. P., & Long, R. E. (1979). A seismic refraction investigation of crustal structure beneath the Lesser Antilles island arc. *Geophysical Journal International*, 58(2), 371-393.

Braitseva, O.A., Melekestsev, I.V., Ponomareva, V.V. & Sulerzhitsky, L.D. (1995). The ages of calderas, large explosive craters and active volcanoes in the Kuril-Kamchatka region, Russia. *Bulletin of Volcanology* 57, 383–402.

Candela, P. A. (1997). A review of shallow, ore-related granites: textures, volatiles, and ore metals. *Journal of petrology*, 38(12), 1619-1633.

Cashman, K. V. & Edmonds, M. (2019). Mafic glass compositions: a record of magma storage conditions, mixing and ascent. *Philosophical Transactions of the Royal Society* 377 (2139), 20180004

Chakraborty, S., & Dohmen, R. (2022). Diffusion chronometry of volcanic rocks: looking backward and forward. *Bulletin of Volcanology*, 84(6), 57.

Chamberlain, K. J., Morgan, D. J., & Wilson, C. J. (2014). Timescales of mixing and mobilisation in the Bishop Tuff magma body: perspectives from diffusion chronometry. *Contributions to Mineralogy and Petrology*, 168, 1-24.

Cherniak, D. J., Watson, E. B., & Wark, D. A. (2007). Ti diffusion in quartz. *Chemical Geology*, 236(1-2), 65-74

Chesner, C.A. (1998) Petrogenesis of the Toba Tuffs, Sumatra, Indonesia. *Journal of Perology* 39, 397–438.

Christeson, G. L., Mann, P., Escalona, A., & Aitken, T. J. (2008). Crustal structure of the Caribbean–northeastern South America arc-continent collision zone. *Journal of Geophysical Research: Solid Earth*, 113(B8).

Cooper, G. F., Wilson, C. J., Millet, M. A., & Baker, J. A. (2016). Generation and rejuvenation of a supervolcanic magmatic system: a case study from Mangakino volcanic centre, New Zealand. *Journal of Petrology*, 57(6), 1135-1170.

Cooper, G. F., Morgan, D. J., & Wilson, C. J. (2017). Rapid assembly and rejuvenation of a large silicic magmatic system: Insights from mineral diffusive profiles in the Kidnappers and Rocky Hill deposits, New Zealand. *Earth and Planetary Science Letters*, 473, 1-13.

Cooper, K. M. (2019). Time scales and temperatures of crystal storage in magma reservoirs: implications for magma reservoir dynamics. *Philosophical Transactions of the Royal Society*, 377(2139), 20180009.

Costa, F., Dohmen, R., & Chakraborty, S. (2008). Time scales of magmatic processes from modeling the zoning patterns of crystals. *Reviews in Mineralogy and Geochemistry*, 69(1), 545-594.

Costa, F., Shea, T., & Ubide, T. (2020). Diffusion chronometry and the timescales of magmatic processes. *Nature Reviews Earth & Environment*, 1(4), 201-214.

Costa, F. (2021). Clocks in magmatic rocks. *Annual Review of Earth and Planetary Sciences*, 49, 231-252.

Couperthwaite, F. K., Thordarson, T., Morgan, D. J., Harvey, J., & Wilson, M. (2020). Diffusion timescales of magmatic processes in the Moinui lava eruption at Mauna Loa, Hawaii, as inferred from bimodal olivine populations. *Journal of Petrology*, 61(7), egaa058.

De Grave, J., Zhimulev, F.I., Glorie, S., Kuznetsov, G.V., Evans, N., Vanhaecke, F. & McInnes, B. (2016). Late Palaeogene emplacement and late Neogene-Quaternary exhumation of the Kuril island-arc root (Kunashir Island) constrained by multi-method thermochronometry. *Geoscience Frontiers* 7, 211–220.

Dohmen, R., & Chakraborty, S. (2007). Fe–Mg diffusion in olivine II: point defect chemistry, change of diffusion mechanisms and a model for calculation of diffusion coefficients in natural olivine. *Physics and Chemistry of Minerals*, 34(6), 409-430.

Dohmen, R., Ter Heege, J. H., Becker, H. W., & Chakrabortrty, S. (2016). Fe-Mg interdiffusion in orthopyroxene. *American Mineralogist*, 101(10), 2210-2221.

Dohmen, R., Faak, K., & Blundy, J. D. (2017). Chronometry and speedometry of magmatic processes using chemical diffusion in olivine, plagioclase and pyroxenes. *Reviews in Mineralogy and Geochemistry*, 83(1), 535-575.

Ganguly, J., & Tazzoli, V. (1994). Fe^{2+}-Mg interdiffusion in orthopyroxene: Retrieval from the data on intracrystalline exchange reaction. *American Mineralogist*, 79(9-10), 930-937

Ghiorso, M. S., & Sack, R. O. (1995). Chemical mass transfer in magmatic processes IV. A revised and internally consistent thermodynamic model for the interpolation and extrapolation of liquid-solid equilibria in magmatic systems at elevated temperatures and pressures. *Contributions to Mineralogy and Petrology*, 119, 197-212.

Gorshkov, G.S. (1967). *Volcanism of the Kuril Island arc.* Nauka, Moscow (In Russian).

Gualda, G. A., Ghiorso, M. S., Lemons, R. V., & Carley, T. L. (2012). Rhyolite-MELTS: a modified calibration of MELTS optimized for silica-rich, fluid-bearing magmatic systems. *Journal of Petrology*, 53(5), 875-890.

Elms, H. C., Barker, S. J., Morgan, D. J., Wilson, C. J., & Charlier, B. L. (2023). Processes and timescales of magmatic rejuvenation and residence prior to post-caldera rhyolitic eruptions: Ōkataina Volcanic Centre, Aotearoa New Zealand. *Journal of Volcanology and Geothermal Research*, 437, 107790.

Erdmann, M. & Koepke, J. (2016). Silica-rich lavas in the oceanic crust: experimental evidence for fractional crystallization under low water activity. *Contributions to Mineralogy and Petrology* 171.

Flaherty, T., Druitt, T. H., Tuffen, H., Higgins, M. D., Costa, F., & Cadoux, A. (2018). Multiple timescale constraints for high-flux magma chamber assembly prior to the Late Bronze Age eruption of Santorini (Greece). *Contributions to Mineralogy and Petrology*, 173, 1-21.

Frost, B.R., Barnes, C.G., Collins, W.J., Arculus, R.J., Ellis, D.J. & Frost, C.D. (2001). A geochemical classification for granitic rocks. *Journal of Petrology* 42, 2033–2048.

Ghiorso, M.S. & Evans, B.W. (2008). Thermodynamics of rhombohedral oxide solid solutions and a revision of the Fe-Ti two-oxide geothermometer and oxygen-barometer. *American Journal of Science* 308, 957–1039.

Gill, J.B. (1981). *Orogenic Andesites and Plate Tectonics*. Springer, Berlin, Heidelberg

Grocke, S.B., de Silva, S.L., Iriarte, R., Lindsay, J. M. & Cottrell, E. (2017). Catastrophic Caldera-Forming (CCF) Monotonous Silicic Magma Reservoirs: Geochemical and Petrological Constraints on Heterogeneity, Magma Dynamics, and Eruption Dynamics of the 3·49 Ma Tara Supereruption, Guacha II Caldera, SW Bolivia. *Journal of Petrology* 58, 227–260.

Grove, T., Parman, S., Bowring, S., Price, R. & Baker, M. (2002). The role of an H_2O-rich

fluid component in the generation of primitive basaltic andesites and andesites from the Mt. Shasta region, N California. Contributions to Mineralogy and Petrology 142 375–396

Grove TL, Elkins-Tanton LT, Parman SW, Chatterjeem N., Muntener, O. & Gaetani, G.A. (2003). Fractional crystallization and mantle-melting controls on calc-alkaline differentiation trends. *Contributions to Mineralogy and Petrology* 145 515–533

Grove, T. L., Till, C. B., & Krawczynski, M. J. (2012). The role of H_2O in subduction zone magmatism. *Annual Review of Earth and Planetary Sciences*, 40, 413-439

Hacker, B. R. (2008). H_2O subduction beyond arcs. *Geochemistry, Geophysics, Geosystems*, 9(3).

Hammerli, J., Kemp, A., Shimura, T., Vervoort, J.D., EIMF & Dunkley, D.J. (2018). Generation of I-type granitic rocks by melting of heterogeneous lower crust. *Geology* 46, 907–910.

Hasegawa, A., Nakajima, J., Umino, N., Miura, S. (2005). Deep structure of the northeastern Japan arc and its implications for crustal deformation and shallow seismic activity. *Tectonophysics* 403, 59–75.

Hasegawa, A., Nakajima, J., Uchida, N., Okada, T., Zhao, D., Matsuzawa, T., & Umino, N. (2009). Plate subduction, and generation of earthquakes and magmas in Japan as inferred from seismic observations: An overview. *Gondwana Research*, 16(3-4), 370-400.

Hawthorne, F.C., Oberti, R., Harlow, G.E., Maresch, W.V., Martin, R.F., Schumacher, J.C. & Welch, M.D. (2012). Nomenclature of the amphibole supergroup. *American Mineralogist* 97, 2031–2048.

Hernández, P.A., Mori, T., Padrón, E., Sumino, H. & Pérez, N. (2011). Carbon dioxide emission from Katanuma volcanic lake, Japan. *Earth, Planets and Space* 63, 1151–1156.

Hildreth, W. (1981). Gradients in silicic magma chambers: implications for lithospheric magmatism. *Journal of Geophysical Research: solid earth*, 86(B11), 10153-10192.

Hildreth, W. (2004). Volcanological perspectives on Long Valley, Mammoth Mountain, and Mono Craters: several contiguous but discrete systems. *Journal of Volcanology and Geothermal Research* 136, 169-198.

Hoang, N., Itoh, J. & Miyagi, I. (2011). Subduction components in Pleistocene to recent Kurile arc magmas in NE Hokkaido, Japan. *Journal of Volcanology and Geothermal Research*

200, 255–266.

Holland, T. & Blundy, J. (1994). Non-ideal interactions in calcic amphiboles and their bearing on amphibole-plagioclase thermometry. Contributions to Mineralogy and Petrology 116, 433–447.

Holloway, J.R. & Burnham, C.W. (1972). Melting relations of basalt with equilibrium water pressure less than total pressure. *Journal of Petrology* 13, 1–29.

Huber, C., Bachmann, O., & Dufek, J. (2011). Thermo-mechanical reactivation of locked crystal mushes: Melting-induced internal fracturing and assimilation processes in magmas. *Earth and Planetary Science Letters*, 304(3-4), 443-454.

Huber, C., Townsend, M., Degruyter, W. & Bachmann, O. (2019). Optimal depth of subvolcanic magma chamber growth controlled by volatiles and crust rheology. *Nature Geoscience* 12, 762–768.

Humphreys, M.C.S., Cooper, G.F., Zhang, J., Loewen, J., Kent, A.J.R., Macpherson C.G., Davidson J.P. (2019). Unravelling the complexity of magma plumbing at Mount St. Helens: a new trace element partitioning scheme for amphibole. *Contributions to Mineralogy and Petrology* 174.

Huppert, H.E. & Sparks, R.S.J. (1988). The Generation of Granitic Magmas by Intrusion of Basalt into Continental Crust. *Journal of Petrology* 29, 599-624.

Iwamori, H. (1998). Transportation of H_2O and melting in subduction zones. Earth and *Planetary Science Letters*, 160(1-2), 65-80.

Iwasaki, T., Kato, W., Moriya, T., Hasemi, A., Umino, N., Okada, T., Miyashita, K., Mizogami, T., Takeda, T., Sekine, S., Matsushima, T., Tashiro, K. & Miyamachi, H. (2001). Extensional structure in northern Honshu Arc as inferred from seismic refraction/wide-angle reflection profiling. *Geophysical Research Letters*, 28(12), 2329-2332.

Iwasaki, T., Adachi, K., Moriya, T., Miyamachi, H., Matsushima, T., Miyashita, K., Takeda T.,Taira, T., Yamada, T. & Ohtake, K. (2004). Upper and middle crustal deformation of an arc–arc collision across Hokkaido, Japan, inferred from seismic refraction/wide-angle reflection experiments. *Tectonophysics*, 388(1-4), 59-73.

Iwasaki T, Tsumura N, Ito T, Arita K, Makoto M, Sato H, Kurashimo E, Hirata N, Abe S, Noda K, Fujiwara A, Kikuchi S & Suzuki K (2019) Structural heterogeneity in and around the

fold-and-thrust belt of the Hidaka Collision zone, Hokkaido, Japan and its relationship to the aftershock activity of the 2018 Hokkaido Eastern Iburi Earthquake. *Earth Planets Space* 71(1):103.

Izbekov, P., Gardner, J.E. & Eichelberger, J.C. (2004). Comagmatic granophyre and dacite from Karymsky volcanic center, Kamchatka: experimental constraints for magma storage conditions. *Journal of Volcanology and Geothermal Research* 131, 1–18.

Jarrard, R. D. (2003). Subduction fluxes of water, carbon dioxide, chlorine, and potassium. *Geochemistry, Geophysics, Geosystems*, 4(5).

Jarosewich, E., Nelen, J.A. & Norberg, J.A. (1980). Reference Samples for Electron Microprobe Analysis. *Geostandart Newsletters* 4, 43–47.

Kahl, M., Chakraborty, S., Costa, F., & Pompilio, M. (2011). Dynamic plumbing system beneath volcanoes revealed by kinetic modeling, and the connection to monitoring data: An example from Mt. Etna. *Earth and Planetary Science Letters*, 308(1-2), 11-22.

Kalacheva, E., Taran, Y., Voloshina, E. & Inguaggiato, S. (2017a). Hydrothermal system and acid lakes of Golovnin caldera, Kunashir, Kuril Islands: Geochemistry, solute fluxes and heat output. *Journal of Volcanology and Geothermal Research* 346, 10–20.

Kalacheva, E., Taran, Y., Kotenko, T., Inguaggiato, S. & Voloshina, E. (2017b). The hydrothermal system of Mendeleev Volcano, Kunashir Island, Kuril Islands: The geochemistry and the transport of magmatic components. *Journal of Volcanology and Seismology* 11, 335–352.

Kawamoto, T. (1996). Experimental constraints on differentiation and H_2O abundance of calc-alkaline magmas. *Earth and Planetary Science Letters* 144, 577–589.

Kimura, J. I., & Yoshida, T. (2006). Contributions of slab fluid, mantle wedge and crust to the origin of Quaternary lavas in the NE Japan arc. *Journal of Petrology*, 47(11), 2185-2232.

Kimura, J. I., & Nakajima, J. (2014). Behaviour of subducted water and its role in magma genesis in the NE Japan arc: A combined geophysical and geochemical approach. *Geochimica et Cosmochimica Acta*, 143, 165-188.

Kimura, J. I. (2017). Modeling chemical geodynamics of subduction zones using the Arc Basalt Simulator version 5. *Geosphere*, 13(4), 992-1025.

Kodaira, S., Sato, T., Takahashi, N., Ito, A., Tamura, Y., Tatsumi, Y., & Kaneda, Y. (2007).

Seismological evidence for variable growth of crust along the Izu intraoceanic arc. *Journal of Geophysical Research: Solid Earth*, 112(B5).

Koloskov, A. V., Fedorov, P. I., & Okina O.I. (2019). New data on composition of intrusive rocks from Shikotan island (Lesser Kuril Chain) // Vestnik KRAUNTs. Nauki o Zemle. 3(43), 52-65.

Kopp, H., Weinzierl, W., Becel, A., Charvis, P., Evain, M., Flueh, E. R., ... & Roux, E. (2011). Deep structure of the central Lesser Antilles Island Arc: relevance for the formation of continental crust. *Earth and Planetary Science Letters,* 304(1-2), 121-134.

Kotov, A.A., Smirnov, S.Z., Plechov, P.Y. Persikov, E.S., Chertkova, N.V., Maksimovich, I.A., Karmanov, N.S. & Buhtiyarov P.G. (2021). Method for Determining Water Content in Natural Rhyolitic Melts by Raman Spectroscopy and Electron Microprobe Analysis. *Petrology* 29, 386–403.

Kotov, A., Smirnov, S., Nizametdinov, I., Uno, M., Tsuchiya, N., & Maksimovich, I. (2023). Partial melting under shallow-crustal conditions: a study of the Pleistocene caldera eruption of Mendeleev volcano, southern Kuril Island Arc. *Journal of Petrology*, 64(6), egad033.

Laverov, N.P. (2005), *The latest and modern volcanism in Russia*. Nauka, Moscow (In Russian).

Li, X., Zhang, C., Almeev, R. R., & Holtz, F. (2020). GeoBalance: An Excel VBA program for mass balance calculation in geosciences. Geochemistry, 80(2), 125629.

Li, J., Ding, X., & Liu, J. (2022). The role of fluids in melting the continental crust and generating granitoids: An overview. *Geosciences*, 12(8), 285.

Lloyd, A.S., Plank, T., Ruprecht, P., Hauri, E.H. & Rose, W. (2012). Volatile loss from melt inclusions in pyroclasts of differing sizes. *Contributions to Mineralogy and Petrology* 165, 129–153.

Locock, A.J., 2014. An Excel spreadsheet to classify chemical analyses of amphiboles following the IMA 2012 recommendations. *Computer Geosciences* 62, 1–11.

Martynov, Y.A., Dril, S.I., Chashchin, A.A., Rybin, A.V. & Martynov A.Y. (2005). Geochemistry of basalts from Kunashir and Iturup Islands: A role for non-subduction factors in the genesis of Kuril Island arc magmas. *Geokhimiya* 43, 369–383.

Martynov, A.Y., Kimura, J.I., Martynov, Y.A. & Rybin, A.V. (2010a) Geochemistry of late Cenozoic lavas on Kunashir Island, Kurile Arc. *Island Arc* 19, 86–104.

Martynov, Y.A., Khanchuk, A.I., Kimura, J-I., Rybin, A.V. & Martynov, A.Y. (2010b). Geochemistry and Petrogenesis of Volcanic Rocks in the Kuril Island Arc. *Pertology* 18, 489-513.

Martynov, A. Yu., Martynov, Yu. A., Rybin, A. V. & Kimura, J.-I. (2015). Role of back-arc tectonics in the origin of subduction magmas: new Sr, Nd, and Pb isotope data from Middle Miocene lavas of Kunashir Island (Kurile Island Arc). *Russian Geology and Geophysics* 56, 363-378.

Martynov, A.Y. & Martynov, Y.A. (2017). Pleistocene basaltic volcanism of Kunashir Island (Kuril Island arc): Mineralogy, geochemistry, and results of computer simulation. *Petrology* 25, 206–225.

Marxer, F., Ulmer, P. & Müntener, O. (2022). Polybaric fractional crystallisation of arc magmas: an experimental study simulating trans-crustal magmatic systems. *Contributions to Mineralogy and Petrology* 177, 1–36.

Mironov, N.L., Tobelko, D.P., Smirnov, S.Z., Portnyagin, M.V. & Krasheninnikov, S.P. (2020). Estimation of CO_2 Content in the Gas Phase of Melt Inclusions Using Raman Spectroscopy: Case Study of Inclusions in Olivine from the Karymsky Volcano (Kamchatka). *Russian Geology and Geophysics* 61, 600-610.

Miyagi, I., Itoh, J., Hoang, N. & Morishita, Y. (2012). Magma systems of the Kutcharo and Mashu volcanoes (NE Hokkaido, Japan): Petrogenesis of the medium-K trend and the excess volatile problem. *Journal of Volcanology and Geothermal Research* 231–232, 50–60.

Miyagi, I., Kita, N., & Morishita, Y. (2017). The geochemical and petrological characteristics of prenatal caldera volcano: a case of the newly formed small dacitic caldera, Hijiori, Northeast Japan. *Contributions to Mineralogy and Petrology*, 172(9), 79.

Miyagi, I. (2022). A preliminary assessment of the abundance of supercritical geothermal fluid using petrological methods: Cases of Kakkonda geothermal field and Aso volcano. In Grand Renewable Energy proceedings GRE2022 (p. 48). Japan Council for Renewable Energy.

Miyagi, I., Hoshizumi, H., Suda, T., Saito, G., Miyabuchi, Y. & Geshi, N. (2023). Importance

of Long-Term Shallow Degassing of Basaltic Magma on the Genesis of Massive Felsic Magma Reservoirs: a Case Study of Aso Caldera, Kyushu, Japan. *Journal of Petrology* 64, 1-25.

Melekhova, E., Schlaphorst, D., Blundy, J., Kendall, J.-M., Connolly, C., McCarthy, A. & Arculus, R. (2019). Lateral variation in crustal structure along the Lesser Antilles arc from petrology of crustal xenoliths and seismic receiver functions. *Earth and Planetary Science Letters* 516, 12–24.

Molina, J.F., Moreno, J.A., Castro, A., Rodriuez, C. & Fershtater, G.B. (2015). Calcic amphibole thermobarometry in metamorphic and igneous rocks: New calibrations based on plagioclase/amphibole Al-Si partitioning and amphibole/liquid Mg partitioning. *Lithos* 232, 286–305.

Morgan, G.B. & London, D. (2005). Effect of current density on the electron microprobe analysis of alkali aluminosilicate glasses. *American Mineralogist* 90, 1131–1138.

Murayama, I. (1978). The Narugo volcano, in: Volcanoes in Japan (I). Tokyo: Daimeido.

Morimoto, N. (1988). Nomenclature of Pyroxenes. *Mineralogy and Petrology* 39, 55–76.

Nakamura, H., Iwamori, H., Nakagawa, M., Shibata, T., Kimura, J. I., Miyazaki, T., Chang, Q., Stefanov Vaglarov, B.S.,, Takahashi, T., & Hirahara, Y. (2019). Geochemical mapping of slab-derived fluid and source mantle along Japan arcs. *Gondwana Research*, 70, 36-49.

Nakajima, J., Matsuzawa, T., Hasegawa, A., & Zhao, D. (2001). Seismic imaging of arc magma and fluids under the central part of northeastern Japan. *Tectonophysics*, 341(1), 1– 17.

Nakanishi, A., Kurashimo, E., Tatsumi, Y., Yamaguchi, H., Miura, S., Kodaira, S., Obana, K., Takahashi, N., Tsuru, T., Kaneda, Y., Iwasaki, T. & Hirata, N. (2009). Crustal evolution of the southwestern Kuril Arc, Hokkaido Japan, deduced from seismic velocity and geochemical structure. *Tectonophysics,* 472, 105-123.

Nandedkar, R.H., Ulmer, P. & Müntener, O. (2014). Fractional crystallization of primitive, hydrous arc magmas: An experimental study at 0.7 GPa. *Contributions to Mineralogy and Petrology* 167 1–27.

Newman, S. & Lowenstern, J.B. (2002). VOLATILECALC: A silicate melt-H_2O-CO_2 solution model written in Visual Basic for excel. *Computers & Geosciences* 28, 597–604.

Ogawa, Y., Ichiki, M., Kanda, W., Mishina, M., & Asamori, K. (2014). Three-dimensional magnetotelluric imaging of crustal fluids and seismicity around Naruko volcano, NE Japan. *Earth, Planets and Space*, 66(1), 1-13.

Okada, T., Matsuzawa, T., Nakajima, J., Uchida, N., Yamamoto, M., Hori, S., Kono, T., Nakayama, T., Hirahara, S. & Hasegawa, A. (2014). Seismic velocity structure in and around the Naruko volcano, NE Japan, and its implications for volcanic and seismic activities Geofluid processes in subduction zones and mantle dynamics 4. *Seismology. Earth, Planets and Space* 66, 1–10.

Omoto, K. (1993). Radiocarbon ages of organic materials collected from Narugo basin, Miyagi Prefecture. *Quaternary Research* 32, 227–229.

Oppenheimer, C. (2003). Climatic, environmental and human consequences of the largest known historic eruption: Tambora volcano (Indonesia) 1815. *Progress in Physical Geography: Earth and Environment* 27, 230–259

Oppenheimer, C., Fischer, T. P., & Scaillet, B. (2014). Volcanic degassing: Process and impact. Treatise on Geochemistry (Second Edition), 4, 111-179.

Parai, R. I. T. A., & Mukhopadhyay, S. U. J. O. Y. (2012). How large is the subducted water flux? New constraints on mantle regassing rates. *Earth and Planetary Science Letters*, 317, 396-406.

Petford, N. & Atherton, M. (1996). Na-rich Partial Melts from Newly Underplated Basaltic Crust: the Cordillera Blanca Batholith, Peru. *Journal of Petrology*, 37, 1491–1521.

Petford, N. & Gallagher, K. (2001). Partial melting of mafic (ambphibolitic) lower crust by periodic influx of basaltic magma. *Earth and Planetary Science Letters* 193, 483–499.

Piskunov, B.N. (1987). *Geological and petrological specifics of island arc volcanism*. Nauka, Moscow (In Russian).

Popa, R.-G., Bachmann, O. & Huber, C. (2021). Explosive or effusive style of volcanic eruption determined by magma storage conditions. *Nature Geoscience*, 14, 781-786.

Putirka, K. (2008). Thermometers and barometers for volcanic systems. *Reviews in Mineralogy and Geochemistry* 69, 61–120.

Putirka, K. (2016). Amphibole thermometers and barometers for igneous systems and some implications for eruption mechanisms of felsic magmas at arc volcanoes. *American*

Mineralogist 101, 841–858.

Rapp, R.P. & Watson, E.B. (1995). Dehydration melting of metabasalt at 8-32 kbar: Implications for continental growth and crust-mantle recycling. *Journal of Petrology* 36 891–931.

Rapp, R.P., Watson, E.B. & Miller, C.F. (1991). Partial melting of amphibolite/eclogite and the origin of Archean trondhjemites and tonalites. *Precambrian Resesearch* 51 1–25.

Richards, J. P. (2011). Magmatic to hydrothermal metal fluxes in convergent and collided margins. *Ore Geology Reviews*, 40(1), 1-26.

Rickwood, P.C. (1989). Boundary lines within petrologic diagrams which use oxides of major and minor elements. *Lithos* 22, 247–263.

Ridolfi, F. (2021). Amp-tb2: An updated model for calcic amphibole thermobarometry. *Minerals* 11, 1–9.

Ridolfi, F. & Renzulli, A. (2012). Calcic amphiboles in calc-alkaline and alkaline magmas: Thermobarometric and chemometric empirical equations valid up to 1,130°C and 2.2 GPa. *Contributions to Mineralogy and Petrology* 163, 877–895.

Riker, J.M., Blundy, J.D., Rust, A.C., Botcharnikov R.E. & Humphreys, M.C.S. (2015). experimental phase equilibria of a Mount St. Helens rhyodacite: a framework for interpreting crystallization paths in degassing silicic magmas. *Contributions to Mineralogy and Petrology* 170.

Roedder, E. (1984). *Fluid Inclusions. Mineralogical Society of America, Reviews in Mineralogy* 12

Rhodes, J.M., Dungan, M.A., Blanchard, D.P., & Long, P.E. (1979). Magma mixing at mid-ocean ridges: evidence from basalts drilled near 22 N on the Mid-Atlantic Ridge. *Tectonophysics* 55, 35–61.

Rose-Koga, E.F., Bouvier, A.S., Gaetani, G.A., Wallace, P.J., Allison, C.M., Andrys, J.A., Angeles de la Torre, C.A., Barth, A., Bodnar, R.J., Bracco Gartner, A.J.J., Butters, D., Danyushevsky, L.V., DeVitre, C.L., Drignon, M.J., France, L., Gaborieau, M., Garcia, M.O., Gatti, E., Genske, F.S., Hartley, M.E., Hughes, E.C., Iveson, A.A., Johnson, E.R., Jones, M., Kagoshima, T., Katzir, M. Kawaguchi, T. Kawamoto, K.A. Kelley, J.M. Koornneef, M.D. Kurz, M. Laubier, Y., Layne, G.D., Lerner, A., Lin, K-Y., Liu, P-P., Lorenzo-Merino, A., Luciani, N., Magalhães, N., Marschall, H.R., Michael, P.J.,

Monteleone, B.D., Moore, L.R., Moussallam, Y., Muth, M., Myers, M.L., Narváez, D.F., Navon, O., Newcombe, M.E., Nichols, A.R.L., Nielsen, R.L., Pamukcu, A., Plank, T., Rasmussen, D.J., Roberge, J., Schiavi, F., Schwartz, D., Shimizu, K., Shimizu, N., Thomas, J.B., Thompson G.T., Tucker, J.M., Ustunisik, G.M., Waelkens, C., Zhang, Y. & Zhou, T. (2021). Silicate melt inclusions in the new millennium: A review of recommended practices for preparation, analysis, and data presentation. *Chemical Geology* 570, 120145.

Rotman, V.K. (2000). Geological map: K-55-II, L-55-XXXII. State geological map of the Russian Federation. Second edition. Kurilskaya series, scale: 1:200000.

Rushmer, T. (1991). Partial melting of two amphibolites: contrasting experimental results under fluid-absent conditions. *Contributions to Mineralogy and Petrology*, 107(1), 41-59

Rutherford, M.J. & Hill, P.M. (1993). Magma ascent rates from amphibole breakdown: an experimental study applied to the 1980–1986 mount St. Helens eruptions. *Journal of Geophysical Research: Solid Earth* 98, 19667–19685.

Ryan, W. B., Carbotte, S. M., Coplan, J. O., O'Hara, S., Melkonian, A., Arko, R., Weissel, R. A., Ferrini, V., Goodwillie, A., Nitsche, F., Bonczkowski, J. & Zemsky, R. (2009). Global multi-resolution topography synthesis. *Geochemistry, Geophysics, Geosystems*, 10(3).

Sakaguchi, K. & Yamada, E. (1988). The Kitagawa Dacite', pyroclastic flow deposits around the Onikobe caldera, northeast Japan. *Report of the Geological Survey of Japan* 268.

Sato, M., Ban, M., Yuguchi, T., & Adachi, T. (2022). Pre-eruptive magmatic processes of historical activities at Zao volcano, northeastern Japan: Insights from compositional zoning in orthopyroxene phenocrysts. *Journal of Volcanology and Geothermal Research*, 432, 107686.

Saunders, K., Blundy, J., Dohmen, R., & Cashman, K. (2012). Linking petrology and seismology at an active volcano. *Science*, 336(6084), 1023-1027.

Schuraytz, B. C., Vogel, T. A. & Younker, L. W. (1989). Evidence for dynamic withdrawal from a layered magma body—the Topopah Spring Tuff, Southwestern Nevada. *Journal of Geophysical Research* 94, 5925–5942.

Shand, S.J. (1943). *The Eruptive Rocks*, 2nd edn. John Wiley, New York

Shillington, D. J., Van Avendonk, H. J., Holbrook, W. S., Kelemen, P. B., & Hornbach, M. J. (2004). Composition and structure of the central Aleutian island arc from arc-parallel

wide-angle seismic data. *Geochemistry, Geophysics, Geosystems*, 5(10).

Shimizu, K., Ushikubo, T., Hamada, M., Itoh, S., Higashi, Y., Takahashi, E. & Ito, M. (2017). H_2O, CO_2, F, S, Cl, and P_2O_5 analyses of silicate glasses using SIMS: Report of volatile standard glasses. *Geochemical Journal* 51, 299–313.

Shimizu, K., Ushikubo, T., Kuritani, T., Hirano, N. & Yamashita, S. (2022). Modification for the matrix effect in SIMS-derived water contents of silicate glasses. *Geochemical Journal* 56, 223–230.

Schneider, C. A., Rasband, W. S., & Eliceiri, K. W. (2012). NIH Image to ImageJ: 25 years of image analysis. *Nature methods*, 9(7), 671-675.

Shukuno, H., Tamura, Y., Tani, K., Chang, Q., Suzuki, T. & Fiske, R.S., (2006). Origin of silicic magmas and the compositional gap at Sumisu submarine caldera, Izu–Bonin arc, Japan. *Journal of Volcanology and Geothermal Reseach* 156, 187–216.

Sisson, T.W. & Grove, T.L. (1993). Experimental investigations of the role of H_2O in calc-alkaline differentiation and subduction zone magmatism. *Contributions to Mineralogy and Petrology* 113, 143–166.

Smirnov, S.Z., Rybin, A.V., Kruk, N.N., Timina, T.Yu., Sokolova, E.N., Kuzmin, D.V., Maksimovich, I.A., Kotov, A.A., Shevko, A.Ya., Nizametdinov, I.R. & Abersteiner, A. (2019). Parental Melts and Magma Storage of a Large-volume Dacite Eruption at Vetrovoy Isthmus (Iturup Island, Southern Kuril Islands): Insights into the Genesis of Subduction-zone Dacites, *Journal of Petrology* 60, 1349–1370.

Smirnov, S.Z., Rybin, A.V., Sokolova, E.N., Kuzmin, D.V., Degterev, A.V. & Timina, T.Yu. (2017). Felsic magmas of the caldera-forming eruptions on the Iturup Island: the first results of studies of melt inclusions in phenocrysts from pumices of the Lvinaya Past and Vetrovoy Isthmus calderas. *Russian Journal of Pacific Geology* 11, 46–63.

Soda, T. & Yagi, K. (1991). Quaternary tephra studies in the Tohoku district northeastern Honshu, Japan. *Quaternary Research* 30, 369–378.

Solaro, C., Balcone-Boissard, H., Morgan, D. J., Boudon, G., Martel, C., & Ostorero, L. (2020). A system dynamics approach to understanding the deep magma plumbing system beneath Dominica (Lesser Antilles). *Frontiers in Earth Science,* 8, 574032.

Stamper, C. C., Blundy, J. D., Arculus, R. J. & Melekhova, E. (2014). Petrology of Plutonic Xenoliths and Volcanic Rocks from Grenada, Lesser Antilles, *Journal of Petrology* 55,

1353–1387.

Stern C.R. (2004). Active Andean volcanism: its geological and tectonic setting. *Revista Geologica de Chile* 31, 161-206.

Syracuse, E.M., van Keken, P.E. & Abers, G.A. (2010). The global range of subduction zone thermal models. *Physics of the Earth and Planetary Interiors* 183, 73–90.

Takahashi, N., Kodaira, S., Klemperer, S. L., Tatsumi, Y., Kaneda, Y., & Suyehiro, K. (2007). Crustal structure and evolution of the Mariana intra-oceanic island arc. *Geology*, 35(3), 203-206.

Tamura, Y. & Tatsumi, Y. (2002). Remelting of an Andesitic Crust as a Possible Origin for Rhyolitic Magma in Oceanic Arcs: an Example from the Izu–Bonin Arc. *Journal of Petrology* 43, 1029–1047.

Taran, Y., Zelenski, M, Chaplygin, I., Malik, N., Campion, R., Inguaggito, S., Pokrovsky, B., Kalacheva, E., Melnikov, D., Kazahaya, R. & Fischer, T. (2018). Gas Emissions From Volcanoes of the Kuril Island Arc (NW Pacific): Geochemistry and Fluxes. *Geochemistry, Geophysics, Geosystems* 19, 1859–1880.

Till, C. B., Vazquez, J. A., & Boyce, J. W. (2015). Months between rejuvenation and volcanic eruption at Yellowstone caldera, Wyoming. *Geology*, 43(8), 695-698.

Tsuchiya. N., Itoh, J., Seki, Y. & Iwaya, T. (1997). Geological map of Japan, 1:50000, Iwagasaki. Geological Survey of Japan.

Tsuchiya, N., Yamada, R., & Uno, M. (2016). Supercritical geothermal reservoir revealed by a granite–porphyry system. *Geothermics*, 63, 182-194.

Ulmer, P., Kaegi, R. & Müntener, O. (2018). Experimentally derived intermediate to silica-rich arc magmas by fractional and equilibrium crystallization at 1.0 GPa: an evaluation of phase relationships, compositions, liquid lines of descent and oxygen fugacity. *Journal of Petrology* 59, 11–58.

Uno, M., Okamoto, A., & Tsuchiya, N. (2017). Excess water generation during reaction-inducing intrusion of granitic melts into ultramafic rocks at crustal P–T conditions in the Sør Rondane Mountains of East Antarctica. *Lithos*, 284, 625-641.

Van Keken, P. E., Hacker, B. R., Syracuse, E. M., & Abers, G. A. (2011). Subduction factory: 4. Depth-dependent flux of H2O from subducting slabs worldwide. *Journal of*

Geophysical Research: Solid Earth, 116(B1).

Vielzeuf, D. & Schmidt, M.W. (2001). Melting relations in hydrous systems revisited: Application to metapelites, metagreywackes and metabasalts. *Contributions to Mineralogy and Petrology* 141, 251–267.

Vigneresse, J.L., Barbey, P. & Cuney, M. (1996). Rheological transitions during partial melting and crystallization with application to felsic magma segregation and transfer. *Journal of Petrology* 37, 1579–1600.

Wallace, P.J. & Anderson, A.T. (1998). Effects of eruption and lava drainback on the H_2O contents of basaltic magmas at Kilauea Volcano. *Bulletin of Volcanology* 59, 327–344.

Wallace, P. J. (2005). Volatiles in subduction zone magmas: concentrations and fluxes based on melt inclusion and volcanic gas data. *Journal of volcanology and Geothermal Research*, 140(1-3), 217-240.

Waters, L.E., Andrews, B.J. & Frey, H.M. (2021). Daly Gaps at South Sister, Oregon, USA, generated via partial melting. *Contributions to Mineralogy and Petrology* 176, 1–33.

Watts, K.E., John, D.A., Colgan, J.P., Henry, C.D., Bindeman, I.N. & Schmitt, A.K. (2016) Probing the Volcanic–Plutonic Connection and the Genesis of Crystal-rich Rhyolite in a Deeply Dissected Supervolcano in the Nevada Great Basin: Source of the Late Eocene Caetano Tuff. *Journal of Petrology* 57, 1599–1644.

Whitaker, M.L., Nekvasil, H., Lindsley, D.H. & McCurry, M. (2008). Can crystallization of olivine tholeiite give rise to potassic rhyolites? - An experimental investigation. *Bulletin of Volcanology* 70, 417–434.

Wilshire, H., Meyer, C.E., Nakata, J.K., Calk, L.C., Shervais, J.W., Nielson, J.E., & Schwarzman, E.C. (1988). Mafic and ultramafic xenoliths from volcanic rocks of the western United States: *U.S. Geological Survey Professional Paper* 1443, 179 p.

Yoshida, T., Kimura, J.I., Yamada, R., Acocella, V., Sato, H., Zhao, D., Nakajima, J., Hasegawa, A., Okada, T., Honda, S., Ishikawa, M., Prima, O.D.A., Kudo, T., Shibazaki, B., Tanaka, A. & Imaizumi, T. (2014). Evolution of late Cenozoic magmatism and the crust–mantle structure in the NE Japan Arc. *Orogenic Andesites and Crustal Growth*, Ed: A. Gómez-Tuena, S. M. Straub, G. F. Zellmer.

Zellmer, G. F., Edmonds, M., & Straub, S. M. (2015). Volatiles in subduction zone magmatism. *Geological Society, London, Special Publications*, 410(1), 1-17.

Zhang, J., Humphreys, M.C.S., Cooper, G.F., Davidson, J.P. & Macpherson, C.G. (2017). Magma mush chemistry at subduction zones, revealed by new melt major element inversion from calcic amphiboles. *American Mineralogist* 102, 1353–1367.

Zhao, D., Matsuzawa, T., & Hasegawa, A. (1997). Morphology of the subducting slab boundary in the northeastern Japan arc. *Physics of the Earth and Planetary Interiors*, 102(1-2), 89-104.

Zharkov, R. V. (2020). Active Volcanoes and Thermal Springs of Kunashir Island (Russia). *IOP Conference Series: Earth and Environmental Science* 459, 022039.

Zlobin, T.K., Abdurakhmanov, L.I. & Zlobina, L.M. (1997). Deep seismic studies of the Mendeleev volcano in the southern Kuriles. *Russian Journal of Pacific Geology* 16, 79–87 (In Russian).

Achievements

Peer-Reviewed Journals, First Author

1) “Partial melting under shallow-crustal conditions: a study of the Pleistocene caldera eruption of Mendeleev volcano, southern Kuril Island Arc”, **Kotov A**., Smirnov S., Nizametdinov I., Uno M., Tsuchiya N., Maksimovich I. Journal of Petrology. egad033, https://doi.org/10.1093/petrology/egad033
2) “Method for Determining Water Content in Natural Rhyolitic Melts by Raman Spectroscopy and Electron Microprobe Analysis”, **Kotov, A.**, Smirnov, S., Plechov, P., Persikov E., Chertkova N., Maksimovich I., Karmanov N., Buhtiyarov P., Petrology. V. 29, P. 386–403, 2021. https://doi.org/10.1134/S0869591121040044

Peer Reviewed Journals, Non-First Author

1) “Hydrocarbons in Magmatic Fluid in Phenocrysts of Eruption Products of the Men’shii Brat Volcano (Iturup Island): Data from Pyrolysis-Free Gas Chromatography–Mass Spectrometry of Melt and Fluid Inclusions”, Nizametdinov I., Kuzmin D., Smirnov S., Bul’bak T., Tomilenko A., Maksimovich I., **Kotov A.**. Russian Geology and Geophysics, V. 63, Iss. 8, P. 890–900, 2022. doi: https://doi.org/10.2113/RGG20214415
2) “High explosivity of the June 21, 2019 eruption of Raikoke volcano (Central Kuril Islands); mineralogical and petrological constraints on the pyroclastic materials”, Smirnov S., Nizametdinov I., Timina T., **Kotov A.**, Sekisova V., Kuzmin D., Kalacheva E., Rashidov V., Rybin A., Lavrenchuk A., Degterev A., Maksimovich I., Abersteiner A., Journal of Volcanology and Geothermal Research, V. 418, 2021. https://doi.org/10.1016/j.jvolgeores.2021.107346.
3) “Parental Melts and Magma Storage of a Large-volume Dacite Eruption at Vetrovoy Isthmus (Iturup Island, Southern Kuril Islands): Insights into the Genesis of Subduction-zone Dacites”, Smirnov S., Rybin A., Kruk N., Timina T., Sokolova E., Kuzmin D., Maksimovich I., **Kotov A.**, Shevko A., Nizametdinov I., Abersteiner A., Journal of Petrology, V. 60, Iss. 7, P. 1349–1370, 2019. https://doi.org/10.1093/petrology/egz032
4) “Behavior of volatiles in the magmatic reservoirs of large-scale eruptions of Pleistocene-Holocene calderas of Iturup Island (Kuril Islands)”, Smirnov S., Maksimovich I., **Kotov A.**, Timina T., Bulbak T., Tomilenko A., Kuzmin D., Shevko A., Rybin A. Geosystems of transition zones, V. 2, № 4, P. 365-376, 2018. DOI: 10.30730/2541–8912.2018.2.4.365–376. (in Russian)

Peer Reviewed Conference Proceedings, First Author

1) “Water in melt inclusions from phenocrysts of dacite pumice of the Vetrovoy Isthmus (Iturup Island, Southern Kuriles)”, **Kotov A.A.,** Smirnov S.Z., Maksimovich I.A., Plechov, P., Chertkova, N.V., Befus, A.I., , IOP Conference Series: Earth and Environmental Science 110(1), 2018, DOI: 10.1088/1755-1315/110/1/012009

Peer Reviewed Conference Proceedings, Non-First Author

1) “Magma storage constrains by compositional zoning of plagioclase from dacites of the caldera forming eruptions of Vetrovoy Isthmus and Lvinaya Past' Bay (Iturup Island,

Kurile Islands)", Maksimovich I.A., Smirnov S.Z., **Kotov A.A**., Timina T, Shevko A.V., IOP Conference Series: Earth and Environmental Science 110(1), 2018, DOI:10.1088/1755-1315/110/1/012015

Conference presentations

1) **Kotov A**., Okumura S., Shimizu K., Miyagi I., Uno M., Tsuchiya N., Agroli G., Magma formation and water budget of the Naruko caldera, NE Honshu, Water-Rock Interaction WRI17 and Applied Isotope Geochemistry AIG14, Sendai, Japan, Poster.
2) **Kotov A**., Smirnov S., Nizametdinov I., Uno M., Tsuchiya N., Partial melting under shallow-crustal conditions: a study of the Pleistocene caldera eruption of Mendeleev volcano, southern Kuril Island Arc. Water-Rock Interaction WRI17 and Applied Isotope Geochemistry AIG14, Sendai, Japan, Oral.
3) **Kotov A**., Okumura S., Shimizu K., Miyagi I., Uno M., Tsuchiya N., Magma formation and water excess beneath Naruko caldera, NE Honshu. JpGU, 2023, Chiba, Japan, Poster.
4) **Kotov A**., Okumura S., Shimizu K., Miyagi I., Uno M., Tsuchiya N., Magma evolution and estimation of fluid amount from melt inclusion studies and numerical modeling in Naruko caldera, NE Japan., IAVCEI Scientific Assembly 2023, Rotorua, New Zealand, Online, Poster.
5) **Kotov A**., Smirnov S., Nizametdinov I., Uno M., Tsuchiya N., Evolution of the dacitic magma chamber of the Pleistocene caldera eruption of the Mendeleev volcano (Kunashir Island, Southern Kurils)., Russian Conference on Thermobarogeochemistry 2022, Novosibirsk, Russia. Online, Oral.
6) **Kotov A**., Okumura S., Shimizu K., Miyagi I., Uno M., Tsuchiya N., Natural and numerical considerations of water budget of the caldera-forming magmas in Naruko volcano, Northeast Japan., Annual Meeting of Japan Association of Mineralogical Sciences (JAMS), 2022, Niigata, Oral.
7) **Kotov A.,** Shimizu K., Okumura S., Uno M., Tsuchiya N., Accumulation of water in the caldera-forming magmas of the Naruko volcano, JpGU, 2022, Chiba, Oral.
8) **Kotov A**, Smirnov S., Maksimovich I., Uno M., Nizametdinov I., Tsuchiya N., Petrogenesis of Mendeleev Volcano Dacitic Magmas (Kunashir Island, Southern Kurils), American Geophysical Union (AGU-2021), Online, Oral.
9) **Kotov A.**, Smirnov S, Tsuchiya N, Uno M, Petrology of pumice stone in the 39ka caldera-forming eruption of Mendeleev volcano (Kunashir Island), Annual Meeting of Japan Association of Mineralogical Sciences (JAMS), 2021, Online, Oral.
10) **Kotov A.**, Smirnov S., Tsuchiya N., Uno M., Behavior of volatile components in the magmatic system of Mendeleev volcano (Kunashir Island), Geothermal Volcanology Workshop, 2021, Online, Oral.
11) **Kotov A.A.,** Smirnov S.Z., Tsuchiya N., Uno M., Evolution of the magmatic-hydrothermal system of Mendeleev volcano (Kunashir Island), Japan Geoscience Union Meeting, June 2021, Online, Oral.
12) **Kotov A.A**., Smirnov S.Z., Nizametdinov I.R., Maksimovich I.A., The first results of studying dacite pumice of the Late Pleistocene caldera eruption of volcano. Mendeleev (Kunashir Island), XXXI conference "Actual problems of geology, geophysics and ecology", October 2020, Saint-Petersburg, Russia. Oral.
13) **Kotov A.A**., Sekisova V.S., Mokrushina O.D., Kozlov E.N., Fomina E.N., Fluid inclusions in graphite-bearing quartzolithes from the Lovozero region (Kola peninsula, Russia). XXX conference "Actual problems of geology, geophysics and ecology", October 2019, Apatity, Russia. Oral.

14) **Kotov A.A**., Smirnov S.Z., Maksimovich I.A., Timina T.Yu, The behavior of volatile components (S, F, Cl) in dacitic magma of a large caldera eruption of the Vetrovoy Isthmus (Southern Kuriles) according to the results of the study of apatites, The 10th international workshop on the Japan- Kurile-Kamchatka-Aleutian volcanic arcs (JKASP-2018), August 20th -26th, 2018, Petropavlovsk-Kamchatsky, Russia. Oral.
15) **Kotov A.A**., Smirnov S.Z., Maksimovich I.A., Behavior of water and fluid regime variations in the chamber of dacitic magma of the caldera eruption of the Vetrovoy Isthmus (Iturup island), XVIII All-Russian Conference on Thermobarogeochemistry, September 2018, Moscow, Russia. Oral.
16) **Kotov A.A**., Smirnov S.Z., Maksimovich I.A, Water in melt inclusions from phenocrysts of dacitic pumice at the Vetrovoy Isthmus (Iturup Island), IX conference « Petrology of magmatic and metamorphic complexes», November 2017, Tomsk, Russia. Oral.

Acknowledgments

I would like to express my deep gratitude to my research supervisor Professor Noriyoshi Tsuchiya, for his guidance, comprehensive support, insightful comment, and fresh ideas.

I am extremely grateful to my first teacher and mentor Professor Sergey Smirnov, who always remains an example for me and thanks to whom I found myself in science and formed my petrological mindset.

My special thanks to Professor Michihiko Nakamura, Professor Atsushi Okamoto, and Professor Masao Ban for their detailed review of this dissertation, interesting discussions, and very helpful recommendations.

This work would not have been done without a great contributions of Dr. Isoji Miyagi who helped conduct the Rhyolite-MELTS modelling and Dr. Kenji Shimizu who helped to conduct the SIMS analyses in JAMSTEC.

I really appreciate Associate Professor Masaoki Uno and Associate Professor Satoshi Okumura for all the help, discussions, experiments, and involvement in my research throughout my research journey.

I would like to offer my special thanks to Manzshir Bayarbold, Geri Agroli and Diana Mindaleva who helped me a lot along my way and good friend.

I wish to thank Japanese Government giving me an opportunity as MEXT Scholarship Awardee in International Environmental Leadership Program (IELP), Graduate School of Environmental Studies (GSES) with all of the full financial support.

I would also like to thank the staff of GSES who helping me with full of smile particularly Ms. Yoko Akasaka and Ms. Yuko Sasahara.

Finally, I am sincerely grateful to my family and my dear Alina Sevets for their unconditional patience, love and support always in any situation.